ABSTRACT

Title of Dissertation: Domain Wall Engineering of Nanoscale Ferromagnetic Elements and its Application for Memory Devices

Sylvia H. Flórez, Doctor of Philosophy, 2006

Dissertation directed by: Professor R.D. Gomez
Department of Electrical and Computer Engineering

This thesis concerns the interaction of spin polarized electrons with the local magnetic moments in nanopatterned metallic systems. We study novel magnetic phenomena appearing in patterned thin-film magnetic wires with length scales in the nanometer regime and in magnetic multilayers. The work has three mayor foci. The first is the interaction between magnetic domain walls and conduction electrons in single layer nanowires. We demonstrate the effect of using small constrictions as artificial traps for domain walls and use these structures to measure the contribution of a domain wall to the *electrical resistivity*. These measurements are correlated with the specific micromagnetic distribution induced by the constriction geometry. Similarly, we demonstrate and characterize the effect of spin current induced magnetization *reversal* in nanowires. This includes a measurement of the critical current/field phase space boundary between static and

moving walls and an estimation of the intrinsic wall mobility. The second is focused on understanding the effects of spin current, *vis-à-vis*, magnetoresistance and domain wall motion, in a multilayer nanostructure device exhibiting giant magnetoresistance (GMR). To demonstrate a potential application, we incorporate the effects of domain wall trapping and spin current induced domain wall motion into a nanometer scale spin-valve device. The device can be fully controlled through current and exhibits significant GMR response. This approach may be useful as a memory element in magnetoresistive random access memory (MRAM) technology, and the device serves as a proof of concept. The third focus is the understanding of the effect strain on the resistance of antiferromagnetically (AF) coupled giant magnetoresistive (GMR) multilayers containing highly magnetostrictive materials. Our measurements reveal that inverse magnetostriction effects lead to enhanced strain sensitivity in comparison to films made of the materials that compose the multilayer. A simple phenomenological model describing the measured field dependence of these effects is used to identify field-biasing values that optimize amplitude, linearity and reversibility of the effect.

Domain Wall Engineering of Nanoscale Ferromagnetic Elements and its Application for Memory Devices

by

Sylvia H. Flórez

Dissertation submitted to the Faculty of the Graduate School of the
University of Maryland, College Park in partial fulfillment
of the requirements for the degree of
Doctor of Philosophy
2006

Advisory Committee:

Professor R.D. Gomez, Chairman/Advisor
Professor Isaak Mayergoyz
Professor Agis A. Iliadis
Professor Martin Peckerar
Professor Lourdes G. Salamanca-Riba (Dean's Representative)

DEDICATION

Dedicated to my Mother, Cecilia Mariño,

my Father, Jaime Flórez

and my husband Vasily Dronov

for the support and inspiration they provide.

ACKNOWLEDGEMENTS

While working toward my Doctoral degree, I had the great fortune to meet and collaborate with many great people, and while I am the sole author of this thesis, I am deeply indebted to the many who have contributed to the process that ends with this dissertation. It is now my great pleasure to take this opportunity to thank them.

Firstly, I would like to thank my advisor Professor Gomez for being a great mentor. I thank him for introducing me to the fascinating world of magnetism and especially for his continual support and friendly encouragement during this project.

I would also like to thank the dissertation committee members Professor Salamanca-Riba, Professor Isaak Mayergoyz, Professor Martin Peckerar and Professor Agis Illiadis for their time and effort in the evaluation of this dissertation.

I am very grateful to the Laboratory for Physical Sciences (LPS) and The National Science Foundation (NSF) for supporting me as a

graduate student as well as my research.

During my time as a PhD student, I was lucky enough to have been surrounded by wonderful people. I would like to thank all my friends and colleagues at LPS for providing me with a very stimulating and enjoyable working environment. Special thanks go out to Dr. Charles Krafft and Dr. Michael Dreyer for endless support and advice on my research. I also owe a debt of gratitude to my fellow group members, Jookyung Lee, Herman Pandana and Konrad Aschenbach as well as to previous members Marcia Golub, Seok-Hwan Chung, Hyuncheol Koo and Li Gan who all provided much help and support.

Finally, my most deep-felt gratitude goes out to my husband Vasily Dronov, who has been at my side for all the years in graduate school and whose advice, support and participation were invaluable, and to my parents Cecilia and Jaime Florez and sisters Andrea and Guiomar who have always provided their unconditional support and inspiration. The knowledge and genuine interest in science that I acquired in the first decades of my life was entirely due to them, and this interest and desire to obtain more knowledge is still a major driving force for me.

TABLE OF CONTENTS

LIST OF TABLES

LIST OF FIGURES

Chapter 1

Introduction

Magnetism has remarkable effects on the behavior of conduction electrons. During the past two decades, researchers studying these effects have made exciting discoveries that have revolutionized the magnetic recording industry. The most prominent examples are the giant (GMR) and tunneling (TMR) magnetoresistance effects that appear in magnetic multilayer structures (MML). In the simple case of single-layer ferromagnetic films, a rich variety of effects such as the anisotropic and lorentz magnetoresistance (AMR/LMR) have been observed and reasonably well understood. Ultimately, these effects are directly related to the electron spin and their study is central for an emerging field known as *spintronics*. The aim of this field is to exploit the quantum mechanical properties of the electron in the design of a new generation of microelectronic devices. Recent advancements towards this objective have, to some extent, been made possible by the rapid progress in fabrication technology, continually allowing further miniaturization. This technology is crucial as quantum mechanical effects are more strongly expressed as device characteristic dimension are reduced.

In this thesis we study issues of critical importance to the development of spintronics, such as static and dynamic properties of nanoscale magnetic systems.

An important focus in this thesis is the interaction that arises between conduction electrons and the domain walls (DW) in a ferromagnet (FM). The interest sparks from the idea that effects similar to the giant magnetoresistance (GMR) effect are expected to arise, given that in both cases there is spin-dependent transport through non-collinear magnetizations. From a technological standpoint, there are two distinct motivations for studies concerning this interaction. First, there is a very high potential for a wide variety of novel devices based on the transport properties of domain walls and second, as fabrication technology allows further miniaturization of magnetic devices, novel quantum effects become increasingly important.

As the electron crosses the domain wall, two types of effects are manifested. The first are scattering effects at the interface leading to a resistance contribution from the domain wall. Secondly, since the direction of electron spin is reversed after crossing the wall, the local magnetization from the wall applies an exchange torque on this electron spin. Conversely, the spin creates a reaction torque on the wall allowing the possibility of moving domain wall through applied currents. The effects of domain wall resistance (DWR) and current induced domain wall motion (DWM) are crucially important effects in terms of device applications. DWR is an efficient transducer of magnetization state, while DWM is an effective means of altering the magnetic state. The combination of these effects thus allows one, in principle, to construct a magnetic non-volatile memory.

In this thesis I investigate the effects DWR and DWM in ferromagnetic elements with nanometer scale geometrical constraint and subsequently use this knowledge to fabricate a spin-current controlled spin-valve device. The device serves as proof of concept for the implementation of these effects in novel mag-

netic random access memory elements.

Additional experiments, also focusing on GMR multilayers (ML), are included in the final part of this thesis. In these experiments we studied the *elastoresistive* properties of GMR ML containing highly magnetostrictive materials. The field dependence of these effects together with a simple phenomenological model describing the origin of the effects is included.

The thesis is divided into eight chapters. Chapters two and three review relevant fundamental background material in magnetism. The first centering on basic magnetostatics properties of thin films and nanoscale magnetic systems and the second concentrating on electrical transport effects appearing in these systems. This chapter also provides a thorough review of most of the magnetoresistive (MR) effects discovered and some widely used spin dependent devices. Chapter four describes the basics of magnetic force microscopy (MFM), as this technique is the most important experimental technique used throughout this work.

The subsequent chapters focus on the core material of this thesis. Chapter 5 covers our experiments on domain wall resistivity. After briefly reviewing some important precursor experiments, we describe our measurement of the electrical resistivity of single head-to-head domain wall in permalloy. Correlations between domain wall geometry and the sign of the effect are also made. To support these conclusions, we present results of micromagnetic simulations performed on the studied structures. We finalize the chapter by discussing the most important models for the effect and comparing them with our experimental results.

Chapter 6 deals with the important issue of spin-current induced domain wall motion. The chapter is divided into two parts. The first describes the physical origin of the effect, which is basically the exchange interaction between

electrons in the domain wall and the conduction electrons. While in the second, we present our experimental findings for the case of permalloy nanowires. This not only includes measurement of the critical current density required for domain wall motion (in absence of applied field), but also its field dependence.

In the following chapter, we illustrate an application of the phenomena of spin-current induced domain wall motion by implementing this effect in a sub-micron sized spin-valve. Details concerning the device structure and magnetic properties are included. Additionally, the behavior of the current induced switching of the device is thoroughly described.

Finally, chapter 8 describes experiments performed on CoFe/Cu antiferromagnetically (AF) coupled GMR multilayers. In this case we measure the *elastoresistance* of the multilayer, i.e., variations in resistivity due to strain-induced changes in magnetization. This type of phenomenon, originates mainly from the inverse magnetostriction effect taking place in the magnetic layers. Since these magnetizations are coupled, strain induces an overall effect on the film resistivity. Our measurements reveal that these effects lead to enhanced strain sensitivity in comparison to films made of the materials the materials that compose the multilayer.

While most equations are in cgs system of units, as this system is widely used by the magnetics scientific community, some values are given in SI units since the data acquisition uses this system and magnitudes may be somewhat easier to grasp.

Chapter 2

Magnetism in Nanoscale Structures

2.1 Review of Basic Ferromagnetism

2.1.1 Energy and Domain Formation

During the past two decades, powerful magnetic imaging techniques such as magnetic force microscopy (MFM) and lorentz microscopy (LM) have been developed. These techniques have enabled us to observe with great detail, the magnetic features that form in ferromagnetic (FM) films. Typically these samples are comprised of uniformly magnetized regions, called *magnetic domains* separated by transition regions known as *domain walls*. Pierre Weiss [1] proposed in 1907, the existence of domain walls (DW) and the concept of a magnetic materials breaking up into magnetic domains. These ideas allowed him to explain why some soft ferromagnetic materials seem to be nonmagnetic when in absence of external magnetic fields. This follows directly from the fact that the domain magnetizations in these materials have random directions and therefore cancel each other out.

In general, the exact magnetic configuration of a given film, i.e., the position of

the domains and domain walls, their shape and dimensions, depends essentially on the competition between the different types of energy present. These are mainly exchange, anisotropy, magnetoelastic and the zeeman energies. The first, the *exchange* energy is the strong quantum mechanical interaction responsible for maintaining adjacent magnetic moments within a magnetic domain, aligned. It arises because electrons are fermions, and can be modeled through the Heisenberg Hamiltonian.

$$H_{ex} = -2 \sum_{j>i} J_{ij} \mathbf{S}_i \cdot \mathbf{S}_j \tag{2.1}$$

where S_i and S_j represent spins of two distinct atomic sites and J is the exchange integral of the overlap of the wave functions of the i^{th} and j^{th} atoms. This integral can be calculated by considering the Hamiltonian for a two electron system and then using perturbation theory to calculate the shifts in energy that arise when the electrons are brought closer to each other and allowed to interact. The resulting expression ultimately depends on the Coulomb interaction and the *symmetry* of electron spin states. Thus, the exchange interaction, being essentially a consequence of the Pauli exclusion principle is *electronic* and not of magnetic in nature. Clearly, when $J > 0$, the system is ferromagnetic while if $J < 0$, the system is antiferromagnetic (AF).

This Hamiltonian, originally formulated by Heisenberg [2, 3] and Dirac [4, 5] in 1926, is adequate for modeling materials where magnetic electrons are well localized, such as insulators. Nevertheless, it is possible to use this model to estimate the exchange energy in metals. We simplify the problem by assuming that the interaction energy J does not depend on the specific spins and that the

angle θ is small. The average of equation 2.1, is then approximately given by

$$H_{ex} = -2J \sum_{j>i} S^2 \cos\theta_{ij} \approx JS^2 \sum_{j>i} \theta_{ij}^2 + constant \tag{2.2}$$

In terms of continuous variables this angular change is approximately $a\partial\theta/\partial x$, where a is the spin lattice constant. The exchange energy (per unit volume), can then be expressed in both microscopic and macroscopic form as:

$$f_{exchange} = \frac{N_v JS^2}{2}\theta_{ij}^2 = A\left(\frac{\partial\theta}{\partial x}\right)^2 \rightarrow A\sum\left(\frac{\nabla M_i}{M_s}\right)^2 \tag{2.3}$$

Where N_v is the number of nearest neighbor spins, per unit volume, and $A = \frac{s^2a^2JN_v}{2}$ is a constant known as the exchange stiffness.

The *magnetostatic* energy is another type of energy that appears as a consequence of the discontinuities in the normal component of the magnetization across an interface. These discontinuities give rise to surface magnetic charges that induce a demagnetizing field that emanates from the surface north-pole, passes through the sample and terminates at the surface south-pole. This dipolar interaction between magnetic surface poles is responsible for the shape dependent anisotropy present in many magnetic systems. The corresponding energy density will depend on the magnetization and the strength of this demagnetizing field as $f_{ms} = -\frac{1}{2}M_s \cdot H_{demag} = -\frac{1}{2}NM_s^2$, where we have used the fact the demagnetizing field can be shown to be proportional to the magnetization. The proportionality factor N is known as the demagnetizing factor. For an infinite sheet $N = 4\pi$ if the magnetization is normal to the surface (or equivalently in SI, N=1) while N=0 for in-plane magnetization .

Another source of anisotropic energy is the *magnetocrystalline* energy, which describes the preference for the magnetization to be aligned along certain crystallographic directions. This energy is not of dipolar origin, but is instead due

to spin-orbit coupling as well as the crystalline electric field determined by the specific chemical bonding. Two common types are the *uniaxial* and *cubic* and the energy corresponding to the first case is given by $f_a^{uni} = k_2 \sin^2\theta + k_4 \sin^4\theta$. In the case of polycrystalline samples, as the ones used throughout this work, the contribution from the crystalline anisotropy in a given direction is the average of the single crystal anisotropies.

Yet another form of anisotropy energy is the *magnetoelastic*. In this case the preferential directions are induced by strain. For the specific case of an isotropic material it is give by $f_{me}^{iso} = \frac{3}{2}\lambda_s \sigma \cos^2\theta$, where σ is the strain, λ_s the saturation magnetostriction, and θ the angle between the magnetization and the angle at which strain is applied.

Finally, there is the energy provided by an externally applied magnetic field. This is known as the *Zeeman* energy, and it is essentially the potential energy of the magnetic moments in the applied field, given by $f_z = -\mathbf{M} \cdot \mathbf{H}$. The competition of these energies within a magnetic sample will ultimately determine the particular magnetization arrangement that will develop in a given sample.

2.1.2 Bloch and Neél Walls

For bulk magnetic sample in absence of applied field or strain, it is mainly the interaction between the exchange and anisotropy energies that determines the formation of domain walls. In the simple case of sample with uniaxial anisotropy, the magnetizations in two adjacent domains will be in opposing directions along its easy axis. The 180° domain wall formed in between is known as a Bloch wall in recognition for F. Bloch's intensive studies on this type of structure [6, 7]. The wall will tend to position itself at a location where the sample width is minimized

(along the hard axis or transverse direction) in order to minimize the wall area and thereby the wall energy. The specific width δ_{DW} of the wall can be obtained from minimization of the sum of exchange and anisotropic energies. This can be understood by considering that a very thin wall will have high exchange energy (and low anisotropic energy) while the opposite occurs for wide walls.

To calculate the precise internal structure of the domain wall, variational techniques that allow *local* minimization of energy must be employed. The first of these calculations was performed by Landau [8] for the one dimensional Bloch wall case. As before, he considered the sum of anisotropy and exchange type energy densities and integrated them along the thickness of the wall. The magnetostatic energy contribution can be ignored if we are assuming the case of an infinite crystal.

$$\sigma = \int_{-\infty}^{+\infty} [f_a(\theta) + A\left(\frac{\partial\theta}{\partial x}\right)^2]dx \tag{2.4}$$

Minimizing this expression with respect to variations in the wall profile $\theta(x)$ leads to an Euler type equation for the domain wall

$$\frac{\partial f_a(\theta)}{\partial\theta} - 2A\frac{\partial^2\theta}{\partial x^2} = 0 \tag{2.5}$$

Each term represents local torques on the magnetization arising from the respective gradients of anisotropy and exchange energies. For the case of a uniaxial anisotropy, the wall profile can be found to be

$$x = \sqrt{\frac{A}{k_u}}\ln(\tan(\theta/2)) \tag{2.6}$$

The domain wall width is typically defined in terms of the slope at the center of the wall, while the energy density σ_{dw} can be obtained by integrating the energy along the wall. This results in $\delta_{DW} = \pi\sqrt{\frac{A}{k_u}}$ and $\sigma_{DW} = 4\sqrt{Ak_u}$. Typical values for Bloch walls appearing in common soft ferromagnets are compiled in Table

Material / Parameter	Fe	Ni	Co	NiFe alloys	Permanent Magnets
δ_{DW} (nm)	30	72		~ 1000	<10
$\sigma_{DW}(mJ/m^2)$	3	0.7		~ 0.1	30

Table 2.1: Typical values for domain wall width and energy density for Bloch walls in given materials.

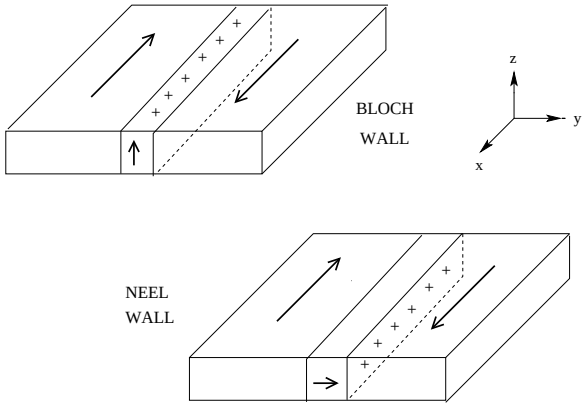

Figure 2.1: Comparison of Bloch and Neél domain wall configurations.

2.1. In the case of thin films below 60 nm, domain walls will have a different structure since the magnetization will prefer to lie in the plane of the film in order to minimize dipolar magnetostatic interaction between free poles at the films surfaces. In this situation a different type of domain wall, with magnetizations rotating 180° degrees *in the plane* of the film is formed. This type of domain wall is known as a Neél wall [9]. Figure 2.1 depicts these two wall configurations. Following from Maxwell's equations, the perpendicular component of the magnetic field must be conserved across any interface (including a domain wall), this implies the existence of magnetic charges at the surfaces of the Neél walls. These walls can thereby repel or attract each other. In contrast with the Bloch wall, the

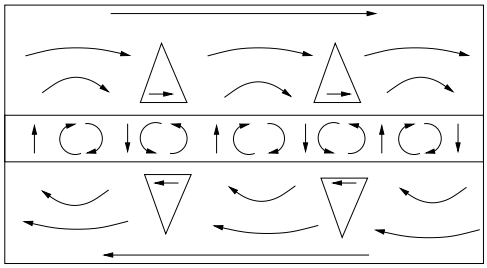

Figure 2.2: Magnetic configuration at a cross-tie wall.

Neél wall thickness increases with decreasing film thickness in order to minimize the magnetostatic energy associated with the charged surfaces faces of the wall. Examples of other types of magnetostatically induced domain walls that can arise in magnetic films are 90° degree and cross-tie walls. The first occur in materials of cubic anisotropy (for $K_1 > 0$) while the second are basically degenerated Neél walls with reduced magnetostatic energy. More specifically, in order to reduce the magnetostatic energy associated with the magnetic charge forming in the Neél configuration, the sense of polarization of the wall alternates as shown in figure 2.2. The nonlocal nature of the self interactions is in part responsible for the complex domain configurations that can arise in thin films.

2.1.3 Dietze and Thomas Model For 1D Domain Walls

In this section we generalize the problem of 1D walls forming in FM films, by describing a simple and illustrative model proposed by Dietze and Thomas [10]. The model not only proves that the DW types proposed by Bloch and Neél are the only possible 1D configurations, but also allows calculation of the magnetostatic energy terms involved in both cases. For the analysis we consider a film of width $2b$ in the y direction and infinite in both x and z directions, as shown in figure 2.3. Here a denotes the region occupied by the one dimensional domain

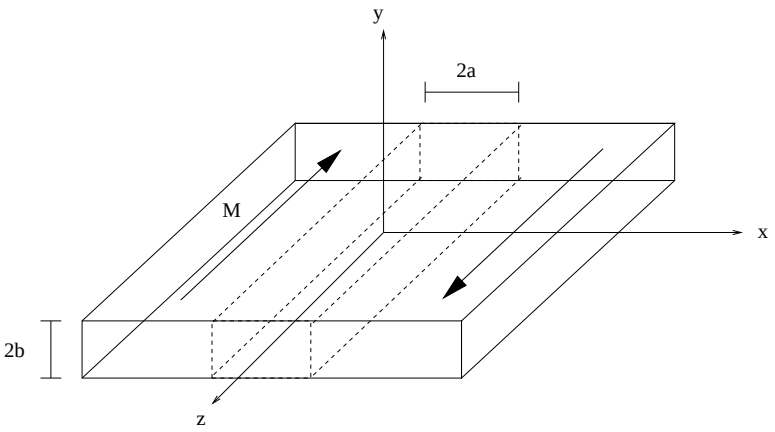

Figure 2.3: Geometry 1D wall calculation.

wall. If z denotes the easy axis, two antiparallel domains will form along this direction as shown. In this model, it is assumed that the x and y components of magnetization are given by $m_x(x) = \frac{q^2 cos\phi}{q^2+x^2}$ and $m_y(x) = \frac{q^2 sin\phi}{q^2+x^2}$ and where q is a variable parameter that related to the domain wall width. If $\phi = \frac{\pi}{2}$ the wall is Bloch type and if $\phi = 0$ it is Neél Type. The z-component can be calculated by taking into account the requirement that $m_x^2 + m_y^2 + m_z^2 = 1$ and the fact that $m_z(\pm\infty) = \pm 1$ (at the end of the wall) which leads to

$$m_z(x) = \frac{x\sqrt{2q^2 + x^2}}{q^2 + x^2} \tag{2.7}$$

The wall is assumed to be one dimensional and m is assumed to be only a function of x. The magnetostatic potential, obtained directly from Maxwell's equation, is given by the well known expression:

$$U_{ms} = \frac{\gamma_B}{4\pi}\left(\int \frac{\nabla' \cdot \mathbf{M}(\mathbf{r}')}{|\mathbf{r} - \mathbf{r}'|} dv' + \int \frac{\mathbf{n} \cdot \mathbf{M}(\mathbf{r}')}{|\mathbf{r} - \mathbf{r}'|} dS'\right) \tag{2.8}$$

Where $\gamma_B = 1$ for SI units and $\gamma_B = 4\pi$ for cgs units. In a slab of dimensions $-a \leq x \leq a$,$-b \leq y \leq b$,$-c \leq z \leq c$, the volume part of the potential can be

written

$$U_{vol} = -M_s \int_{-c,c} \int_{-b,b} \int_{-a,a} \frac{\frac{\partial m(x',y',z')}{\partial x'} + \frac{\partial m(x',y',z')}{\partial y'} + \frac{\partial m(x',y',z')}{\partial z'}}{\sqrt{(x-x')^2 + (y-y')^2 + (z-z')^2}} dx'dy'dz' \quad (2.9)$$

Integrating by parts, the first term with $\partial m_x/\partial x'$ with respect to x', and the second with respect to y', etc it is found that the terms evaluated between the limits $-a, a$ etc cancel the potential of the surface charge. If we additionally assume a two dimensional magnetization that does not depend on z, the total potential simplifies to:

$$U(x,y) = M_s \int_{-b}^{b} \int_{a}^{a} \frac{(x-x')m_x(x',y') + (y-y')m_y(x',y')}{(x-x')^2 + (y-y')^{3/2}} dx'dy' \quad (2.10)$$

For the rectangular slab, the potential can be calculated by integrating within the area delimited by $-a \leq x \leq a$. The corresponding magnetostatic energy will be given by

$$E_M = \frac{1}{2} \int (M \cdot \nabla U) dS = \frac{1}{2} M_s \int_{-a}^{a} \int_{-b}^{b} \left[m_x(x) \frac{\partial U}{\partial x} + m_y(x) \frac{\partial U}{\partial y} \right] dxdy \quad (2.11)$$

For the simple case of a one dimensional magnetization only dependent on x. After some manipulation, as explicitly shown in reference [18] the magnetostatic energy of this rectangular slab can be expressed as

$$\begin{aligned} E_M = 2M_s^2 \int_{0,\infty} \frac{1 - e^{-2bt}}{t} \int_{-a}^{a} \int_{-a}^{a} cos[(x-x')t][m_y(x)m_y(x') - m_x(x)m_x(x')]dx'dxdt \\ + 2\pi b \int_{-a}^{a} [m_x(x)]^2 dx \end{aligned} \quad (2.12)$$

By substituting the model in equations 2.12, for the case of $a \to \infty$ we find a magnetostatic energy per unit wall area

$$\varepsilon_M = \pi^2 M_s^2 \left[q cos^2\phi + \frac{q^2}{b} (sin^2\phi - cos^2\phi) log\left(1 + \frac{b}{q}\right) \right] \quad (2.13)$$

For a Neél wall, with $\phi = 0$ this energy is proportional to $1-(q^2/b)log(1+(b/q))$ For a Bloch wall, on the other hand, with $\phi = \frac{\pi}{2}$ this energy is proportional to $(q^2/b)log(1+(b/q))$ which goes to zero for $b \to 0$. For thin films, where the energy of the surface charge is larger than that of the volume charge, a Neél wall exist, while a Bloch wall will form in thick films for which the magnitudes of these energy components are inverted. For this model, the exchange energy, per unit wall area is given by

$$\varepsilon_{ex} = \frac{A}{2bM_s^2}\int_{-b}^{b}\int_{-\infty}^{\infty}((\nabla m_x)^2 + (\nabla m_y)^2)dxdy = \frac{2\pi A}{q}(\sqrt{2}-1) \tag{2.14}$$

While the uniaxial anisotropy energy, per unit wall energy

$$\varepsilon_{ani} = \frac{K_1}{2b}\int_{-b}^{b}\int_{-\infty}^{\infty}(1-m_z^2)dxdy = \frac{K_1}{2b}\int_{-b}^{b}\int_{-\infty}^{\infty}\frac{K_1 q^4}{(q^2+x^2)^2}dxdy = \frac{\pi q}{2}K_1 \tag{2.15}$$

From these expressions we note that only the magnetostatic energy component depends on the angle ϕ. Furthermore since $\partial\varepsilon_M/\partial\phi \propto \cos\phi\sin\phi$ then $\partial\varepsilon_M/\partial\phi = 0$ has only the two solutions previously mentioned. One with $sin\phi = 0$ and with total wall energy per unit wall area

$$\varepsilon_{NEEL} = \frac{2\pi A}{q}(\sqrt{2}-1) + \frac{\pi q}{2}K_1 + \pi^2 M_s^2 q[1 - \frac{q}{b}log(1+\frac{b}{q})] \tag{2.16}$$

And another with $cos\phi = 0$ and with total wall energy per unit wall area

$$\varepsilon_{BLOCH} = \frac{2\pi A}{q}(\sqrt{2}-1) + \frac{\pi q}{2}K_1 + \frac{\pi^2 M_s^2 q^2}{b}log(1+\frac{b}{q}) \tag{2.17}$$

Therefore no other types of one dimensional walls are expected to exist. The complexity of the magnetostatic term, even in the simple one dimensional case becomes evident. Minimizing the wall energy with respect to q can obtain the following transcendental equations

$$\frac{2A}{q^2}(\sqrt{2}-1) = \frac{K_1}{2} + \pi M_s^2[1 - \frac{2q}{b}log(1+\frac{b}{q}) + \frac{q}{q+b}] \tag{2.18}$$

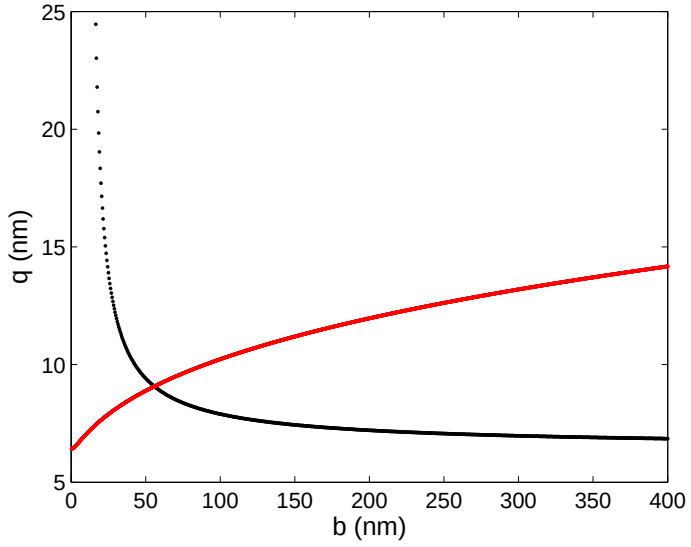

Figure 2.4: Variation of width parameter q with film thickness for Bloch and Neél walls in permalloy.

For the Neél, and Bloch walls respectively.

$$\frac{2A}{q^2}(\sqrt{2}-1) = \frac{K_1}{2} + \pi M_s^2[\frac{2q}{b}log(1+\frac{b}{q}) - \frac{q}{q+b}] \tag{2.19}$$

Analytical solutions, in agreement with Landau and Liftshitz [8] approach are only possible for the limiting cases of $b \to 0$ and $b \to \infty$. For intermediate thickness, the equations must be solved numerically, as shown in figure 2.4 for the case of permalloy with $A \sim 1 \times 10^{-6}\ ergs/cm$ (or $A \sim 1 \times 10^{-11}$ J/m), $M_s \sim 800$ emu (or $M_s \sim 8.5 \times 10^5$ A/m) and $k \sim 3 \times 10^3\ ergs/cm^3$ (or $k \sim 3 \times 10^2\ J/m^3$).

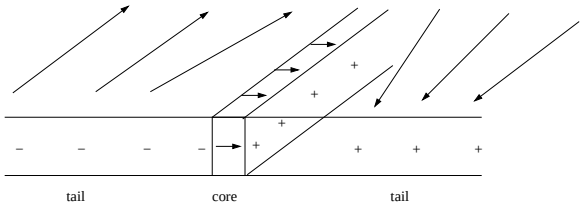

Figure 2.5: Decomposition of Neél wall into three regions (a core and two tails) of different length scale.

2.2 Multidimensional Domain Wall Structures in Thin Films

As film thickness is reduced, the assumption of 1DIM infinitely extended domain walls breaks down and a full description of domain wall properties requires a *multidimensional* approach. Even in the simplest case of the 1D symmetric Neél wall, appearing only in very thin films (below 50 nm for permalloy) where the magnetization is confined to the film, the stray field of the wall can not be described in one dimension. Early attempts to compute micromagnetic properties of the wall numerically encountered many difficulties when using a fixed cell size. The problem lies in the fact that the wall structure has three regions where changes in magnetization occur at very different length scales. As shown in figure 2.5, the wall is composed by a sharply localized core interacting with two extremely long tails. Numerical problems were eventually solved by Kirchner and Doring [13], by using a variable cell size in their simulation. Perhaps the most accurate analytical approach to this wall structure was developed by Riedel and Seeger [11], who separated the mathematical description into two equations: a differential equation for the core and an integral equation for the tails. The latter is linearized by neglecting the exchange energy in the tails and full solution of

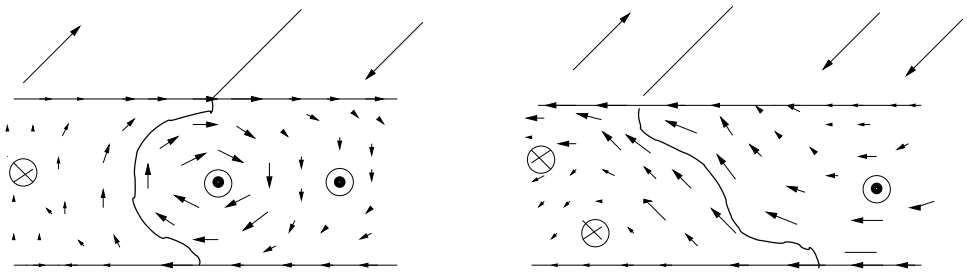

Figure 2.6: Bloch and Neél stray field free walls structures known as asymmetric walls.

the wall profile was obtained through Fourier methods.

For somewhat thicker films, commonly encountered DW structures are known as the *asymmetric* Bloch and Neél walls shown in figure 2.6. In these structures, the magnetization arranges itself in a way that minimizes dipolar charges. Note that at the surfaces, these walls appear to be common Neél walls. Both are generally classified as vortex walls. The configuration on the left is somewhat simpler than the asymmetric Neél wall on the right and appears more frequently at low fields.

The first to observe the asymmetric Bloch wall from micromagnetic simulations was LaBonte [14–16]. This result was achieved when following Aharoni's [18] idea to relax the symmetry requirement for the wall configuration. The final result revealed a significant reduction in wall energy, in comparison to the symmetric case.

If a field is applied perpendicular to the easy axis, mirror symmetry is lost and this configuration becomes unstable and this effect has been studied numerically [12]. In this situation the asymmetric Neél wall becomes more favorable. This type of wall was first presented by A. Hubert [20]. Note that the magnetization points in the same direction (the direction of the applied field) on both surfaces.

2.3 Trapping Domain Walls in Nanoscale Constrictions

As discussed in the previous sections, the geometry of a domain walls forming in a ferromagnetic structure depend strongly on the shape and dimensionality of the sample. A clear example of this was given in the previous section where we described the transition from a Bloch wall to the asymmetric "vortex" wall and finally to the symmetric Neél wall, when reducing the thickness of the film. In a similar way, drastic differences exist between the domain wall structures forming in thin films and those forming in wires and other nanostructures. The complex problem of understanding micromagnetics of DW's in nanoscale thin film elements is not yet well understood and throughout this work we have performed experiments on this type of elements with the objective of shedding some light on this intricate problem. In our experiments, we concentrate on the case of nanoscale magnetic wires where the strong shape anisotropy pins the magnetization along the axis of the wire. This however, does not exclude the possibility of domain walls existing along the wire. For example, the presence of a defect along the wire can decouple the magnetization on each side. In this case a 180° degree wall, with magnetizations lying in a head-to-head (or tail-to-tail) orientation, will form at this site. During the process of magnetization reversal for the wire, the defect will behave as a pinning site for the domain wall. R.D. McMichael et al. [163] have predicted two types of head-to-head domain walls appearing in wires, namely transverse and vortex. In the same work, they also estimate the critical dimensions for which each type of wall exists. This result, together with a schematic of these wall types are shown in figure 2.7.

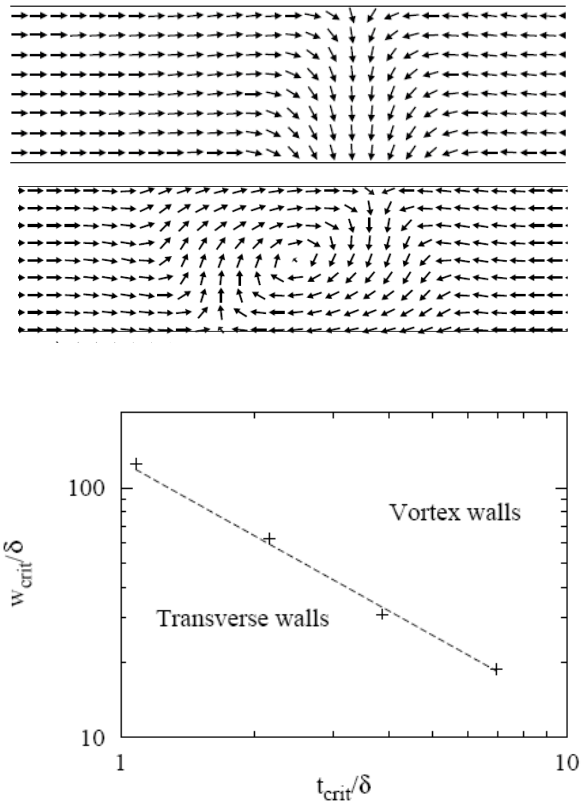

Figure 2.7: Two types of domain walls appearing in submicron wires. The relative magnitude of the exchange length and diameter of the wire determines the formation of either structure, as shown by McMichael et al. Reprinted from [163], Copyright (1997) IEEE.

P. Bruno [21] was the first to suggest that domain wall pinning sites could also be artificially induced in a wire by making a "neck" or constriction in the wire. Furthermore, he demonstrated through a simplified model, that domain wall structure can be drastically influenced by geometrical constraints and that the resulting structures may be drastically different to those obtained in bulk, i.e. in absence of constraints. Through a rather straightforward analysis he demonstrates the somewhat surprising fact that for strongly *pronounced* constrictions (this limit will be mathematically defined later on), the wall structure tends to become independent from material parameters such as magnetization, exchange stiffness and anisotropy constants, and is determined solely by the constriction geometry. Furthermore, his work reveals that the domain walls formed inside these constrictions have completely different properties than the commonly observed Bloch and Neél walls. In other words, we can expect the novel domain wall structures to form within narrow constrictions.

The analysis considers a Bloch type domain wall structure, with magnetizations confined to the yz plane. Two simplifying assumptions made throughout Bruno's analysis are that the domain wall is planar (does not bend) and dipolar interactions are neglected. The validity of the latter is later verified. The total energy of the domain wall can be calculated, as shown in section 2.1.2, by integrating the sum of exchange and uniaxial anisotropy energy density contributions. In this case however, the cross-section is determined by a function $S(x)$, so that the integral becomes:

$$E(\theta) = \int dx(A\dot{\theta}^2 + k\cos^2\theta)S(x) \tag{2.20}$$

with $\dot{\theta} = \frac{d\theta}{dx}$ and boundary conditions $\theta(\pm\infty) = \pm\frac{\pi}{2}$, and $\dot{\theta}(\pm\frac{\pi}{2}) = 0$. The structure of the wall can be found by solving the corresponding Euler equation,

which can be expressed in the following way:

$$\ddot{\theta} + \dot{\theta}\frac{\dot{S}}{S} + \frac{k}{A} sin\theta \cos\theta = 0 \tag{2.21}$$

Thus a new term, $\dot{\theta}\frac{\dot{S}}{S}$, appearing due to the geometrical constraint is found. The equation is then solved under several additional assumptions in order to calculate the profile $\theta(x)$, the energy of the wall ε and its corresponding width w. The latter is defined by $w = 4\left(\int \dot{\theta}(x)dx\right)^{-1} = 4\left(\int \dot{\theta}d\theta\right)^{-1}$. The pre-factor is chosen so that the definition leads to the corresponding width for the unconstrained Bloch width parameter $2\sqrt{\frac{A}{k}}$. The last term in the Euler equation 2.21 can be neglected, if the term $(\frac{\dot{S}}{S})^2$ is large compared to the anisotropy term. If this is not the case, this approximation will result in an upper limit for the domain wall width in the constriction. The solution of the differential equation (ignoring the anisotropy energy) leads to the following equations for wall profile, width and energy. The trick in finding this solution is noting that $\dot{\theta} = constant/S(x)$ satisfies the differential equation.

$$\theta^*(x) = \pi\left[\frac{\int_{-\infty}^{x} S^{-1}(x)}{\int_{-\infty}^{+\infty} S(x)} - \frac{1}{2}\right] \tag{2.22}$$

$$w^* = \frac{4}{\pi}\left[\frac{\int_{-\infty}^{+\infty} S^{-1}(x)^2}{\int_{-\infty}^{+\infty} S^{-2}(x)}\right] \tag{2.23}$$

$$E^* = \frac{4}{\pi}\left[\frac{\pi^2 A}{\int_{-\infty}^{+\infty} S^{-1}(x)}\right] \tag{2.24}$$

It will later be shown that these expressions are accurate whenever $w << wo$. They are also *only* useful in situations where constriction cross-section function is in fact integrable. Under these conditions, it is clear that the wall structure will no longer depend on material properties.

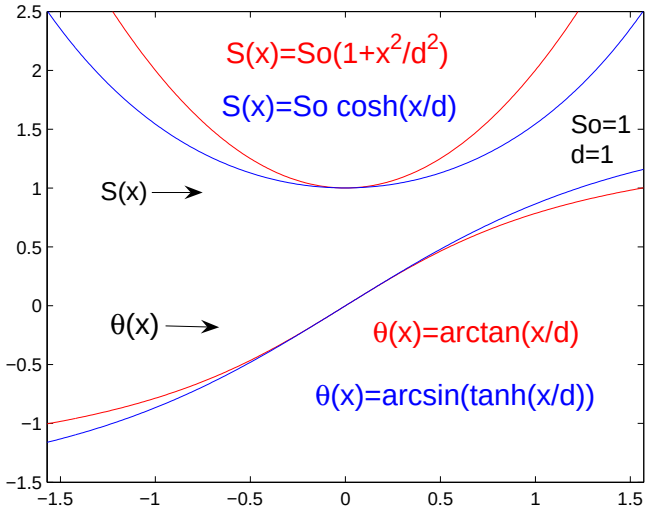

Figure 2.8: Wall profile for different constriction cross sections. Note no dependency on material properties.

For instance, for a constriction modeled through the functions:

$$S(x) = S_0(1 + \frac{x^2}{d^2}) \tag{2.25a}$$

$$S(x) = S_0(cosh(x/d)) \tag{2.25b}$$

The wall profiles are shown in figure 2.8. In order to observe what happens in the more general case of non-integral constrictions, and for a more precise solution to the problem, Bruno [21] also solves the equation including the anisotropy term. Although this equation is difficult to solve, introduction of certain clever approximations that will not be described here, allow for an almost complete analytical solution.

The important physical conclusion that can be extracted from the final solution is that there are three clear regimes determined by the relative magnitude of the ratios $\frac{wo}{d}$ and $\frac{S_1}{S_0}$ where the wall parameters behave differently. The first is

Range / Parameter	$\frac{wo}{d} \leq 1$	$1 \leq \frac{wo}{d} \leq \frac{S_1}{S_0}$	$wo/d \geq S_1/S_o$
w	w_o	$\frac{8d}{\pi}$	$w_o \left[1 + \frac{18d}{w_o \pi^2} \left[\left(\frac{S_1}{S_o}\right)^2 - \frac{S_1}{S_o} \right] \right]^{-1}$
E	$4\sqrt{Ak}S_o$	$\frac{\pi^2 A S_o}{2d}$	$4\sqrt{Ak}S_1 \left[1 - \frac{9}{\pi^2}\frac{d}{w_o}\frac{S_1}{S_o} + \frac{54}{\pi^4}\frac{d^2}{w_o^2}\left(\frac{S_1}{S_o}\right)^2\right]$

Table 2.2: Domain wall parameters for different constriction regimes.

determined by $\frac{wo}{d} \leq 1$. In this case, the wall is completely inside the constriction and therefore not influenced by it. The second, which is the most interesting appears when $1 \leq \frac{wo}{d} \leq \frac{S_1}{S_0}$. In this range the solution agrees with the initial solutions obtained when neglecting anisotropy energy, in the limit of $S_1 = \infty$. In this case, the wall geometry is uniquely determined by constriction geometry. Finally, for $\frac{w_d}{s} \geq \frac{S_1}{S_o}$, both the competition between exchange and anisotropy *and* the constriction geometry play a role. The constriction geometry is however less important. Table 2.2. shows the width and energy, obtained for each regime, for the case of a constriction determined by:

$$\begin{aligned} S(x) &= S_o \qquad\quad for \quad |x| \leq d \\ &= S_1 > S_o \quad for \quad |x| \geq d \end{aligned} \tag{2.26}$$

Chapter 3

Overview of Magnetic Force Microscopy

Magnetic Force Microscopy (MFM) was first demonstrated by Martin and Wickramasinghe [23, 24] in 1987, uses a sharp magnetic probe to generate images of the local magnetic stray field slightly above a sample. The resolution is primarily dictated by the effective radius of the point probe as well as the proximity to the surface. An image is obtained by measuring the local interaction force (or force gradient) point by point as the tip is scanned across the surface. The technique is based on the force detection capabilities of an atomic force microscope (AFM), which was invented by Binnig et al in 1986 [25, 27].

3.0.1 Atomic Force Microscopy : Principles of Operation

In AFM, a small sharp tip mounted onto a cantilever raster scans over the surface of a sample. During the scan the force or force gradient acting on the tip is recorded by means of a feedback mechanism which changes the tip to sample separation.

A scan can be performed in contact mode or in non-contact mode by using a DC or a harmonically vibrating cantilever, respectively. In DC mode the

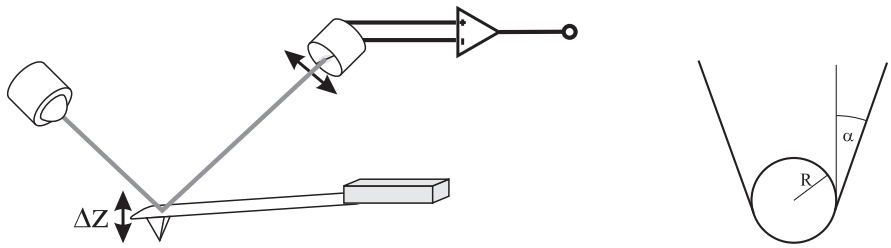

Figure 3.1: (Left) Schematic of the most common cantilever deflection detection method. A laser beam is bounced of the cantilever and then focused onto the center of a split photo detector. The difference in the signal between the lower and upper half is then a measure of the cantilever deflection. (right) Typical model of an AFM tip. The sharpness is usually characterized by its radius R and the cone angle.

force F acting on the tip leads to a deflection d of the cantilever proportional to its spring constant c according to Hook's law $F = \mathrm{c} \cdot d$. The deflection is then usually measured by interferometry. Piezoresistive cantilevers are also used where the deflection is measured by the resistive change with bending. The minimal detectable force is fundamentally limited by the thermal excitation of the cantilever which can be estimated according to the equal partition principle $d_{thermal} = \sqrt{\mathrm{k_B}T/\mathrm{c}}$. For a soft cantilever with a spring constant of $\mathrm{c} \cong 0.02N/m$ this limit is $F_{min} \cong 0.01\mathrm{nN}$.

In AC mode the cantilever is oscillated at or near its resonance frequency $f_0 = \frac{1}{2\pi}\sqrt{\mathrm{c}/m_{eff}}$. Here m_{eff} denotes the effective mass of the tip-cantilever system. The mechanical drive is usually provided by a piezoelectric bimorph. The resonance-frequency is shifted by a force gradient acting on the tip $f = \frac{1}{2\pi}\sqrt{(\mathrm{c} - \partial F/\partial z)/m_{eff}}$. This equation can be rewritten as a relative frequency

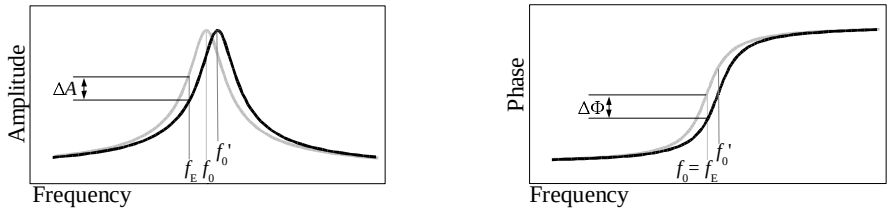

Figure 3.2: Amplitude and phase response of a cantilever. The cantilevers free resonance frequency is f_0. When a force gradient is acting on the tip the resonance frequency is shifted to f_0'. The cantilever is driven at the frequency f_E. As a result of the force gradient, the amplitude changes by ΔA and the phase by $\Delta\Phi$ respectively

shift

$$\frac{\Delta f}{f_0} = \frac{f - f_0}{f_0} = \sqrt{1 - \frac{\partial F/\partial z}{\mathrm{c}}} - 1 \tag{3.1}$$

For small force gradients the square root can be expanded into a Taylor series which leads to the approximation

$$\frac{\Delta f}{f_0} = -\frac{\partial F/\partial z}{2\mathrm{c}} \tag{3.2}$$

Therefore, to first order, the relative frequency shift is proportional to the negative force gradient. As a consequence, it can be shown that the phase will vary from its nominal 90 out of phase, relative to the driving term by

$$\Delta\phi \approx -2Q\frac{\Delta f}{f} = -\frac{Q\partial F/\partial z}{c} \tag{3.3}$$

where Q is the quality factor of the cantilever.

There are two commonly used methods for detecting the frequency shift, referred to as amplitude demodulation (AM) and frequency demodulation (FM). Amplitude demodulation is generally used in AFM operating under ambient conditions since it requires a less complicated electronics. In AM the cantilever is

excited at a fixed frequency f_E. For any driven damped harmonic oscillator the amplitude and phase of the cantilever oscillation with respect to f_E are given by

$$A(f_E) = \frac{\mathrm{A}_0}{\sqrt{\left(1 - \left(\frac{f_E}{f_0}\right)^2\right)^2 + \left(\frac{f_E/f_0}{Q}\right)^2}} \tag{3.4}$$

and

$$\Phi(f_E) = arctan\left[\frac{f_E/f_0/Q}{1-(f_E/f_0)^2}\right] \tag{3.5}$$

Q denotes the quality factor of the cantilever resonance. The curves are sketched in figure 2. Both amplitude and phase can be used to measure the frequency shift. Usually, the amplitude is used as a feedback signal whereas the phase is used to measure the frequency shift at larger distances. It has been shown [28] that the minimum detectable force gradient, with AM modulation is given by

$$\left[\frac{\partial F}{\partial z}\right]_{min} = \frac{1}{A_{RMS}}\sqrt{\frac{2\mathrm{ck_B}TBW}{2\pi f_0 Q}} \tag{3.6}$$

Here A_{RMS} is the root-mean-square of the amplitude of the driven cantilever vibration, BW is the measurement bandwidth. At first sight it may seem advantageous to increase the sensitivity of the measurement by increasing the quality factor Q. However, as was first pointed out by Albrecht et al [29], it is actually not possible to do so without sacrificing measurement bandwidth. The response time of the system, or the time it takes for the system to settle to steady vibration after a change in resonance frequency, may be expressed in terms of the time constant $\tau = -Q/\pi f$. This is the biggest obstacle in using AM under vacuum conditions. In the absence of air damping, Q is very high and the available bandwidth unacceptably low. Thus for vacuum applications FM detection for which the quality factor and the measurement bandwidth are independent, is

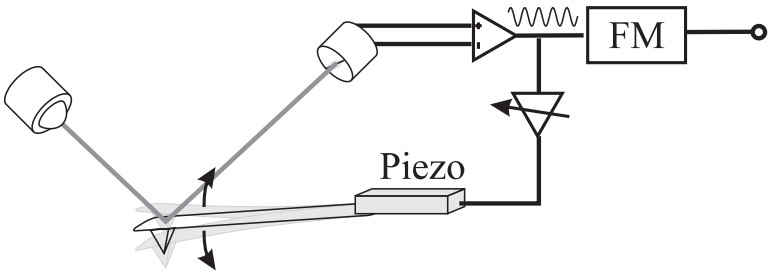

Figure 3.3: Schematic of the frequency demodulation technique. The signal of the cantilever deflection is fed back to a piezoelectric element at the base of the cantilever. Choosing the right phase within this feedback loop leads to an oscillation at the instantaneous frequency of the cantilever. The amplitude is electronically kept at a given level and the frequency of the oscillation is converted to a voltage using a frequency demodulation circuit (FM).

preferred. In frequency demodulation the signal measuring the cantilever deflection is fed back to the to the piezo element underneath the cantilever. The phase of this feedback loop is then adjusted to drive the feedback loop into oscillation at the momentary resonance frequency of the cantilever. The amplitude of the oscillation is controlled by a separate feedback loop adjusting the overall gain of the excitation feedback loop. The frequency is measured by a frequency-voltage converter. The minimum detectable force is [29] similar to the previous case equation, except for an extra factor of $\sqrt{2}$.

$$\left[\frac{\partial F}{\partial z}\right]_{min} = \frac{1}{A_{RMS}}\sqrt{\frac{4ck_BTBW}{2\pi f_0 Q}} \tag{3.7}$$

This apparent reduction in minimum sensitivity is more than compensated by the advantages that the speed of frequency change of the cantilever is independent of the Q factor. This makes this method preferred for use under vacuum conditions.

Tip-Sample Interaction Forces

Several forces govern the interaction between the tip and the sample [30]. The basis for mapping the topography of a sample is a combination of the Pauli repulsion and the Van der Waals attraction. Both interactions are usually combined in the Lennard-Jones potential. The magnitude of the resulting force is given by

$$F_{LJ} = \frac{2}{3}\pi^2 \varepsilon \rho_T \rho_S \mathrm{R}\sigma \left(\frac{\sigma^2}{z^2} - \frac{\sigma^8}{30 z^8} \right) \tag{3.8}$$

ε denotes the dielectric constant of the surrounding media, ρ_T and ρ_S are the electron densities of the tip and sample, respectively, R is the radius of the tip and σ is the typical decay length of the interaction. For distances greater than 10 nm the van der Waals part of the force decays faster as $1/z^8$ due to the retardation effect of the van der Waals interaction.

A second force is due to the electrostatic interaction between tip and sample. Its magnitude is given by:

$$F_E(z) = \frac{U^2}{2}\frac{\partial C}{\partial z} + \frac{q_\mathrm{T} q_\mathrm{S}}{\varepsilon z^2} \tag{3.9}$$

The first part describes the force due to the capacitive interaction between a conductive tip and a conductive sample. The second part is the usual electrostatic force between local charges on the tip and the sample.

Additionally, for magnetic tip and sample, the magnetostatic interaction also adds to the total force. In principle, this interaction force can be calculated from the gradient of the potential energy of the tip when brought near the stray field of a magnetic sample or via the reciprocity theorem, that of the sample when brought near the stray field of the tip.

$$\mathbf{F}_M(z) = -\nabla E = \int \nabla(\mathbf{H}_\mathrm{S} \cdot \mathbf{M}_\mathrm{T}) dV_\mathrm{T} = \int \nabla(\mathbf{H}_\mathrm{T} \cdot \mathbf{M}_\mathrm{S}) dV_\mathrm{S} \tag{3.10}$$

This interaction is the basis for MFM and will be further discussed in the following section. If the tip is brought into contact with the surface two *more* forces usually come into play. These are negligible in most cases, and only mentioned here for completeness. In air, most surfaces have a thin layer of water of a thickness of a few nanometers. This layer forms a meniscus around the tip, when it is brought in contact with the sample, giving rise to an attractive force. Furthermore, the tip itself deforms and partially 'wets' the surface leading to an adhesion force.

3.0.2 Magnetic Force Microscopy

In magnetic force microscopy the foremost goal is to separate the magnetic force from the other aforementioned interactions. In other words, the trick is to find scanning conditions under which the magnetic interaction is dominant. The obvious choice is to simply increase the magnetic moment of the tip, and has been a suitable option for bulk samples. For most thin film samples, however, the strong interaction would likely influence the magnetic structure of the sample, rendering this method ineffective. A more subtle approach is to rely on the long range nature of magnetic forces. Most of the forces decay more rapidly with distance than the magnetic interaction, with the exception of the electrostatic forces which is usually distinguishable from the magnetic contrast. A major source of image contamination is due to surface topography. The experiment, therefore, involves a two-step process of determining the texture of the surface and subsequently measuring the magnetic forces at a distance of typically 50-100 nm above the sample surface. One of the most widely used scanning modes is known as *lift mode*. In this method, two consecutive scans of the same line of the sample surface are performed. In the first scan, the topography of the sample is measured. This is

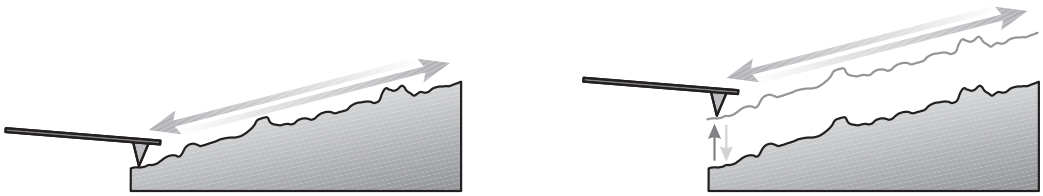

Figure 3.4: Schematic of the lift mode. In the first pass of this two step process the topography of the sample is determined for the current scan line. This information is used in the second pass to maintain a constant tip to sample distance, while measuring the force or force gradient acting on the tip. The process is repeated for all scan lines.

followed by a second scan in which a constant tip-sample distance is maintained by using the topographic information gathered in the first scan. Another method, which is less used is called *plane subtraction mode*. In this mode, only the overall slope of the sample plane within the region of interest is determined. This information is the used to measure the force or force gradient at a constant distance to the sample plane. Since the feedback system is not required and every line is only scanned once, scanning speeds can be significantly increased. However, this technique is only recommendable for relatively flat samples, for which the scan height can be set low enough for the magnetostatic forces not to be too weak.

From the numerous advance in MFM recently developed, important examples are scanning at low temperatures [31, 32], under UHV ultra high vacuum conditions [34–37] and efforts focused toward fabricating extremely sharp tips [38–41] that allow significant enhancement of the instrument resolution.

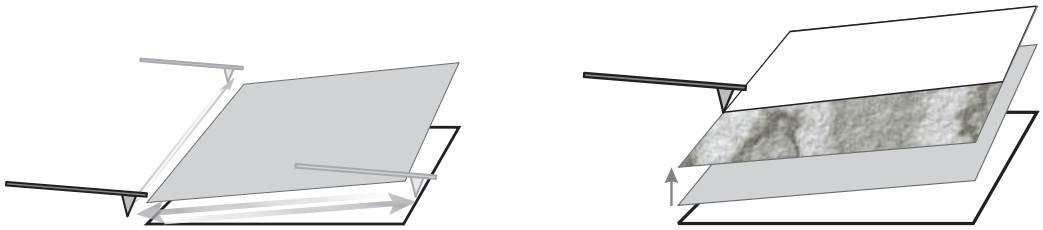

Figure 3.5: Schematic of the plane subtraction mode. First, the slope of the sample is determined along two sides of the region of interest. The information is used to extrapolate the sample plane. Then the tip is lifted up to the desired height and the force or force gradient is acquired at a constant distance to the sample plane.

Theory of Contrast Formation and Interpretation of MFM Images

The contrast observed in MFM images is a result of the magnetic interactions existing between tip and sample as expressed in equation (9). Since the magnetic properties of the tip are not always well known, the interpretation of MFM images using this formula is not straightforward. Nevertheless, analysis of the magnetic properties can be greatly simplified by introducing the "magnetic pole expansion" [42] where only the monopole and dipole terms in M_{T} are considered. The interactions take a simple form and are given by

$$\int \nabla(\mathbf{H}_{\mathrm{S}} \cdot \mathbf{M}_{\mathrm{T}}) dV_{\mathrm{T}} \longrightarrow \mathbf{F}_{monopole} = -q \cdot \mathbf{H}_{\mathrm{S}} \tag{3.11a}$$

$$\int \nabla(\mathbf{H}_{\mathrm{S}} \cdot \mathbf{M}_{\mathrm{T}}) dV_{\mathrm{T}} \longrightarrow \mathbf{F}_{dipole} = -(m \cdot \nabla)\mathbf{H}_{\mathrm{S}} \tag{3.11b}$$

where q is the effective magnetic charge of the tip and m the effective moment of the tip. Within this approximation, the total force acting on the probe is simplified to

$$\mathbf{F}_M(z) = (q + m \cdot \nabla)\mathbf{H}_{\mathrm{S}} \tag{3.12}$$

Since the cantilever deflection is mainly along the z-axis, the force further simplifies into

$$F_M^z = qH_z + m_x\frac{\partial H_x}{\partial z} + m_y\frac{\partial H_y}{\partial z} + m_z\frac{\partial H_z}{\partial z} \tag{3.13}$$

The stray field of the ferromagnetic sample H_S can be obtained from the samples magnetostatic potential $\Phi_S(\mathbf{r})$ as $\mathbf{H}_\mathrm{S}(\mathbf{r}) = -\nabla\Phi_\mathrm{S}(\mathbf{r})$. The magnetostatic potential can be calculated from the distribution of the magnetic poles in the sample surface as:

$$\Phi_S(\mathbf{r}) = \int_S \frac{d^2\hat{\mathbf{n}}' \cdot \mathbf{M}_\mathrm{S}(\mathbf{r}')}{|\mathbf{r}-\mathbf{r}'|} - \int_A \frac{d^3\mathbf{r}'\nabla \cdot \mathbf{M}_\mathrm{S}(\mathbf{r}')}{|\mathbf{r}-\mathbf{r}'|} \tag{3.14}$$

The first integral covers the surface charges induced by discontinuities of the magnetization components perpendicular to the surface. The second integral includes the volume charges originating from the divergence of the magnetization vector field within the sample. Given that the tip to sample distance during MFM measurements is of the order of 100 nm the main contribution of the force interaction stems from the magnetic poles in the sample surface close to the tip. Hence the contrast in an MFM image can be regarded as the presence of negative or positive magnetic poles. If precise characterization and calibration of the magnetic tips is available, quantitative image interpretation of MFM images can be achieved by performing numerical calculations of the interactions between tip and sample [43–46]. Several sophisticated methods have been developed for determining the effective tip moment [52–61]. Current carrying non-magnetic metallic micron-sized structures are commonly used [52, 53, 56, 57]. The shapes of these structures are chosen such that the magnetic field can be calculated with a high accuracy by using methods of conventional magnetostatics. The use of current rings for the purpose of MFM tip calibration was first performed by Kong and Chou [52, 53]. Alternatively the tips *stray field* can be measured using

Hall effect measurements [62], calibrated MFM measurements [63] and Lorentz electron tomography and holography [64–67].

Another powerful method for quantitative analysis of MFM images is based on the idea that the true image can be considered as the convolution of the tip response function [69] with the magnetic charge distribution of the sample. The instrument response function is derived by deconvoluting the tip's true field distribution from the measured image. It contains all the information concerning the tip's magnetic and geometric properties. In the work of T. Chang et al. [69] the tip response function is obtained by imaging the flux emanating from the end of a very narrow nickel strip. This single domain structure resembles a magnetic "point charge".

Chapter 4

Overview of Spin Dependent Transport

4.1 Phenomenological Models of Magnetoresistance

We begin this section by reviewing some basic concepts concerning electrical transport in ferromagnets that are instrumental in understanding the magnetoresistive effects arising in all of our experiments.

Generally speaking, the conduction electrons responsible for electrical transport in metallic systems are mostly s or p type. In contrast to this, f-states are highly localized and can not participate in this process. The d-states, however are only moderately localized and can participate in the conduction process. In ferromagnets, it is these states that specifically link electrical and magnetic properties, thereby leading to interesting effects. During the conduction process, empty d-states can be temporarily occupied by s-electrons (of the same energy) and through this mechanism the scattering becomes spin and orbital dependent. This phenomenon, commonly referred to as s-d scattering was initially studied and described by Mott in the mid 1940's. Additionally, the hybridization (linear

combinations of s and d- states forming molecular orbitals directed along certain directions/covalent bonds) of s and d-states, occurring in transition metals generates new degrees of orbital momentum in the conduction process. This process is due to the overlap of s and d bands near the Fermi Energy. It is therefore not surprising that transport measurements can indeed be a probe for magnetism. For transition FM metals, simplified models of density of states diagrams, showing 4s and 3d states, for both weak and strong ferromagnets are shown in figure 4.1. These figures illustrate the well known splitting of states, reflecting the exchange preference for spins of a given type. Both s and d-states exist at the Fermi level, but the densities of spin-up and spin-down states are not equal. The Drude model is commonly used to describe the resistivity $1/\rho = ne^2\tau/m^*$, where, n is the volume concentration of free carriers, τ their relaxation time and m^* the effective mass which is inversely proportional to the band curvature. Although the model is only directly applicable to the s-states, and does not hold when the d-states intersect the Fermi surface, several related consequences can be mentioned. The first is that the number of carriers n, will vary due to the hybridization process: s electrons become more localized effectively reducing n, while the delocalization of some d states may slightly increase the effective n. Secondly, the hybridization of s-d states results in an increase in effective mass. That is, the hybridized s states acquire the more "reduced curvature" characteristics of the d-bands. Finally, the relaxation time τ is also decreased by the possibility of s-electrons being scattered into the more localized d-states. This simple model therefore illustrates the important role of the band structure on the resistivity of ferromagnets.

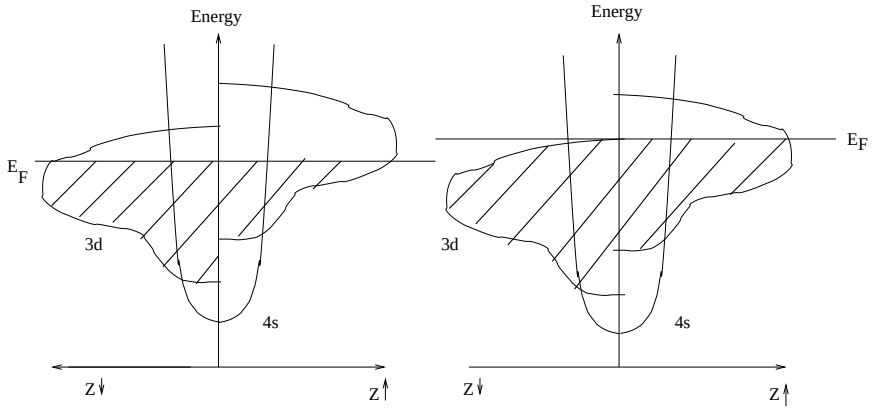

Figure 4.1: Simplified model of density of states of 4s and 3d states for weak (left) and strong(right) ferromagnets.

4.1.1 Mott's Two Current Model

Mott proposed a simple model for the resistivity of ferromagnets [70, 71]. The model is based on the fact that at temperatures below T_c, the spin direction of the carriers is conserved during most scattering events. This is because at this temperature range the spin waves that mix the two spin populations, are not strongly excited. Mott proposed that the current passing through a FM can be represented by the parallel circuit of the resistivities of each spin type as shown in figure 4.2. As explained in the previous section, in any FM the resistivity of a given spin channel will depend on the sum of all scattering contributions. This includes, phonon, impurity and most important, s-d scattering. Therefore, the resistivities of the spin channels $\rho_\uparrow, \rho_\downarrow$ are not expected to be equal in FM's.

4.1.2 Anisotropic Magnetoresistance of Ferromagnets

Electrical transport in the presence of external magnetic fields, leads to many important and interesting phenomena. These effects are commonly known as

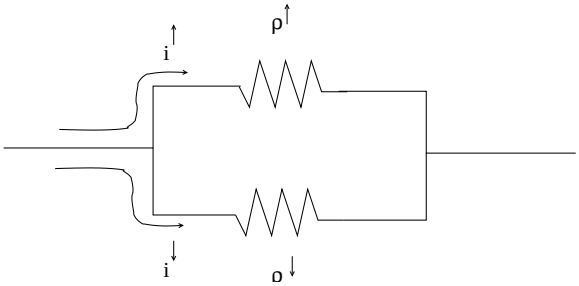

Figure 4.2: Equivalent circuit for Mott's two current model of resistivity in (transition metals) ferromagnets.

galvanometric effects and some well known examples are, the ordinary Hall effect and the anisotropic magnetoresistance (AMR) effect.

The Hall effect appears on any conductive sample that carries an electric current and is placed in magnetic field perpendicular to the current direction. The Lorentz force, acting on the carriers will cause them to deflect laterally (with respect to the current direction) generating a transverse electric field. The effect is much larger in semiconductors than in metals since the conductivity is low (yet mobility is high) enough to sustain the voltage difference (Hall voltage) between the sides of the sample.

Magnetoresistance (MR) on the other hand, refers to changes in the resistance induced by this applied field. The field initially causes a deflection in the path of the charge carriers, but once the carriers begin to orbit around the magnetic field, they cease to contribute to the current density ($< v_x >= 0$ averaged over a complete cyclotron orbit) until they are scattered. Immediately after the scattering event, the velocity of the particle will be in the direction of the applied field. From this simple description, we can conclude that the longer the relaxation times, the lower the resistivity and the larger the effects of the magnetic field on the resistance. This variation of resistivity with magnetic field is known

as magnetoresistance and was first suggested by Kohler by proposing the relationship $\Delta\rho/p = f(H/\rho)$ known as Kohler's rule. Since the deflection of a carrier in any either direction away from the current flow, increases the resistivity, the change in ρ must be an even function of the applied electric field.

$$\frac{\Delta\rho}{\rho} \propto \left(\frac{H}{\rho}\right)^2 \tag{4.1}$$

Both Hall and MR effects, normally referred to as *ordinary* in non-ferromagnetic materials, also exist in ferromagnets. For the latter however, effects are much stronger and normally referred to as *"extraordinary"*. The reason for the enhancement is essentially that the role of the external field is replaced by the internal field, which being proportional to the magnetization is much stronger. In other words, ordinary effects originate from the macroscopic flux density H while the extraordinary from the microscopic part of the M. For instance, the Hall resistivity from ferromagnets should have to two components: one proportional to the external field and one proportional to the magnetization: equivalently $\rho_H = E/J = (R_o H + 4\pi R_s M)$.

In contrast to the classical ordinary effects, the extraordinary effects are inherently quantum mechanical. The mechanism that couples the microscopic internal field to the spin of the conduction electron is the spin-orbit coupling. The two contributions can be written as a scalar sum simply because the two Hall effects have the same symmetry. The spin-orbit interaction, proportional to $\mathbf{L}\cdot\mathbf{s}$ is in the direction of the radial component of the Lorentz force. This can be shown as follows:

$$\mathbf{L}\cdot\mathbf{s} = (\mathbf{r}\times\mathbf{p})\cdot\mathbf{s} \propto \mathbf{r}\cdot(\mathbf{p}\times\mathbf{M}) \propto \mathbf{r}\cdot(\mathbf{J}\times\mathbf{M}) \tag{4.2}$$

The magnetoresistance effect is also enhanced in ferromagnets and has the attribute of being highly anisotropic. For this reason it is known as the anisotropic

magnetoresistance (AMR) effect. Generalizing Kohler's rule to ferromagnets we obtain

$$\frac{\Delta\rho}{\rho} \propto a\left(\frac{H}{\rho}\right)^2 + b\left(\frac{M}{\rho}\right)^2 \tag{4.3}$$

Representing the sum of ordinary and anisotropic magnetoresistance. At low fields, the extraordinary effects dominate, while at high fields it is the ordinary effects that dominate, since the magnetization saturates. The general form of the AMR observed in many ferromagnetic systems is given by:

$$\frac{\Delta\rho(H)}{<\rho>} = \frac{\Delta\rho}{<\rho>}\left(cos^2\theta - \frac{1}{3}\right) \tag{4.4}$$

where θ is the angle between $\mathbf{J}$ and $\mathbf{M}$.

However, the underlying mechanism behind the AMR effect in ferromagnets is distinctly different than the picture previously described for the ordinary MR effect, i.e., conduction electrons being trapped into cyclotron orbits between scattering events. If this mechanism were the dominant, then electrons traveling perpendicular to the magnetization would be trapped in orbits around the magnetization and the resistance should increase. In reality, it is observed for most ferromagnets that the resistance is actually minimized when the current and the magnetization are perpendicular to each other. Therefore, the generalization of Kohler's rule holds up only for $b < 0$.

The complexity of the AMR effect is well recognized. In fact, a complete and satisfactory model for the mechanism is yet to be developed. However, the main elements can be understood by considering the interactions of the conduction electrons with the lattice potential and impurities (ignoring exchange). That is

$$V_{scatt} = V_{Coul} + V_{SOI} + V_{exch} + ... = -\frac{Ze^2}{r} + \zeta\mathbf{L}\cdot\mathbf{S} \tag{4.5}$$

The first term, the Coulomb interaction is the strongest, while the second is the

spin-orbit interaction (SOI) directly responsible for the AMR effect. In order to understand how SOI leads to AMR in 3d transition metals, it is convenient to refer to Mott's two current model. For instance, for the case of strong ferromagnets with high $\alpha = \rho^{\downarrow}/\rho^{\uparrow}$ there are no $3d \uparrow$ holes, therefore s-d scattering is negligible in this band.

In this situation, SOI provides a mechanism for mixing of spin-up and spin-down states so that $s^{\uparrow}$ can be scattered into empty d-states. The mechanism is quantum mechanical and can be understood by expressing the SOI operator as

$$\mathbf{L} \cdot \mathbf{S} = L_x S_x + L_y S_y + L_z S_z = L_z S_z + (L^+ S^- + L^- S^+)/2 \tag{4.6}$$

where $L^{\pm} = L_x \pm iL_y$ has the effect of raising or lowering the m_l value of the state described by the initial angular momentum wavefunction as

$$L^{\pm}\psi(m_l) \rightarrow \psi(m_l \pm 1) \tag{4.7}$$

Therefore, the effect of operators such $L^+S^- + L^-S^+$ is to first lower (or raise) the spin quantum number and then to raise (or lower) the z angular momentum component. For example, the state $3d^{\uparrow}(m_l)$ will be transformed into $3d^{\downarrow}(m_l + 1)$. Comparison between cases with and without SOI scattering are described in figure 4.3. Therefore, there is an increase in resistance when there is SOI. Furthermore, these interactions depend on direction as conduction s-electrons can only scatter into 3d hole states if the conduction electron momentum $\mathbf{k}$ is in the plane of the classical orbit of the empty d state. It turns out that this only true when $\mathbf{J}//\mathbf{M}$. This explains the phenomena that resistance is minimized for $\mathbf{J} \perp \mathbf{M}$.

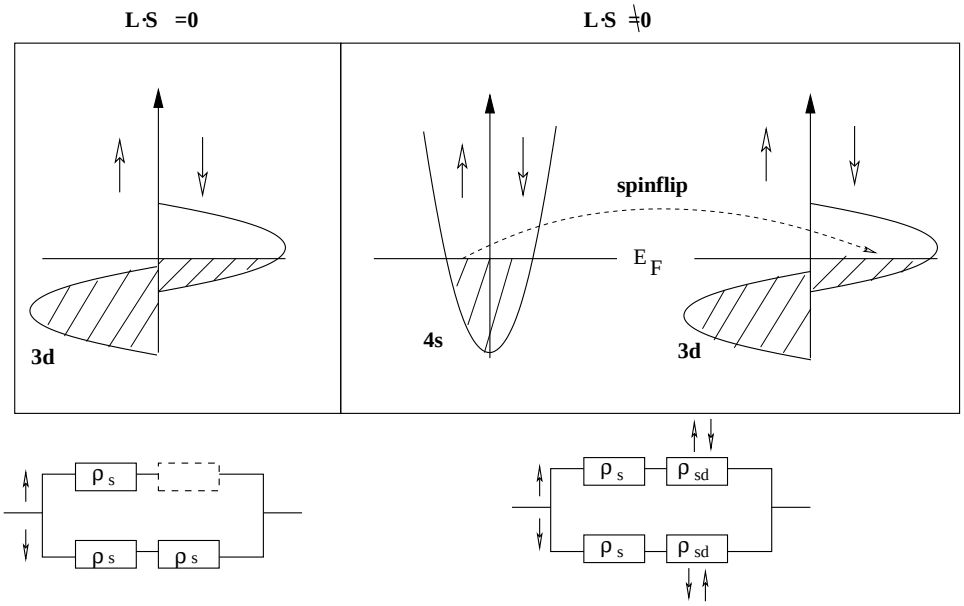

Figure 4.3: Comparison of effective resisitivity with and without SOI.

4.2 Spin Dependent Transport Through Non-collinear Magnetizations

Spin dependent transport through non-collinear magnetizations leads to interesting phenomena, which has been intensively studied in magnetic multilayers (MML) for over a decade. The interest arises mainly due to the extremely high potential for a wide variety of applications. This has already been proven to be the case for the giant magnetoresistance effect (GMR), widely used in devices such as magnetic field sensors, motion sensors and in nonvolatile magnetic computer memory (MRAM). The latter has many advantages over the conventional dynamic random access memory (DRAM). Some of these advantages are the capability to store higher density data, access the data faster (no boot-up process required) and less power consumption.

The GMR effect was discovered separately by M.N. Babich [72] and P. Gru-

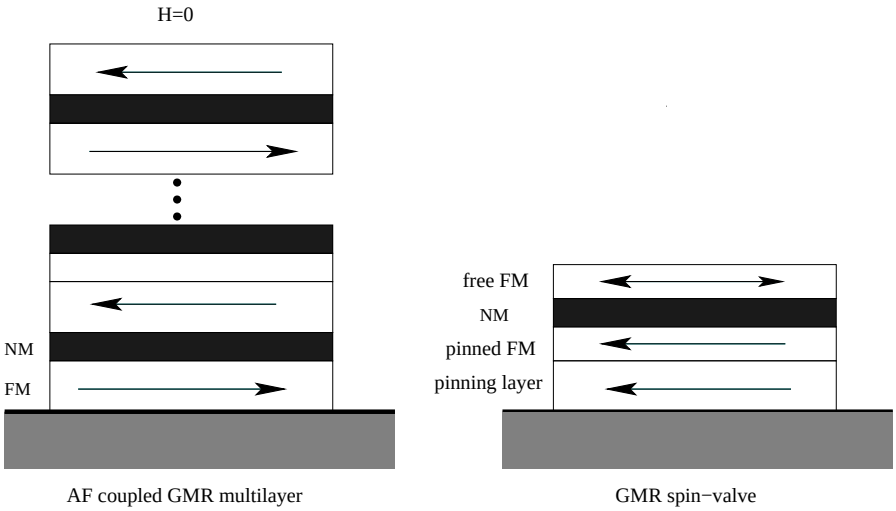

Figure 4.4: Two types of ML exhibiting GMR.

enberg [73] in the late 1980's and can be observed in any multilayer structure in which the relative orientations of the magnetizations of the individual layers can be modified and controlled through an external applied field. The field induced magnetization changes lead to large variations in resistivity when placed in a changing magnetic field, i.e., giant magnetoresistance. The amplitude of the effect is considered "giant" in comparison to the well known anisotropic magnetoresistance effect (AMR) previously used in similar magnetic field sensing applications. AMR is at most $2-3\%$ the GMR effect can reach up to 80% in magnitude. Details concerning the origin of the GMR effect are still under some discussion, however, it is largely recognized to be a consequence of spin dependent scattering of the conduction electrons traveling through the multilayer, either parallel (CIP) or perpendicular (CPP) to the magnetic layers. Typical GMR structures are antiferromagnetically coupled multilayers and spin-valves. The two structures are shown in figure 4.4.

4.2.1 Giant Magnetoresistance in Antiferromagnetically Coupled Multilayers

As can be observed in figure 4.4, AF coupled ML consist of a series of magnetic layers separated by thin nonmagnetic metallic spacer layers of a given thickness. The magnetic layers are coupled through the Ruderman-Kittel-Kasuya-Yosida (RKKY) coupling. This interaction was first proposed by M. A. Ruderman and C. Kittel [74] and describes the coupling mechanism of nuclear magnetic moments or localized inner d shell electron spins in a metal by means of an interaction through the conduction electrons.

Essential to the discovery of the GMR effect in this type of multilayers was the finding the coupling between adjacent ferromagnetic layers oscillates as a function of the thickness of the nonmagnetic layer. Also, this oscillation was found to be damped, in the sense that the AF coupling at the first peak (narrow spacer) is much stronger than at the second one (wider spacer) etc. Strong coupling is desired for biasing, so that the resistivity will peak in absence of applied field however, if this coupling is too strong, very high applied fields will be required in order to saturate the device. Thus, tailoring of the magnetic properties of the ML can be achieved by adequately choosing thickness of the layers. If the layers are AF coupled, the overall resistivity of the multilayer, depends on the magnetization directions of the individual layers. These will assume an AF arrangement in absence of an applied external field, due to the exchange coupling between them, and will be aligned in the same direction if a saturating external field is applied. When the FM layers are antialigned (aligned) spin dependent scattering of the carriers is maximized (minimized) leading to a maximum (minimum) in resistance.

4.2.2 Exchanged-Biased Spin-Valves and Magnetic Tunnel Junctions

GMR can also arise independent of the RKKY interaction. A well known example is the spin-valve. As depicted in figure 4.4 a spin-valve is comprised of a pinning layer, a pinned FM layer,a metallic spacer and a free FM layer. The purpose of the first layer is to fix or "pin" the direction of an adjacent film, which is therefore called the pinned layer. Antiferromagnetic or ferrimagnetic materials are typically used as pinning layers and it is basically the exchange coupling between these films that maintains the magnetization of the pinned layer constant. Adjacent to the pinned layer there must be a "spacer" layer that is non-magnetic and whose function is to decouple magnetically the pinned and free layers. The next layer is the free layer, which is a magnetic film of low coercivity. This film is responsible for sensing the external magnetic field. When the structure is placed in a relatively low and varying magnetic field, only the free layer's magnetization will change. Therefore relative changes between layer magnetizations can be induced leading to large variations in resistivity. As in AF coupled ML, the resistivity of the spin-valve can thus be controlled through an externally applied magnetic field. The main difference between these systems is the fields range required to saturate the magnetizations: the latter requires much lower fields due to the weaker interlayer coupling. The high field sensitivity of spin-valve devices makes them highly attractive for many magnetoelectronic applications such as magnetic field sensors.

As can be observed in the figure 4.5, the magnetization of the free layer, reverses with respect to the direction of the pinned layer for a small field range at relatively low field values. Only by applying a relatively large field, equal to

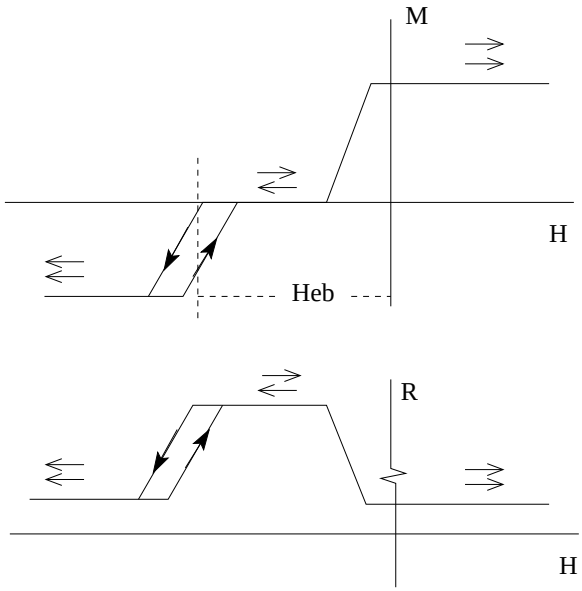

Figure 4.5: (Top) Magnetization and (bottom) resistance vs. field for an exchanged biased spin-valve.

the exchange biasing field H_{eb}, can the pinned layer be switched.

Similar effects can be observed when instead of having a pinning layer, two ferromagnetic layers of different coercivity are used. In this case, the structure is commonly referred to as a *pseudo* spin-valve. A high resistance interval will be obtained when the two layers are antiparallel. Materials commonly used for the free layers are soft ferromagnets such as permalloy and cobalt while typical pinning AF hand are FeMn and IrMn. For the non-magnetic interlayer Cu, Ag an Au have provided the most successful results. Additional buffer under/over layers are also included in order to optimize the microstructure of the magnetic layers. A clear example of this is the use of a Ta underlayer when deposited over Si(100), SiO_2 or Si_3N_4 which strongly enhances the [111] texture permalloy [Duchateau et al]. The [111] texture is desirable for more than one reason. First, it increases the strength of the exchange biasing for $Fe_{50}Mn_{50}$, secondly it decreases defect

scattering.

One final type of multilayer structure, whose operation is also based on spin-dependent-transport is the magnetic tunnel junctions (MTJ). This device is similar to a spin-valve but has the metallic spacer replaced by an oxide (typically alumina) barrier. In this case, spin-polarized tunneling through this barrier leads to even higher magnetoresistance changes at room temperature. A key difference between both types of elements is the much higher impedance of the MTJ type.

Chapter 5

Electrical Resistivity of Magnetic Domain Walls

5.1 Introduction

The idea of domain walls contributing to the electrical resistivity is a concept that dates back to the 1970's. The origin of the phenomena resides in the inability of the electron spin to track the rotating exchange field it encounters when crossing a domain wall. In other words, as the conduction electron travels through the magnetic spiral in the domain wall, it's spin has difficulty in reorienting itself parallel to the direction of the local magnetization. Therefore, the width of a domain wall is a key parameter in determining the magnitude of the effect. The narrower the DW, the larger the angle between the magnetization directions of successive atomic layers, and the larger the effects on the resistivity. As pointed out by Berger [77], for wall thicknesses much larger than the electron wavelength (as occurs in bulk strong ferromagnets) a wall represents a smooth and gradual disturbance which is not expected to reflect appreciably electron waves in a metal. This assertion was confirmed by Cabrera and Falicov [75, 76]. Their calculations, of transmission and reflection coefficients of electrons tunneling through domain walls were carried out in the diffusive limit valid when the system size is much

larger than the electron mean free path resulting from defect scattering l. The results revealed that the back-reflection probability of electrons at a domain wall was exponentially small in the ratio of the domain wall width to the fermi wavelength, $\sim e^{-\delta_{DW}/\lambda_F}$. For metals with λ_F =0.1 nm, the probability of conduction electrons scattering when impinging on a 180° domain wall, was shown to be negligible for domain walls of widths above 10 nm. Therefore, unless a wall was as thin as a single monolayer, electron scattering reflections were expected to be extremely difficult to measure.

In 1996, however, Gregg et al. provided the first experimental confirmation of the effect [78]. They measured magnetoresistance curves of a 1000 $\mathring{A}$ thick Co film with regular stripe domains. By passing a current, nominally perpendicular to the stripe domains and comparing the resistance of the sample in absence of a magnetic field, where the domain pattern exists and at high fields, where the domains walls have been completely swept out of the sample, a positive contribution from the domain walls was found. For this sample, the domain walls were estimated to be 15 nm and too wide for back-reflection scattering to account for the increase in resistivity. The additional resistivity was 0.52 $\mu\Omega cm$ for a sample of resistivity of 10 $\mu\Omega cm$. To explain his observations, Gregg argued that effects similar to those observed in GMR structures should exist when conduction electrons travel between magnetic domains, i.e., when they cross a domain walls. This follows directly from the fact that in this situation, the electrons also travel through non-collinear magnetizations.

Similar experiments, focusing on films with stripe domains, were subsequently performed by Rudiger and Kent et al. [79, 80]. In this case, the effects of micron sized Fe wires with a controlled striped domain structure were studied. Sur-

prisingly, a negative contribution from the domain wall was measured and more attention was drawn to the problem of deciphering the resistive contribution of domain walls.

The timely developments in fabrication technology, allowing the generation of nanoscale magnetic structures opened the door for a new set of experiments in which the magnetic and transport properties of domain walls could be individually probed, in contrast to previous experiments where average effects were measured for samples with multiple domain walls.

In the ideal experiment, a single domain wall is localized and a perpendicular current injected through it while maintaining the magnetizations of the adjacent domains parallel to this current and thereby simultaneously suppressing the anisotropic magnetoresistance from the domains. This situation however, with head-to-head (or tail-to-tail) magnetizations is energetically unfavorable due to the magnetostatic energy between the magnetic charges existing at the domain wall. Nevertheless, the configuration can be achieved for a narrow sub-micrometer magnetic wire in which case, the shape anisotropy pins the magnetization along the long axis of the wire. Magnetization reversal of the wire occurs through the nucleation and displacement of a domain wall. By including a constriction along the wire, the domain wall can be localized as it will behave as a trapping potential for the domain wall.

Reduced dimensions affect both the DW width and the mechanism of electron transport responsible for the DW resistance. In the limit of very narrow constrictions with dimensions lower than the electron mean free path l, domain walls become very thin and transport through the wall becomes ballistic. The term ballistic implies that conduction electrons are not scattered by defects or

impurities. For this case, enormous domain wall resistance effects are expected and the effect, known as *ballistic magnetoresistance* BMR is of great interest in the development of novel magnetoelectronic applications. In this limit, the electrical resistance becomes independent of material and geometry and is exactly 12.9 kOhms for the case of a single conductance channel. This effect has been demonstrated theoretically and experimentally under certain specific conditions. Early observation of the BMR effect was reported by N. Garcia et al [82, 83] and S. Chung et al [84]. The latter, performed breakthrough experiments while working in our group. These involved two separate rods, either ferromagnetic or half metallic, that were physically brought together through an atomic contact. The fact that this is achieved and that transport through the contact is indeed 1-dimensional can be verified by observing the electrical resistance. The measured values were found to be multiples of 12k Ohms and as showed increasing quantization steps as the rods were slowly brought together in a highly controlled manner. In this set-up, bound coils around each rod control the respective magnetization by applying DC current is applied to one rod, to pin its magnetization, while applying an AC current to the other. When the magnetizations change from an antiparallel configuration to a parallel one, huge magnetoresisitve effects are observed. The largest effects were obtained for the case of half-metallic CrO_2 contacts with magnetoresistance values near 400%. For FM contacts such as nickel, large effects up to 300% were also observed. Observation of BMR effects in planar nanojunctions has been intensively pursued. However, to date, only experiments in which patterns are formed through electro-deposition have shows this type of effects. The pursuance of this effect was one of the main motivations in this work for attempting to measure DWR in a nanoconstriction.

Pioneering work on magnetic nanowires was performed by Hong and Giordano [81], who were the first to use magnetoresistance measurements to detect the presence and propagation of individual domain walls. These appeared as discontinuous changes in resistance. The observation of this type of event was somewhat unexpected due to the tiny amounts of magnetic material that compose the domain wall. Widespread and intense research on magnetic nanowires followed and a striking diversity of experimental results [85–96] and theoretical descriptions [97–109] have been reported. Despite efforts, however, many inconsistencies within reported results remain unresolved. These inconsistencies involve fundamental issues such as the underlying mechanisms and sign of the effect. While numerous results find a positive contribution from the domain wall [88–91], many other find a negative contribution [85–87]. Experimentally, the main obstacle lies in the difficulty in isolating a single domain wall and distinguishing its contribution from other effects.

Perhaps the most widely accepted semiclassical model was the one provided by Levy and Zhang [98]. The model describes how an increase in resistivity arises from the mixing of the two spin channels with different resistivity, due to spin dependent impurity scattering at the domain wall. Further details concerning this mechanism and its mathematical representation are included in section 5.4.

The only intrinsic mechanism that predicts a negative domain wall resisitance was proposed by Tatara and Fukuyama [101–107]. In this case the origin of the effect is attributed to reduced weak localization correction due to the decoherence of the electrons by scattering at the domain wall. However, the fact that the negative resistance persists up to high temperatures [79, 85] at which inelastic scattering lengths are shorter than the mean free path, casts some doubt on this

theory.

In this chapter we present our experiments, aimed at measuring the resistive contribution of single domain walls in Py and Co. The experiments consist in performing and correlating magnetic force microscopy (MFM) and magnetoresistance measurements of nanowires containing constrictions.

The chapter has two sections. The first contains detailed descriptions of experimental techniques and results while in the second we describe Levy and Zhang's theoretical model for domain wall resistance and compare their results to our data. Although the equations in the following chapters are in cgs system of units, some measured values are given in SI units, since this system is used in the data acquisition.

5.2 Experimental Details

5.2.1 Constriction Morphology

The permalloy nanostructures studied in this section were fabricated on thermally oxidized Silicon substrates through e-beam lithography. The geometry used in the SEM mask design consists of two 200 nm wide wires joined by a 45° degree angle constriction as shown in figure (left). The lithography involved a standard lift-off method with a double layer MMA/PMMA in order to achieve a resist profile with an undercut pattern. The metals were deposited using thermal evaporation at background pressures near 1×10^{-6} mtorr. In the case of permalloy, a $Ni_{81}Fe_{19}$ evaporation source was used, in order to obtain a nominal $Ni_{80}Fe_{20}$ composition of the sample. Details concerning the specific recipes can be found in appendix 1. Figure (right) shows a preliminary trial Au/Cr sample obtained through this

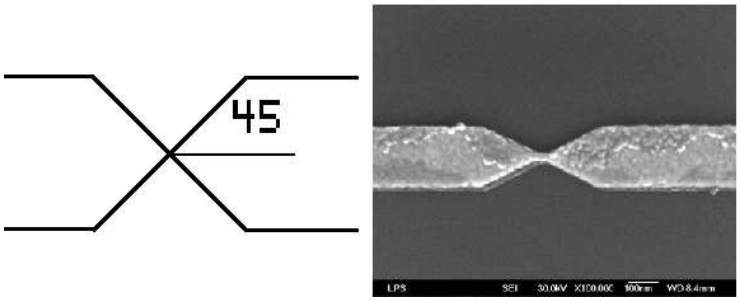

Figure 5.1: SEM CAD Mask design(left). Sem image of trial Au/Cr structure

fabrication process. The photolithography mask used for the Au/Cr contacts, shown below allows the fabrication of 20 elements per pattern, while each square pattern is 0.5 cm. In order to achieve fine control of junction widths (nanometers precision) we systematically varied the e-beam exposure dose along an array of identical structures. After fabricating several trial samples and inspecting them using the SEM we were able to determine the minimum approximate threshold dosage for our sample to *still* be connected at the junction. An example of this process is shown in figure 5.3 corresponding to doses of $320 - 380\ \mu C/cm^2$ in steps of $20\ \mu C/cm^2$. In this case, the third dose level corresponds to the desired approximate threshold. Constrictions with widths down to 5 nm were achieved through this method. MFM scanning of wires with this type of constrictions shows strong bright/dark contrast near the constriction, even in the case where magnetization is head-to-tail throughout the wire. This contrast reveals the presence of charge accumulation due to the geometry. Figure 5.4, shows an example of this for a given permalloy structure. These images were taken with a hard magnetic tip.

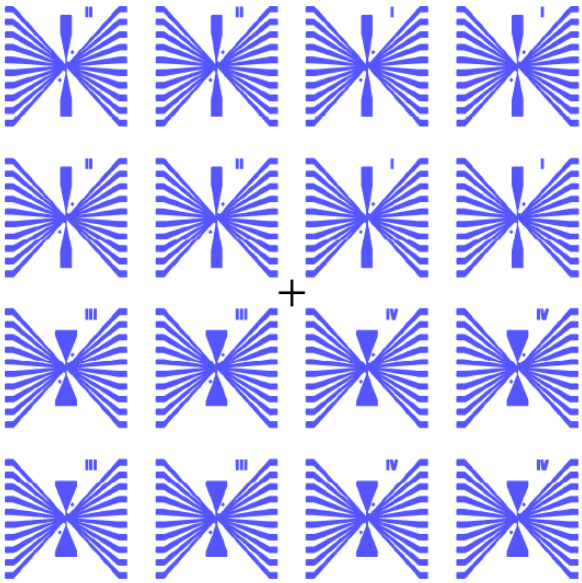

Figure 5.2: Photolithography mask design for large contact pads.

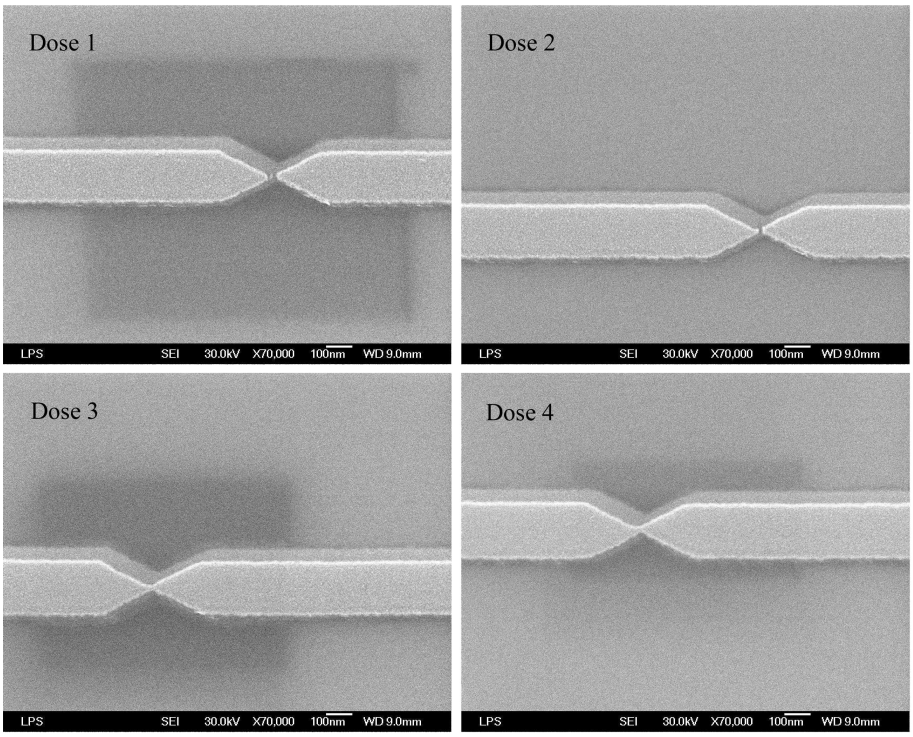

Figure 5.3: Slight variation of e-beam exposure, along an array of identical structures allowing fine control of junction width

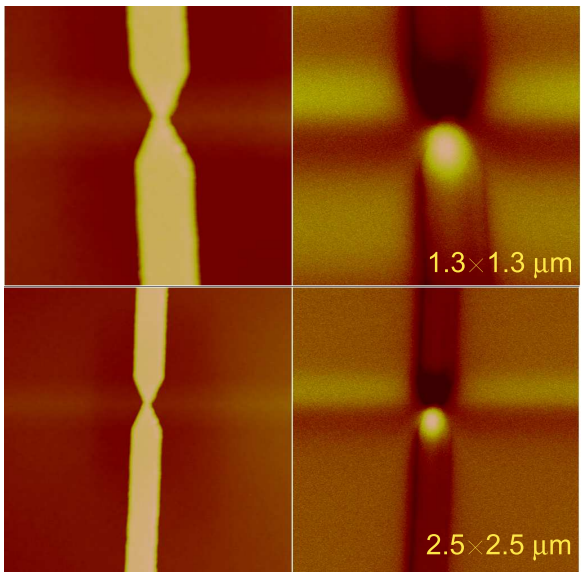

Figure 5.4: AFM and MFM images of permalloy constrictions showing shape induced magnetic charge accumulation near a constriction.

5.2.2 MFM Observation of Domain Wall Trapping

By performing MFM scanning in the presence of an external applied field, we are able to track the magnetization reversal process of nanowires with constrictions. Figure 5.5 constitutes an example of this for the case of Py wires with constrictions on the order of $\sim 20 - 40$ nm. In all cases scanning was performed at the specified field. However, initially a positive saturation field was applied leaving all magnetizations pointing upward as in cases 1 and 2. At 3, three of the visible elements have partially switched, leaving a domain wall trapped in a constriction. These domain walls appear as dark areas such as the one encircled in part 3 of the figure 5.5. As the field was continuously increased in magnitude in the negative directions, some of the elements achieve complete magnetization reversal leaving the magnetization pointing downward. In some cases, however, the domain wall was not depinned even at relatively high fields, showing the strong pinning

force of this type of constriction. In panel 7, the field has been removed and we observed that for these elements, states with a domain wall trapped in a constriction were remanent. At -350 Oe, all elements have switched to the negative direction. Other geometrical features such as "bends" in a wire can also behave as potential wells or "trapping sites" for domain walls. An example of this is shown in figure 5.6 where remanent state was induced by applying an external field in the perpendicular direction. The pinning fields in this case were found to depend on the angle.

5.2.3 MR Measurements on Angled Permalloy Wires

For our initial experiments on domain wall resistance (DWR) we fabricated patterns that consist of two wires joined by a narrow constriction and with an angle of approximately 27° degrees between the wires. The permalloy ($Ni_{80}Fe_{20}$) wires were roughly 200 nm wide and 25 nm thick. This geometry was chosen for two reasons. First, to magnetically decouple the wires, and secondly, to have a pinning center for domain walls at the junction. We focused on $Ni_{81}Fe_{19}$ because of its technological importance and the controversy that remains concerning the sign of the domain wall resistance effect [89, 90]. Figure 5.7a shows a series of the structures and the Au/Cr electrical contacts. The small rectangular pads, visible in this image, (see arrow) are additional Au pads and not to be confused with nucleation pads for the $Ni_{80}Fe_{20}$ wire. These pads are only ~ 25 nm thick, while the large Au/Cr contact structures are > 100 nm thick and suitable for wire bonding. Images 5.7 (b-c), at higher magnification, show examples of some of the fabricated junctions. The high aspect ratio of the wires promotes single domain states for both elements, as confirmed by MFM images taken at remanence and

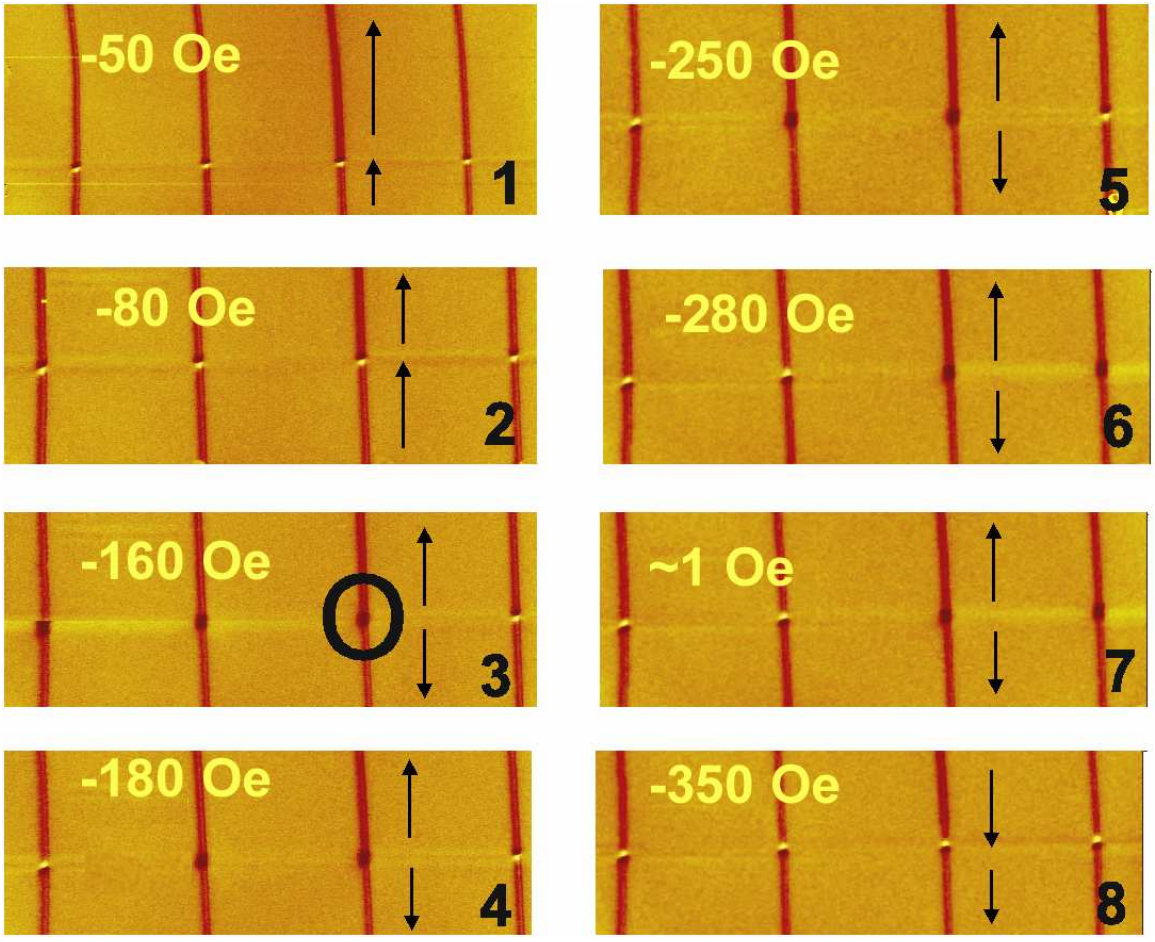

Figure 5.5: MFM under applied external field for a series of wires containing constricitons. DW trapping within the constrictions (encircled)is observed during the magnetization reversal process.

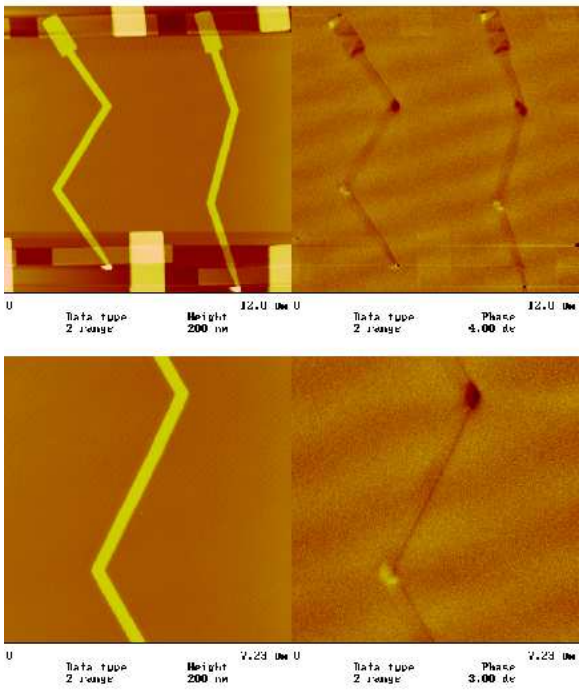

Figure 5.6: Bent wires also provide trapping sites for domain walls.

shown in figure 5.8. The bright and dark contrast at the ends and at the junction, correspond to the accumulation of magnetic charges in those regions. From the contrast one can infer that the magnetizations of the elements are connected head to tail and follow the easy axes of the respective elements. For Py, domain walls in the bulk are rather wide and on the order of $1\mu m$, while the length of the constriction is near $0.2\mu m$. Therefore the ratio $w_o/d \sim 5 > 1$ and following Bruno's theory, the domain wall is certainly determined by the pattern. The narrowest constrictions are near 5 nm, resulting in ratios $S_1/S_0 \sim 40$. For this case, Bruno finds DW's to be completely determined by the geometry of the constriction.

A representative MR curve of structures with wide junctions (∼100 nm) is shown in figure 5.9. The magnetic field was directed parallel to the axis of the short element. The MR exhibits the familiar non-linear behavior and is accom-

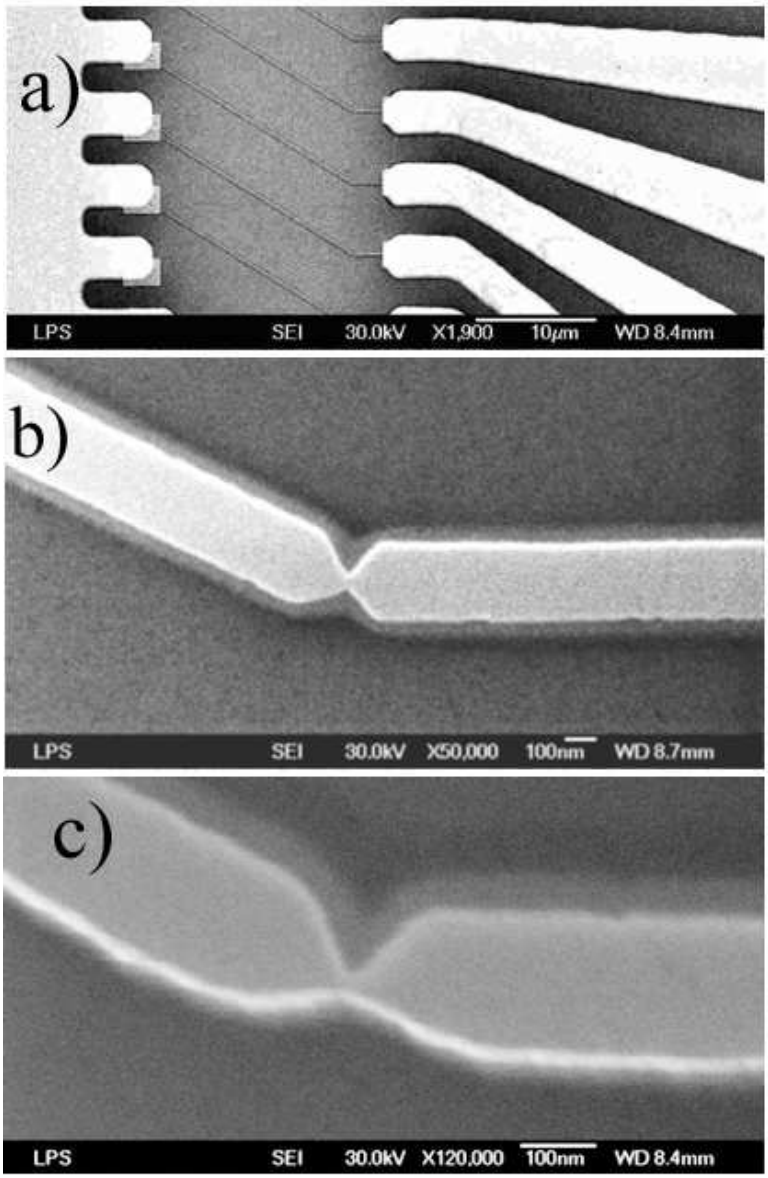

Figure 5.7: Permalloy wires fabricated through electron beam lithography. The dosage is varied along the structures in order to achieve high control of constriction width.

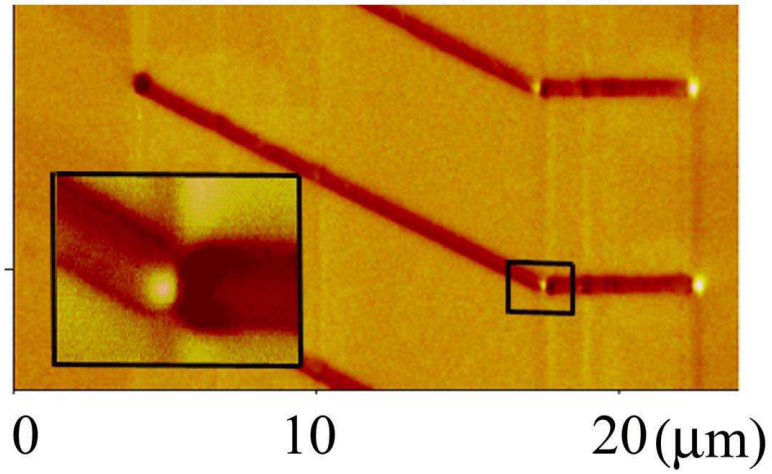

Figure 5.8: MFM images of permalloy wires at remanence. Head to tail configuration of magnetizations on both sides of the constriction can be inferred from bright/dark contrast.

panied by an abrupt upward transition at a magnetic field value $H = H_{sw2}$. The behavior is exclusively governed by the long element, since the magnetization of the short element is always parallel to the current and consequently yields negligible AMR contribution. Starting from near negative saturation the resistance increases as the magnetization of the long element becomes increasingly parallel to its easy axis, i.e., the direction of the current flow. At positive fields, the MR curve decreases more rapidly as the average magnetization rotates away from the easy axis. As the field is further increased, the magnetization switches direction at $H = H_{sw2}$. Since this element forms a 27° angle with the applied field, the magnetization after the switch will make a lesser angle with the easy axis than before. Hence, it will have less transverse component with respect to the current direction and thus produce higher resistance at $H = H_{sw2}$. Furthermore, by virtue of strong exchange and dipolar interaction resulting from a large junction area, the short element switches simultaneously and the intermediate state,

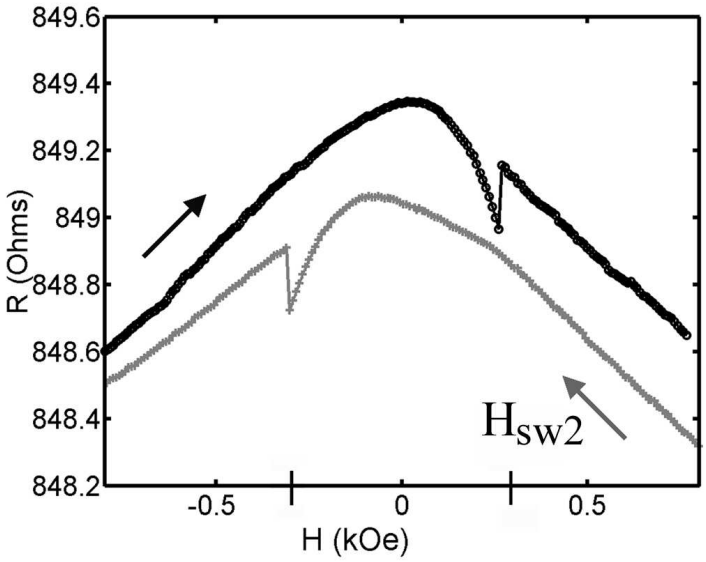

Figure 5.9: Magnetoresistance curve for wire with wide constriction ∼50nm. The dominant effect is AMR.

where opposing magnetizations are created at the junction, is suppressed. The behavior is identical in the return phase of the MR loop.

The situation is markedly different when the junction size is reduced below $\sim$ 40 nm. An example of this case is shown in figure 5.10. The main distinction is the appearance of an abrupt resistance drop at $H = H_{sw1}$ followed by a gradual decrease reminiscent of the earlier case at negative fields. The low resistance state persists within a finite field range up to $H = H_{sw2}$. The resistance jumps were found to be irreversible, and supporting data is shown in figure 5.11. The top curve is a segment of a half-cycle MR curve, which shows both negative (H_{sw1}) and positive (H_{sw2}) transitions with increasing field. In the bottom curves the magnetic field was swept from negative to positive values until the sharp drop in resistance was observed at $H = H_{sw1}$. Then, prior to reaching $H = H_{sw2}$, the field was reduced and swept in the opposite direction, as denoted by the arrows in the

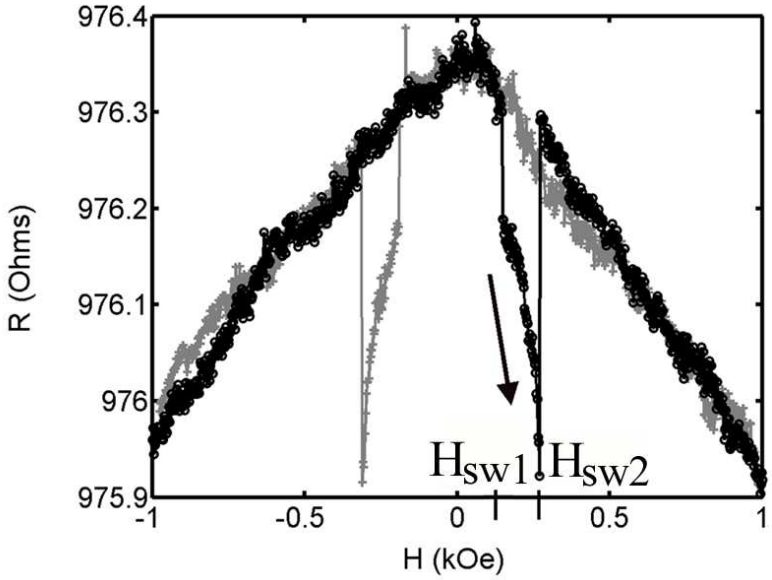

Figure 5.10: Magnetoresistance of a narrow constriction roughly 15 nm. The drop in the resistance corresponds to the trapping of a domain wall in the constriction.

figure. The low resistance state persisted past $H = 0$, and a positive transition was observed at a negative field $H = H'$ as shown. This is characteristic of an irreversible process due to a domain wall, and strongly suggestive that $H = H'$ is the field at which the domain wall is swept out of the junction accompanying the reversal of the small element. Additional insight on the low resistance state can be derived by considering the MFM images shown in figure 5.13, which show a small area enclosing the short element in its entirety. These images were obtained in the presence of external magnetic fields parallel to the short element (vertical axis in figure). The constriction is located in the lower part of the image where we observe the effects of magnetic charge accumulation. While the MFM resolution is insufficient to observe the DW structure at the junction, it is nevertheless clear that the orientation of the net magnetization of the elements can be deduced as shown by the arrows. In this case, i.e., patterns with narrow

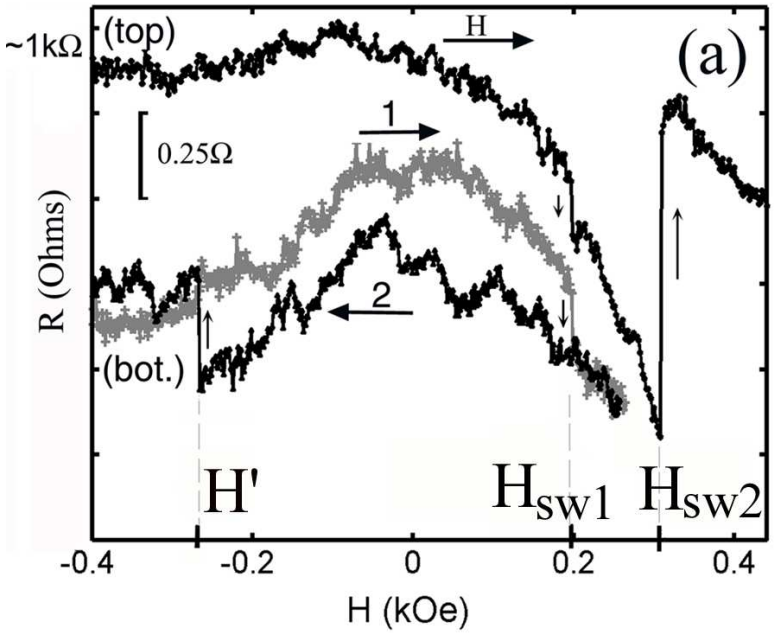

Figure 5.11: (Top) Irreversibility of trapped state in magnetoresistance curve.

constrictions, three stable magnetic states were identified. We submit that the low resistance state bounded by H_{sw2} and H_{sw1} coincides with image (II) in figure 5.13. It shows a strong positive charge accumulation characteristic of head-to-head magnetizations. The correlation can be made from independent MR and MFM measurements on the same structure. Although it would have been ideal to obtain MR and MFM simultaneously, this was not possible since the field from the MFM tip perturbed the local magnetization which introduced large fluctuations in the MR during the scan. Indeed we found, through MFM scanning in the presence of applied external field, that switching occurred earlier than for the MR measurement. This was undoubtedly due to the additional field produced by the MFM tip. Based on these observations, we suggest that the abrupt reduction of the resistance at H_{sw2} occurred due to the formation of a DW at the junction. Although the values of H_{sw1}, H_{sw2} depend on the sweep rate

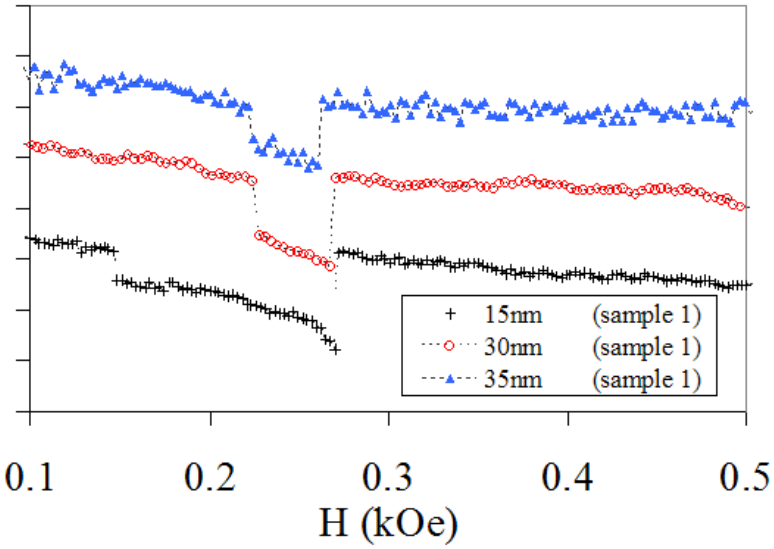

Figure 5.12: Dependence or MR on junction width.

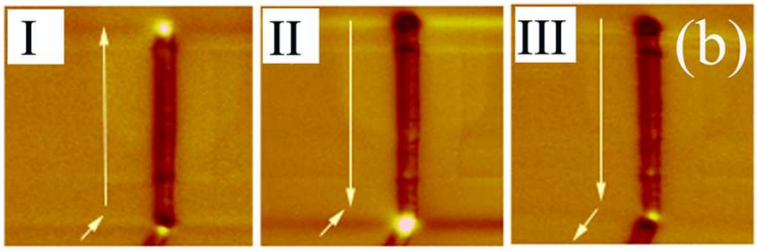

Figure 5.13: (Top) Irreversibility of trapped states in magnetoresistance curve, (bottom) three stable remanent magnetic states.

and on the value of the current, consistent with a domain wall processes, narrower constrictions seem to yield wider field ranges $\Delta H = H_{sw1} - H_{sw2}$ as shown in figure 5.12. This further supports our description since width reduction decouples the wires by reducing the exchange energy at the constriction. However, without enough statistical correlations it is hard to rule out the influence of other factors such as intrinsic switching field distributions and slight variations in the widths of element. From the data however, we can calculate the effective resistivity

contribution from the domain wall. Supposing that the resistivity in the junction changes from ρ to $\rho + \Delta\rho$, due to the presence of a DW then, the total resistance with and without the DW are, respectively $R^{DW} = \rho L/tw + (\rho + \Delta\rho)\delta_w/tw_j$ and $R = \rho L/tw + \rho\delta_w/tw_j$. Here, L is the total length, t the thickness ($t \sim 25nm$), w the width of the wire ($w \sim 200nm$), w_j the width of the junction, and δ_w the DW width. Assuming $w_j \sim \delta_w$ [21] and $L/w \sim 100$, the normalized change in resistance is given by $(R^{DW} - R)/R = (\Delta\rho/\rho)(L/w + 1)$. For the data shown in figure 5.10, changes in resistance are roughly $\Delta R/R \sim 0.03$ %, resulting in negative $\Delta r/r$ in the DW near 3%. This sharp negative drop in resistance is most probably due to the AMR effect originating from within the DW trapped at the junction. However, several other mechanisms where domain walls cause a decrease in resistance, have also been proposed [99–107].

This type of behavior was observed for numerous Py and Co samples with constrictions varying from $\sim 15-50$ nm. For samples with narrower constrictions, carrying out magnetoresistance measurements becomes very difficult. Aside from the difficulty in handling the sample, as it is extremely sensitive to electrostatic discharge, the signal to noise ratio obtained in the measurements is very low following the very low currents that the structure can withstand.

Most samples, reveal that domain walls cause a reduction in resistance, however, for a specific sample, a *positive* DWR effect with similar features was observed. This measurement is shown in figure 5.14. The constriction geometry in this case was very different than previously studied constrictions. An SEM of the sample is shown in figure 5.15 revealing a constriction that appears to be slightly below 10 nm. In this case, the magnitude of the effect is near 0.06%, which represents about $\Delta\rho/\rho \sim 6\%$ for the domain wall. This suggests that AMR may

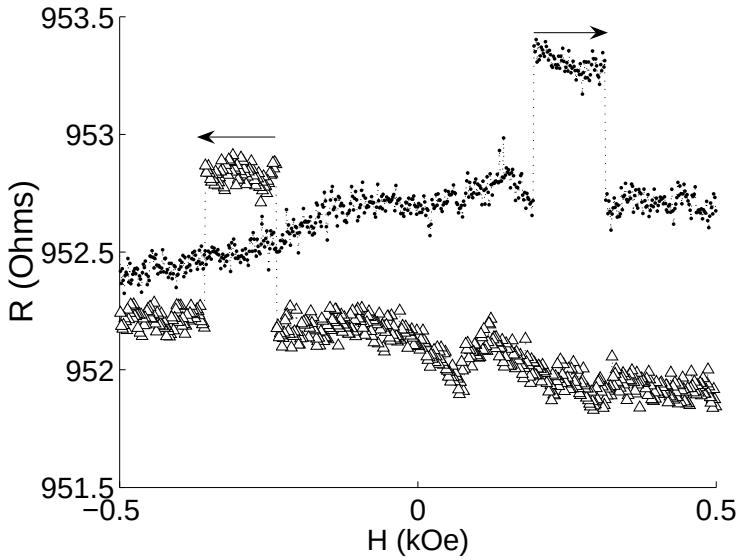

Figure 5.14: Positive resistive contribution from a domain wall trapped in a constriction below ∼10 nm.

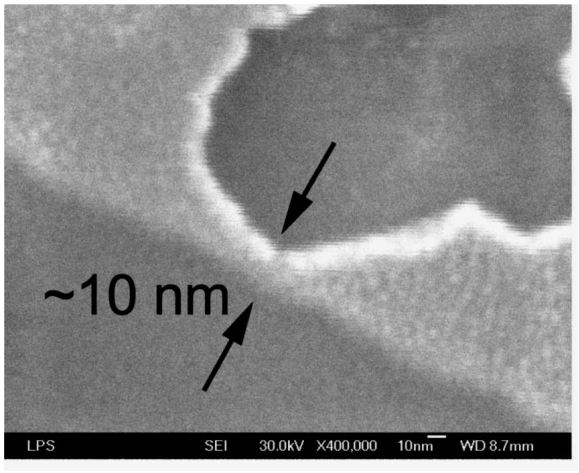

Figure 5.15: SEM of constriction corresponding to sample exhibiting positive domain wall resistance.

not be the exclusive origin of the observed domain wall resistance. In fact, this data supports the Levy and Zhang's calculation (see secion 5.4) semiclassical calculation for DWR in the diffusive limit. This formalism predicts positive domain wall resistivity varying between $5 - 10\%$. Apparently, one could argue that the reduced constriction size enhances the effect of domain wall scattering. This idea is further supported by the micromagnetic simulations presented in the following section.

5.3 Micromagnetic Simulations

Micromagnetism is a theoretical formalism which enables the prediction of magnetization distribution and magnetization reversal process in bulk magnetic materials. For submicron sized samples, numerical solutions are possible and micromagnetic simulations emerge as a powerful tool for studying these systems.

A complete review of micromagnetism and numerical micromagnetism is not included in this work. Good references for this can be found at [111, 112]. In this section we limit ourselves to briefly describing some results obtained using the NIST public software OOMMF [113]. A brief overview of the solution method implemented in this package is included as an apppendix.

5.3.1 Simulation Results

In order to understand the complex domain wall structures forming within our constricted wires, we performed micromagnetic simulation corresponding to the samples shown in figures 5.7 and 5.15. In each case a bitmap image, or mask, that define the geometry to be considered, are given as input to the software. In

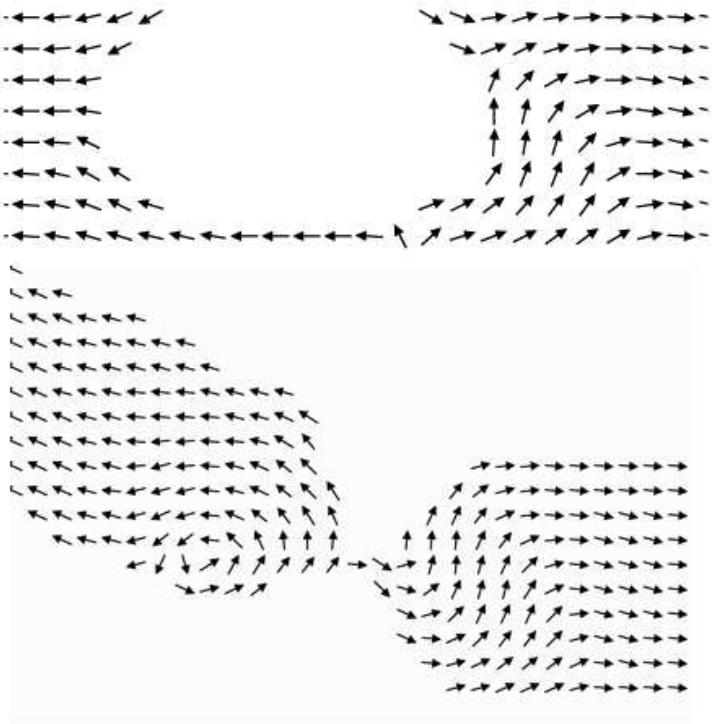

Figure 5.16: Zoom-in of domain wall structures, transverse and vortex, observed to be trapped in the two different sample geometries measured.

the numerical experiment, we emulate the real experiment in order to track the trapping of the domain wall in our simulation. That is, we initially apply a high saturating field in the positive direction, then slowly reduce the field until zero. Subsequently low fields of increasing value are applied in the opposite direction until "one side" of the pattern has switched leaving a domain wall trapped near the constriction. The main result of our simulations is shown in figure 5.18, depicting the appearance of a transverse wall for one case and a vortex wall for the second case.

Additionally, the simulation allows us to follow the behavior of the magnetization components and all energy components during the magnetization reversal

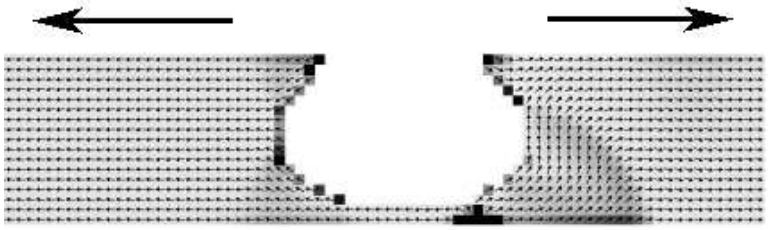

Figure 5.17: Rendition of the divergence of the magnetization for the transverse case revealing the narrow extent of this domain wall.

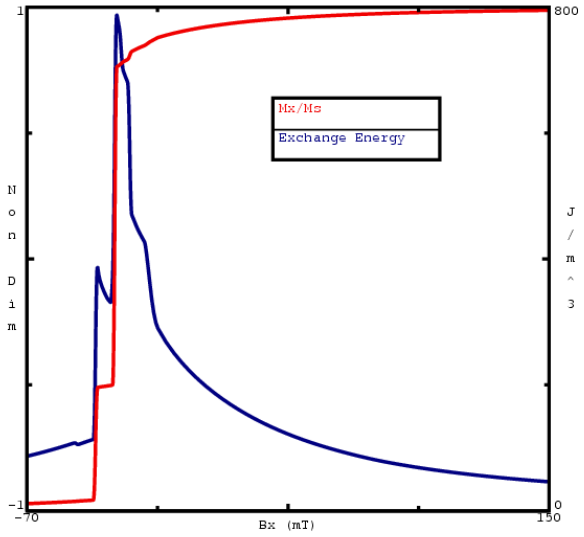

Figure 5.18: Exchange energy and transverse magnetization component as a function of applied field, for the case of the vortex wall.

process. Figures 5.18 and 5.19 show this behavior for the longitudinal component of the magnetization and the exchange energy. The latter is interesting as the first peak reveals the nucleation event for the domain wall.

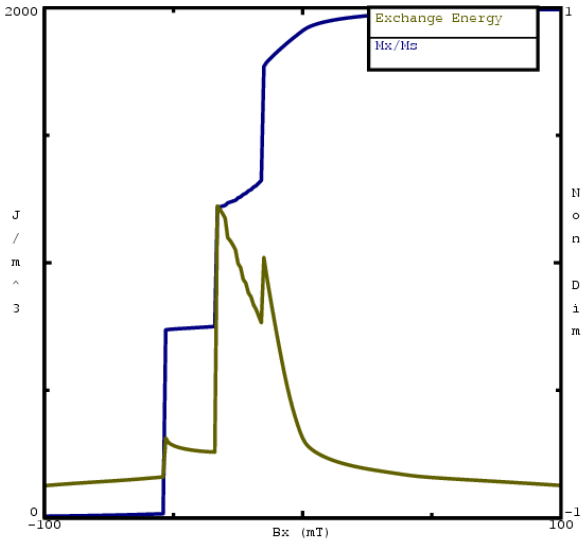

Figure 5.19: Exchange energy and transverse magnetization component as a function of applied field, for the case of the transverse wall.

5.4 Domain Wall Resistivity due to impurity Scattering at the Domain Wall

Levy and Zhang's model is based on the Hamiltonian in equations 5.3 and 5.4, commonly used to describe the GMR effect. It is separated into two parts, first a spin dependent part and second, a part that represents the scattering of electrons by impurities.

$$H_o = \frac{\hbar^2 \nabla^2}{2m} + V(\mathbf{r}) + J\sigma \cdot M(\mathbf{r}) \tag{5.1}$$

$$V_{scatt} = \sum_i [v + j\sigma \cdot M(\mathbf{r})]\delta(\mathbf{r} - \mathbf{r}_i) \tag{5.2}$$

J denotes the exchange splitting, $V(\mathbf{r})$ the non-magnetic periodic potential, and $M(r)$ is a unit vector pointing in the direction of the local magnetization. In the second expression, V_{scatt}, represents the scattering of electrons by impurities

located at positions $\mathbf{r}_i$, while j represents the spin dependence of the scattering. The solution of this eigenvalue problem is then used to calculate the domain wall resistivity through the Boltzmann transport formalism.

Although the increase in resistivity is attributed to spin dependent scattering at impurities, the scattering in itself is not the dominant source of resistance, but the fact that it leads to the mixing of spin states due to the non-collinearity of spins in the domain wall. To understand how spin-mixing causes an increase in resistivity, recall that, in general, for all ferromagnets the resistivity of one spin channel is much lower than for the other. Therefore, the resistance is always lowest in saturation state where a short circuit exists through the low resistance channel and any spin mixing causes an increase in electrical resistivity.

However, the impurity scattering potential in a uniformly magnetized sample, can not scatter between states of different spin as the spin channels are independent of each other and the electron eigenstates are pure spin states. It is the presences of the domain wall that produces a perturbation capable of mixing the spin channels.

To understand how this is possible, recall that when modeling problems involving spin, requires choosing a direction for the spin axis of quantization σ. If the magnetization is uniform, the simplest and obvious choice for this axis coincides with the direction of the magnetization. If however, another direction is specified, then the Hamiltonian may be diagonalized through a local gauge transformation, i.e. by rotating the spin operator parallel to M. This is normally done through the rotation operator given by $R_\theta = exp[-i\frac{\theta}{2}\hat{n}\cdot\sigma]$ where $\hat{n}$ represents the axis of rotation.

The rotated Hamiltonian, is diagonal in spin space and the corresponding

spinor representing the electron states are

$$H_\theta = R_\theta^{-1} H_o R_\theta = -\frac{\hbar^2 \nabla^2}{2m} + J\sigma_z \tag{5.3}$$

$$\psi(\mathbf{r}) = R_\theta \begin{pmatrix} \phi_\uparrow(\mathbf{r}) \\ \phi_\downarrow(\mathbf{r}) \end{pmatrix} \tag{5.4}$$

Inside a domain wall however, the situation is much more complex as the magnetizations are non-collinear and the angle of the magnetization varies with position. Because of this, the rotation and kinetic energy operators can become non-commuting variables and the spin Hamiltonian can not be diagonalized through the rotation operator as before.

$$R_\theta^{-1} \frac{\hbar^2 \nabla^2}{2m} R_\theta = \frac{\hbar^2 \nabla^2}{2m} + V_{pert} \tag{5.5}$$

where

$$V_{pert} = V_{DW} = R_\theta^{-1}[p^2/2m, R_\theta] = \frac{\hbar^2}{2m}(\sigma \cdot \hat{n})(\nabla\theta)\cdot - \frac{i\hbar^2}{4m}(\sigma \cdot \hat{n})\nabla^2\theta + \frac{\hbar^2}{8m}|\nabla\theta|^2 \tag{5.6}$$

This new term, represents precisely the "mistracking" of electrons crossing the domain wall, and appears as a direct consequence of the fact that momentum and position are non-commuting operators. This perturbation potential represents the interaction of the conduction electron with the domain wall and is fundamental not only in Levy and Zhang's model but in most other important DWR models such as those proposed by R.P. van Gorkom et al. [99] and Tatara [101–107].

To estimate the magnitude of this perturbation we assume a 180° degree wall with magnetization rotating continuously rotating over a distance d, or equivalently $\theta(x) = \pi x / d$ for $0 < x < d$. In this case, $\sigma \cdot n = \sigma_x(\sigma_y)$ for a Bloch (Neél) wall. For these walls, the second term in V_{pert} is zero, while the third term

represents a constant shift in the potential, with no physical significance. Then, using first order perturbation theory, the eigenstates of $H_o + V_{pert}$ are found to be

$$\psi_{\uparrow}(k_x\mathbf{r}) = \alpha^{-2}(k_x)[R_\theta \begin{pmatrix} e^{i\mathbf{k}_{\uparrow}\cdot\,\mathbf{r}} \\ 0 \end{pmatrix} - \frac{ik_x}{k_F} R_\theta \begin{pmatrix} 0 \\ e^{i\mathbf{k}_{\uparrow}\cdot\mathbf{r}} \end{pmatrix}] \tag{5.7}$$

$$\psi_{\uparrow}(k_x\mathbf{r}) = \alpha^{-2}(k_x)[R_\theta \begin{pmatrix} 0 \\ e^{i\mathbf{k}_{\downarrow}\cdot\,\mathbf{r}} \end{pmatrix} + \frac{ik_x}{k_F} R_\theta \begin{pmatrix} e^{i\mathbf{k}_{\downarrow}\cdot\mathbf{r}} \\ 0 \end{pmatrix}] \tag{5.8}$$

These states allow the calculation of the matrix elements that determine the Boltzmann scattering rates.

$$V_{kk'}^{\sigma\sigma'} = \int \Psi_{\sigma}^{+}(\mathbf{k,r}) V_{scatt} \Psi_{\sigma'}(\mathbf{k'},\mathbf{r}) d^3r \tag{5.9}$$

From these rates are the essence of the electrical resistivity calculation presented by Levy and Zhang. Their final result for the case of a current perpendicularly crossing a domain wall is

$$\rho_{CPW} = \rho_0 \left[1 + \frac{\xi^2}{5} \frac{(\rho_0^{\uparrow} - \rho_0^{\downarrow})^2}{\rho_0^{\uparrow}\rho_0^{\downarrow}} \left(3 + \frac{10\sqrt{\rho_0^{\uparrow}\rho_0^{\downarrow}}}{\rho_0^{\uparrow} - \rho_0^{\downarrow}}\right)\right] \tag{5.10}$$

Here $\rho_0^{\uparrow}$ and $\rho_0^{\downarrow}$ are the spin channel resistivities. From this plot we see that according to this semiclassical calculation, DWR varying form $5-10\%$ is expected, in agreement with our experimental result shown in figure 5.14.

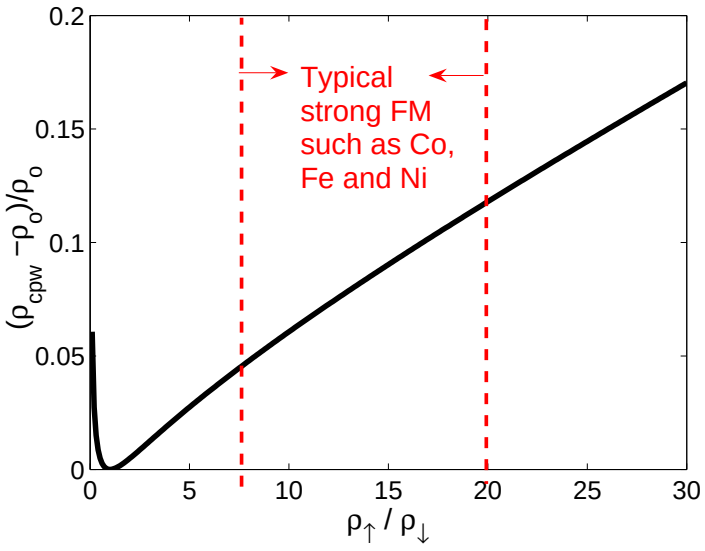

Figure 5.20: Levy and Zhangs result for DWR as a function of spin up/down ratio, for the case of current perpendicular to the domain wall.

5.5 Summary of Results

We find two types of domain walls in constricted permalloy nanowires and identify their dominant resistive contributions:

- For the vortex type wall, we find a negative contribution arising from AMR originating from the transverse components of the magnetization entering the wire in the domain wall.

- For the transverse wall, only obtained in the narrowest constrictions $\lesssim$ 10 nm we find a positive DWR effect near 6%, in agreement with Levy and Zhang's model for diffusive ferromagnets. Only in this case is the domain wall narrow enough so that its own AMR does not mask the inherent (positive) domain wall resistance (DWR).

Chapter 6

Spin Current Induced Magnetization Reversal Through Domain Wall Motion

6.1 Introduction

In the early years, *spintronics* was mainly focused on understanding the effects of magnetism on transport properties. The discovery of the *spin-torque effect* dramatically changed this and it is now well recognized that electrical currents can be a tool for changing the local magnetization. The effect is a consequence of the non-conservation of spin-current when crossing a magnetic layer, as some of the angular momentum from the current is transferred to the magnetization. The mechanism may offer an effective and efficient method for device switching thereby expanding the realm of possible magnetoelectronics devices.

Spin-transfer effects have been thoroughly studied in FM/M/FM trilayers in the CPP configuration as shown in figure 6.1. The appearance of the effect in these systems was first proposed by Slonczewski [190] and demonstrated experimentally by Myers et al. [191, 192]. In this case, the first magnetic layer acts as a spin filter and the incident polarized electrons exert a torque on the second

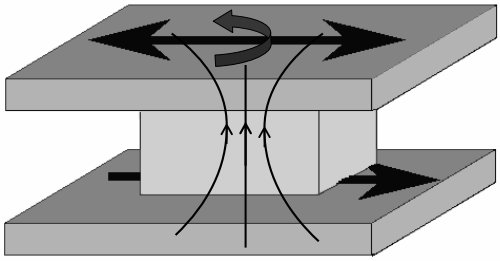

Figure 6.1: Schematic for current induced magnetization reversal in a multilayer with current perpendicular to plane (CPP configuration)

layer. For currents above a given critical current, the torque can lead to complete magnetization reversal, confirming the feasibility of current controlled magnetic memory cells. However, the currents required for this may be too high for industrial implementation. In this work, we focus on another scheme for locally modifying magnetization through applied electrical currents, i.e., by using the current to displace domain walls. The idea was first proposed by Berger in the late 1970's [77, 127] and has attracted considerable attention since. Early MFM observations of the effect were provided by L. Gan [149], while working in our group. In this case 90° and 180° degree Bloch walls in 20 μm side strips of Py, 160 nm thick, were moved through current pulses. Berger performed similar experiments [138, 139] on continuous Py films 263 nm thick but using kerr-contrast microscopy to observe the effects of current pulses on the position of Bloch walls.

The dominant interaction between conduction electrons and domain walls is in most films, which are typically thicker than $\cong 0.1\mu m$, is the *hydromagnetic domain-drag* forces [127] resulting from the Hall effect. The non-uniform current distribution at the wall leads to eddy current loops circling the wall, as shown in figure 5.2, where the the current is decomposed into a uniform distribution plus a

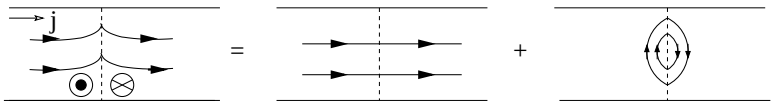

Figure 6.2: Non-uniform current distribution at the wall decomposed into a uniform distribution plus a DC eddy current loop circling the wall. The field generated by the current loop exerts a dragging force on the domain wall.

DC eddy current loop circling the Bloch wall. The field generated by this current loop exerts a force on the domain wall, thereby dragging it. This force can be modeled by considering the basic equation for the force per unit area, exerted on a domain wall by a magnetic field, $2M_sH$. By expressing the field in terms of wall velocity and wall mobility $\mu = v_w/H$ we can write

$$F_x^{drag} = 2M_s\mu_e^{-1}(R_1 j - v_e) \tag{6.1}$$

where μ_e is the eddy current limited wall mobility and R_1 the anomalous hall constant. It can be shown [142] that $\mu_e \propto \frac{1}{t}$ where t is the sample thickness and that this interaction becomes negligible for films with thickness below $\cong 0.1\mu m$. This force however, is not the only force resulting from the interaction between conduction electrons and domain walls.

In the early 1980's, Berger proposed the existence of another effect based on the *s-d exchange interaction*, capable of displacing domain walls, even in very thin films. To describe the origin of the effect, we track what occurs to the conduction electron as it crosses a domain wall for the *almost adiabatic* case, applicable to the case of wide walls. Before entering the domain wall, the electron spin is aligned with the local magnetization in the domain adjacent to the wall. As it enters the wall, the local magnetization begins to rotate and although the electron spin tries to adiabatically follow the local magnetization, a small angle α starts to build up

between the spin and the local magnetization. As $\alpha > 0$ the electron spin starts to precess around the local exchange field from from the wall. At the end of the wall, the electron has flipped its spin (in the case of a 180° degree wall) and has therefore given a quantum $\hbar$ of angular momentum to the wall. Since the total angular momentum of the system is conserved, a torque of equal magnitude and opposite sign is applied on the magnetization of the wall.

This idea raised a new challenge for experimentalists in the field. That is, to confirm the effect of current induced domain wall motion for the (non-Bloch type) domains walls forming in thin films and nanoscale wires. The first experiments on submicron-scale patterned wires were perfomed by Tsoi et al. [169]. In these experiments, magnetoresistance measurements were used to show that domain wall motion could be triggered by an electrical current in the presence of low magnetic fields. Verification of the effect in *absence* of any applied magnetic field came sometime after in the works of [152, 181] as well as our own work presented in this chapter [161].

Figure 6.3 explains the basic concept behind our experiments on current induced magnetization reversal in nanowires. By displacing a domain wall between two constrictions along a wire, the magnetization of the section of the wire between the constrictions is completely reversed. Although the process of magnetization reversal through DWM was for a long time considered inadequate in terms of speed, recent theories [157, 165], simulations [155] and experiments [152], point toward the possibility of fast reversal through CIDWM. Furthermore, these studies indicate that the presence of even weak magnetic fields can dramatically boost the speed of the DWM. In the case of magnetoresistive random access memory MRAM, advantages offered by the CIDWM approach are lower power

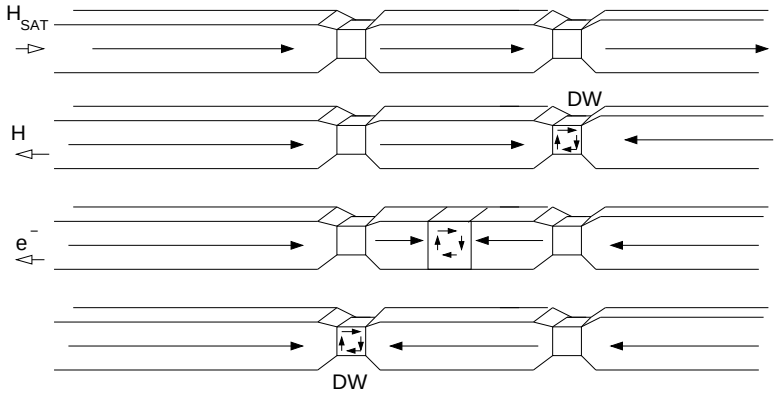

Figure 6.3: Concept behind current induced magnetization reversal.

consumption, crosstalk reduction during the writing process and simplified device architecture, making this technology extremely attractive. Yet understanding and controlling this phenomenon in real structures is a demanding task. First, the interaction between conduction electrons and a DW in presence of applied fields leads to complex dynamical behavior due to various coexisting physical processes. Secondly, the behavior will depend on the intricate DW micromagnetic structure determined by the nanostructure geometry. Thus, quantitative correlations between field and critical currents in CIDWM can shed light on these effects and may ultimately optimize the control and efficiency of the mechanism. We begin this section by describing my experimental observations concerning the spin-torque effect. This is followed by Berger's phenomenological description and estimation for the s-d exchange interaction responsible for triggering the motion in thin films. Next I will focus on the problem of modeling the dynamics of current induced domain wall motion. I will begin by reviewing the simpler case of domain wall motion in presence of a DC magnetic field and in absence of applied spin currents. This will serve as a basis for understanding Zhang and Li's model, where spin-torque is added to the problem. The results from these models are

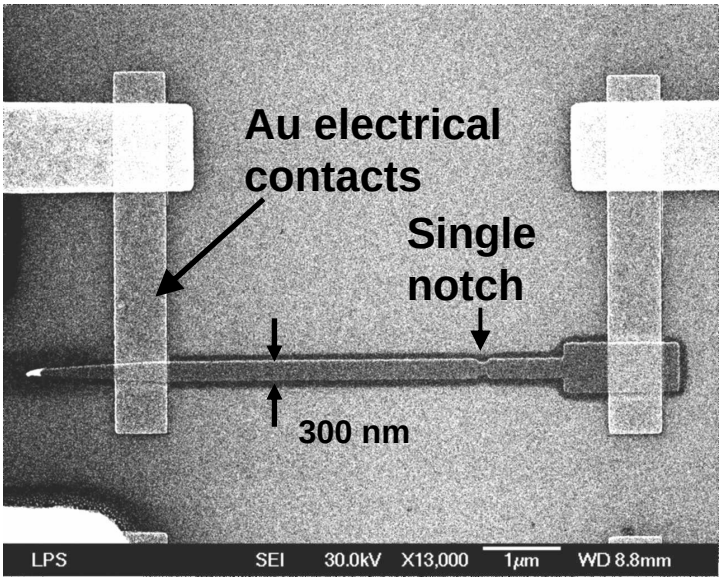

Figure 6.4: SEM micrograph of single notch sample with electrical contacts.

compared to our experimental observations.

6.2 Spin-Torque Experiments

6.2.1 Domain Wall Motion Along a Wire

Experiments were carried out on 300 nm wide $Ni_{81}Fe_{19}$ wires 30-40 nm thick, fabricated over thermally grown SiO_2 substrates through e-beam lithography following the standard lift-off process described in the appendix.

Figure 6.7 shows MFM scans of a section of a nanowire containing a domain wall. Each image on the right side was taken after scanning the image on its left and applying a voltage pulse across the wire. The magnitude of the applied peak voltage is specified for each experiment. A low moment MFM tip was used in order to minimize tip effects on the position of the domain wall. Data of displacements vs voltage, collected from experiments of this type is shown in

figure 6.8. The data confirms that the displacements are in the same direction as the injected conduction electrons. However there is significant dispersion in the measured displacements for currents near the critical value.

6.2.2 Reversible Domain Wall Motion Between Two Constrictions

In the next set of experiments, complete magnetization reversal of a section of the wire was attempted as described in the schematic in figure 6.3. In this case the wires were also 300 nm wide and 40 nm thick but contain *two* constrictions each roughly 220 nm wide. Following other similar studies [169], the elements are asymmetrical, as shown in figure 6.9, with a nucleation pad on one side and a sharp end on the other, ensuring DW nucleation from only one direction and the reproducibility of the process. The underlying Cr/Au electrodes were included to allow current injection through the magnetic element. AFM/MFM scans of a typical sample are included in figure 6.7. Experiments were performed by applying concurrent applied magnetic fields H_{app}, and electrical currents to the sample and by using magnetic force microscopy (MFM) to evaluate the resulting effects. The samples were magnetically initialized by saturating the magnetization in the upward direction. Figure 6.16a shows an AFM of a section of the wire near the constrictions. Part b of this figure shows MFM of this same are at remanence after saturation. Subsequently, we swept H_{app} in the opposite direction until a DW nucleates from the lower pad edge and propagates towards the lower constriction. At this point, the section of the pattern below the lower constriction has reversed the direction of its magnetization. This switching event typically occurs near H_{app}= -165 Oe. After removing the H_{app}, MFM images as

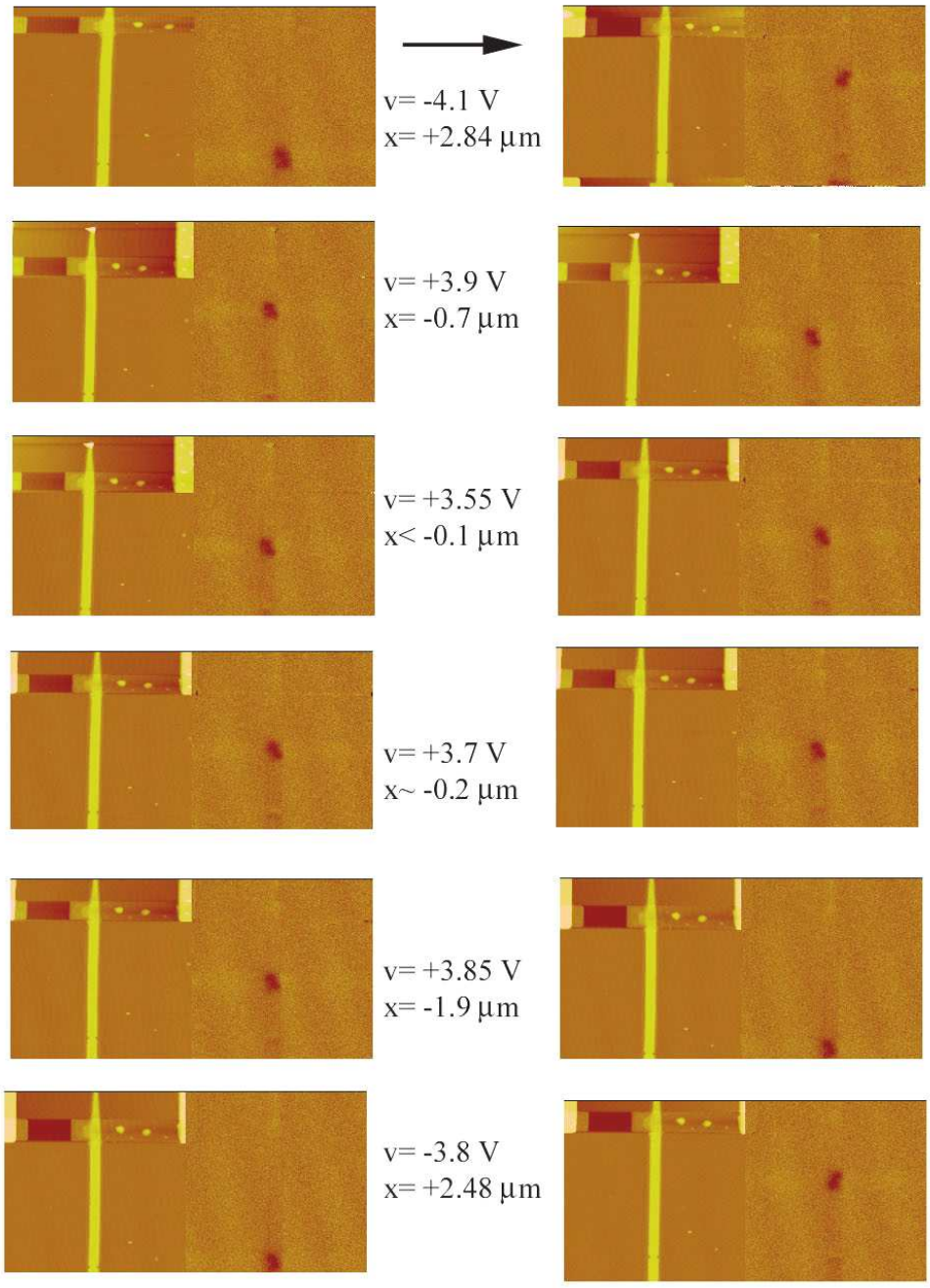

Figure 6.5: MFM images of Py wires, before (left) and after(right) applying the indicated DC voltage to the wire. The images show the corresponding induced displacements. The wires are 300 nm wide and 20 nm thick with $R \sim 1k\Omega$, corresponding to current densities on the order of $10^{11} A/m^2$.

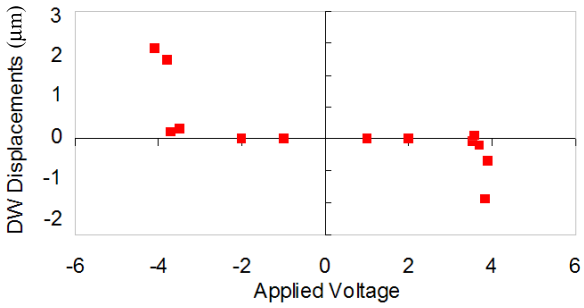

Figure 6.6: Domain wall displacements vs. applied voltages corresponding to the images shown in figure 6.4. The data illustrates the correspondence between the direction of the domain wall motion with the direction of electron flow.

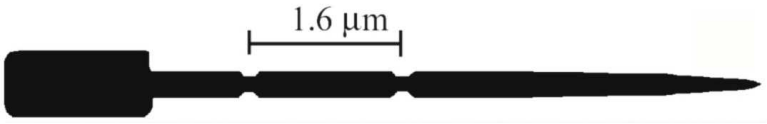

Figure 6.7: Bitmap of pattern geometry used for experiments on current induced magnetization reversal through domain wall motion.

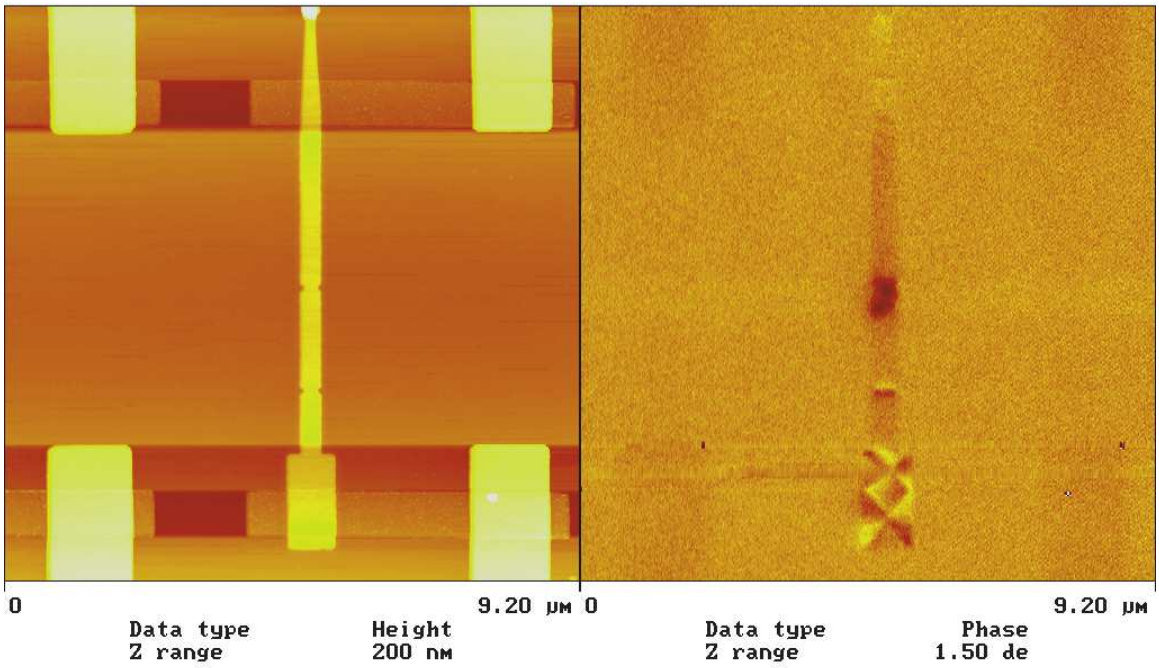

Figure 6.8: AFM/MFM images of permalloy nanostrucutres fabricated for experiments on current induced magnetization reversal through domain wall motion.

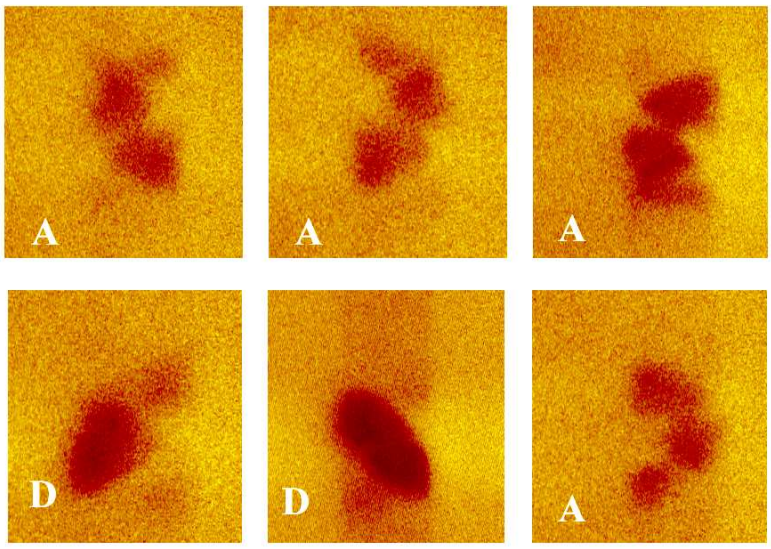

Figure 6.9: MFM images showing the types of domain walls found to be trapped within the constrictions. The six configurations identified are vertical and horizontal mirror images of two basic types labeled 'A' and 'D'.

in figure 6.19c, confirm the capture of a tail-to-tail (or head-to-head) DW in the lower constriction. The magnetic configurations, with a DW trapped in either constriction, were found to be stable and not affected by a low moment MFM tip. Figure 6.8 shows MFM images of the six types of DW's, which were observed to be trapped in a stable manner within the constrictions. It is readily apparent that each structure can be obtained from horizontal and vertical mirror reflections from two basic structures, labeled 'A' and 'D'. Type 'D' shows an accumulation of magnetic charge at the constriction forming a line diagonal to the axis of the element. A schematic of this wall is shown in figure 6.9. Type 'A' is more complex, but the magnetization distribution can be visualized by means of micromagnetic simulations. By using the public OOMMF simulation code with standard parameters for NiFe, $M_S = 8.6 \times 10^5 A/m$, $A_{ex} = 1.3 \times 10^{-11}$ J/m and with a cell size of 10 nm, we were able to numerical reproduce the magnetiza-

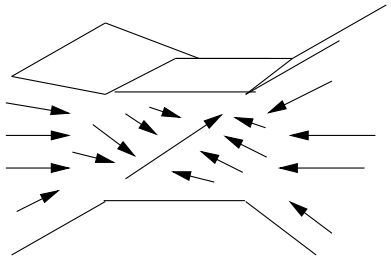

Figure 6.10: Schematic of inferred magnetization configuration for the 'D' type wall. The wall is transverse with diagonal charge accumulation.

tion reversal process of our patterns. This includes observation of domain wall trapping within each constriction. In the simulation we first saturate the sample along its its easy axis. Subsequently, the field is reduced in steps of $10Oe$. Stable micromagnetic configurations are found at each field. After passing the zero field boundary, fields of opposite direction and increasing magnitude are applied (also increasing in steps of 10 Oe). We observed that a positive field near 167 Oe, a domain wall that has formed in the nucleation pad on the right, sweeps through the sample leaving the section behind with reversed magnetization direction. This domain wall is trapped in the constriction and this state is stable for a field range. At a somewhat higher field, the domain wall moves to the constriction on the right. Micromagnetic distributions with domain walls trapped in a constriction are shown in figure 6.10. In each case there appears to be a vortex type structure trapped near the constriction. Note that these simulations predict with remarkable accuracy the experimental switching field values. Figure 6.11 shows a zoom-in of trapped domain wall (a) together with rendition of the divergence of the magnetization in pixel shading shown in figure (b). An MFM of the actual domain structure is also included (c) in order to corroborate the

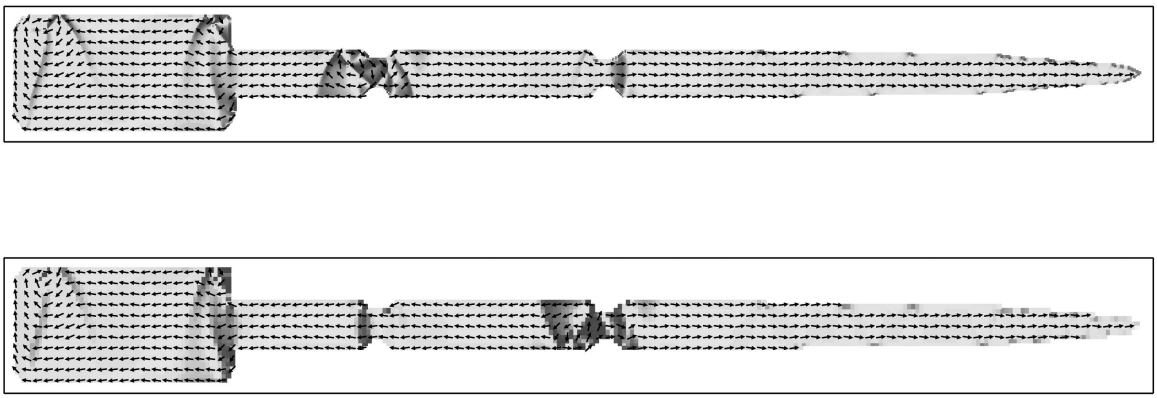

Figure 6.11: Two intermediate states arising during the magnetization reversal process simulated using OOMMF (micromagnetic simulator). These states show a domain wall trapped in either the left (top) or right (bottom) constrictions. Pixel shading represents divergence of the magnetization.

resemblance.

The next set of experiments involved applying current pulses through the patterned wire in order to observe its effect on a trapped domain wall. The pulses had rise times near 20 ns and were exponentially decaying with fall times on the order of 1 μs. Interestingly, we observed that by applying pulses (of either polarity) above a certain excitation threshold ($\sim 5 \times 10^{11}$ A/m^2) yet below the motion threshold ($\sim$ 7.5 $\times$ 10^{11} A/m^2), the pattern could be transformed from one domain wall type to another. Examples of observed transformation and the corresponding peak voltages are shown in figure 6.12. Although we did not measure a large enough number of events to statistically characterize these events, we can say that the vortex state appears with much higher frequency than the transverse state. This is not surprising since it should be a lower energy state. This is evidence of Berger's description [137] that the current pulse may "jiggle" the DW thereby exciting modes of DW oscillation, and subsequently relaxing into

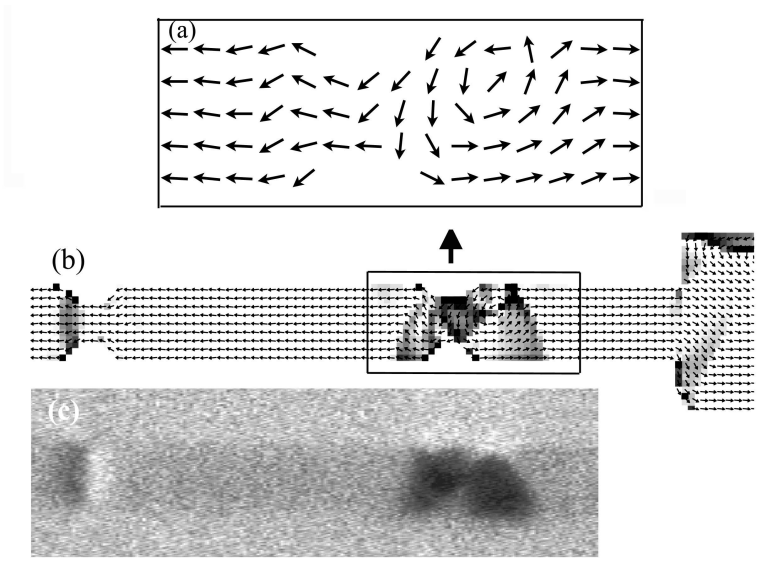

Figure 6.12: (a) Zoom-in of magnetization distribution at constriction, showing a vortex structure on one side of the constriction, (b) pixel shading represents the divergence of the magnetization in order to allow direct comparison with MFM image shown in (c).

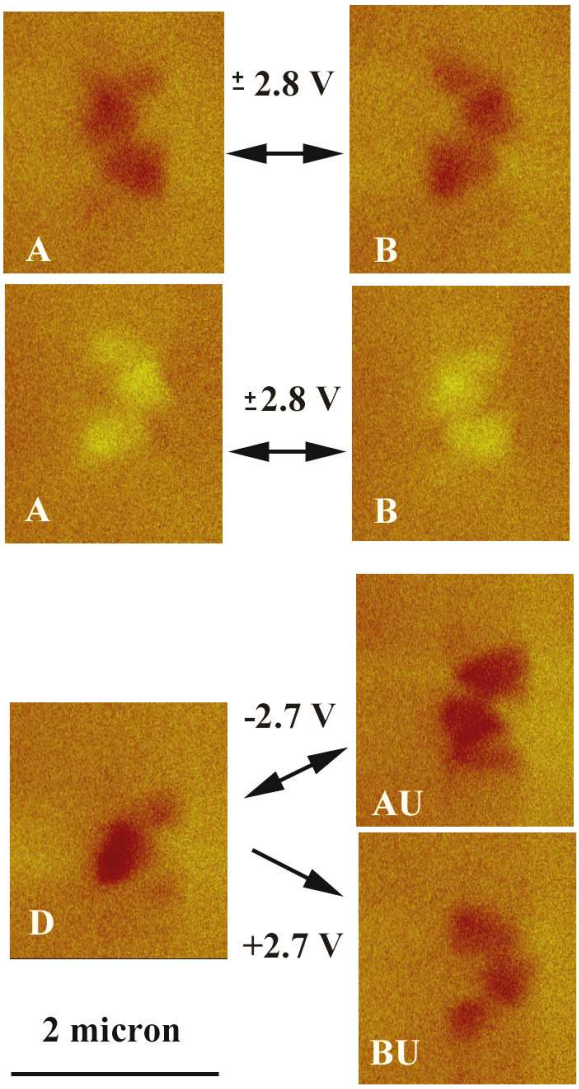

Figure 6.13: Observation of current induced domain wall transformations. Fast rising (20 ns) and exponentially decaying ($1\mu s$) pulses of the specified amplitude were applied to the constricted wire holding a domain wall. The arrows indicate the observed transformations and the peak voltage.

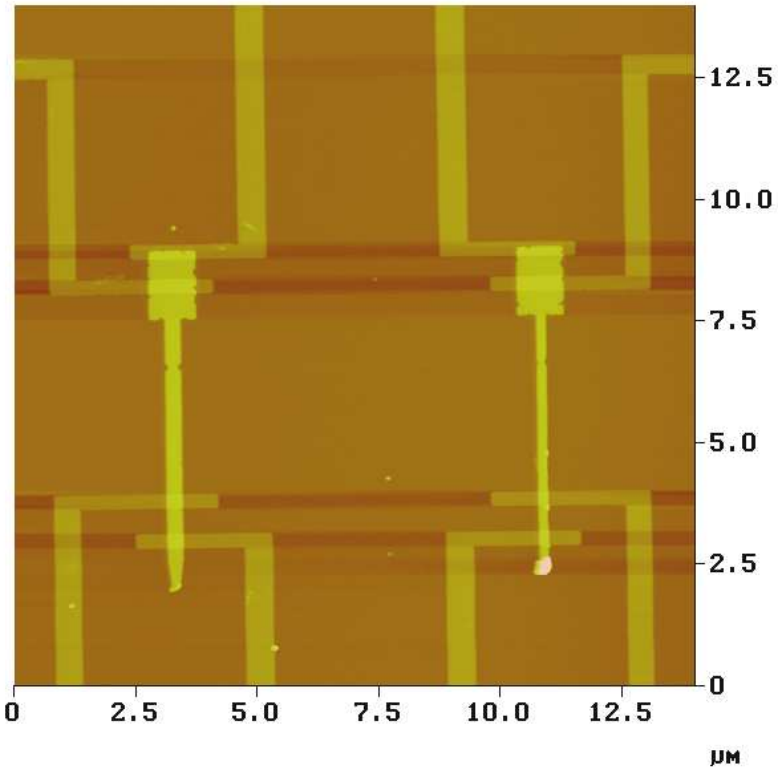

Figure 6.14: AFM of (left) 200 nm wide wire and (right) 100 nm wide wire and their electrical contacts.

one of the six available states.

Experiment were only carried out with vortex type walls as trapping transverse walls proved to be a highly unprobable event. In an attempt to promote the formation of transverse walls, we fabricated narrower wires. An example is shown in figure 6.13 with two wires: a 200 nm wide wire on the left and a 100 nm wide wire on the right. In figure 6.14 we compare the domain walls trapped in each of these cases. In this figure the narrower wire is on the left and it appears to approach a diagonal wall. For the narrow sample, however, the domain wall appeared to be much more sensitive to MFM tip induced effects. Even with a low moment tip, we observed tip-dragging effects as shown in figure 6.15. This was

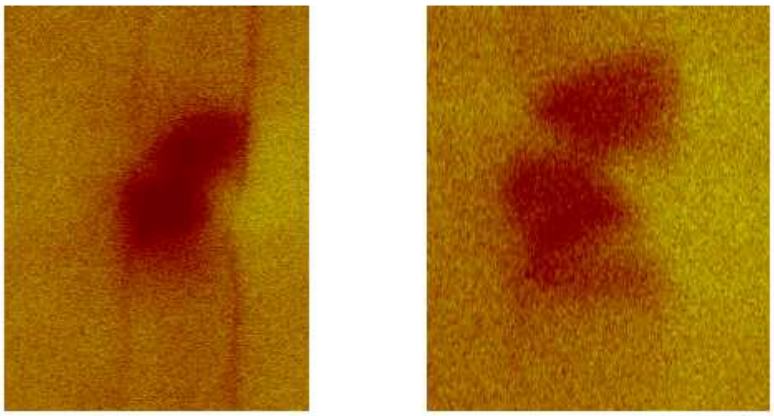

Figure 6.15: Comparison of domain wall structure obtained for (left) 100 nm and (right) 200 nm wires. The narrower structure on the left appears to promote a diagonal wall.

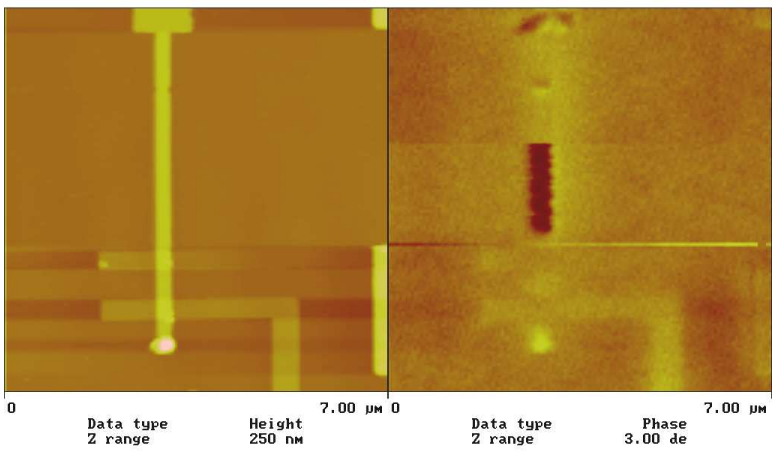

Figure 6.16: Dragging of a domain wall with MFM low moment tip.

not expected since narrower wires should result in stronger pinning. However this may be due to the fact that the constriction is not well defined due to difficulties in lithographic fabrication for narrower wires.

6.2.3 Measurement of Critical Current Densities for Magnetization Reversal

For current pulses (fast rising) above $\sim 7.5 \times 10^{11}\mathrm{A}/m^2$ and at $H_{app} \sim 0$, we observed current induced domain wall motion (CIDWM). The motivation behind using fast rising pulses, originated from Berger description [137] that sustains that this type of pulse is more effective in displacing walls. An example of this effect is shown in figure 6.16, where DW at the lower constriction has moved to upper constriction, thereby reversing the magnetization of the central segment. Reversible CIDWM, as shown in this figure, was consistently observed for all observed DW types, although the DW type was not necessarily conserved after the displacement. We can toggle between the two trapped states, i.e., alternatively displacing the DW between the two sites by reversing the polarity of electrical current pulse and maintaining the amplitude above the critical threshold. However, since these high current densities cause significant electromigration and sample deterioration as shown in figure 6.17, only few repetitions of this event (with no field) can only be observed with a given sample In conclusion, our observations on current induced magnetization reversal are in agreement with previous studies [149, 151–153, 159, 169] and we can confirm that the DW can be displaced in the direction of electron motion in absence of an external applied magnetic field (zero field measurements include the earth's magnetic field).

The critical phase space boundary H_c, j_c for domain wall motion in this type of

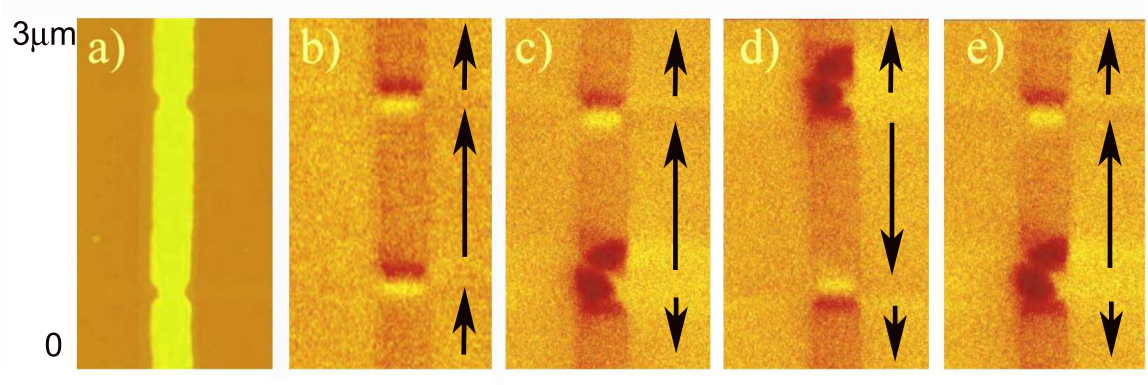

Figure 6.17: Demonstration of reversible current induced magnetization reversal of the section between the constrictions: (a) AFM zoom-in of constriction area, (b) MFM of sample at remanence after field saturation in the positive vertical direction, (c) MFM of domain wall trapped in the lower constriction after applying an external field,(d) MFM of sample after applying a current pulse (with electrons flowing upward) with magnitude above the critical value required for domain wall motion, (e) MFM of sample after applying a current pulse (with electrons flowing downward) with magnitude above the critical value required for domain wall motion.

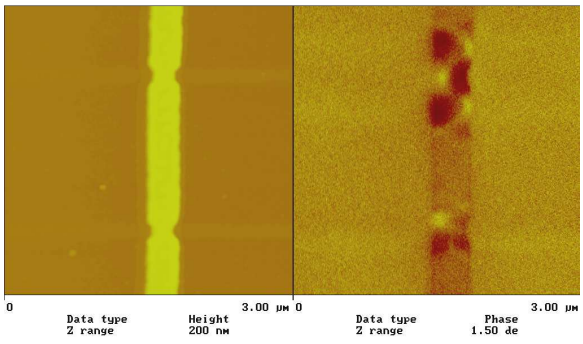

Figure 6.18: Magnetic configuration obtained after high DC currents caused significant sample deterioration.

sample was obtained using MFM. Figure 6.18, shows the data obtained using fast rising current pulses. The directions of current, field and initial magnetization in each cuadrant are specified in the diagram below. For each data point, the sample was initialized by trapping an 'A' type DW, of the same symmetry in the same constriction. For this data, all domain walls were initialized in the lower constriction. The result clearly shows a nonlinear behavior of the general form $\sim (1 - H/H_c)^{1/3}$.

An interesting observation is illustrated in figure 6.19 where we show the critical boundary for three measurements. Two of them were performed on samples with the same wall type but clear differences in the constriction geometry, while the third was performed on one a different wall type but similar constriction geometry. The result indicates that the measured critical densities are much more sensitive to domain wall type than to details concerning the constriction geometry. In the plot in figure 6.20 we compare data corresponding to DWM with both uniform and pulse current excitation. For $j_c > 0$, the direction of H_{app}, as well as the electron pressure act in the same direction and both assisting DWM. Negative currents, $j_c < 0$ correspond to the case where H_{app} and electron pressure act in opposite directions. For both types of current excitation, data confirms that the current assists in the depinning of the DW, regardless of direction of electron motion. In general, the order of magnitude of the critical current densities appears to be in agreement with other similar experiments. Results however, show significant differences between the field dependence of j_c in the uniform and pulsed excitation cases. For the pulsed case, j_c appears to be more non-linear with H_{app} in comparison to the DC case. In this data, the critical values slightly below H_p are higher for the DC case, however additional data (not shown) suggests that the

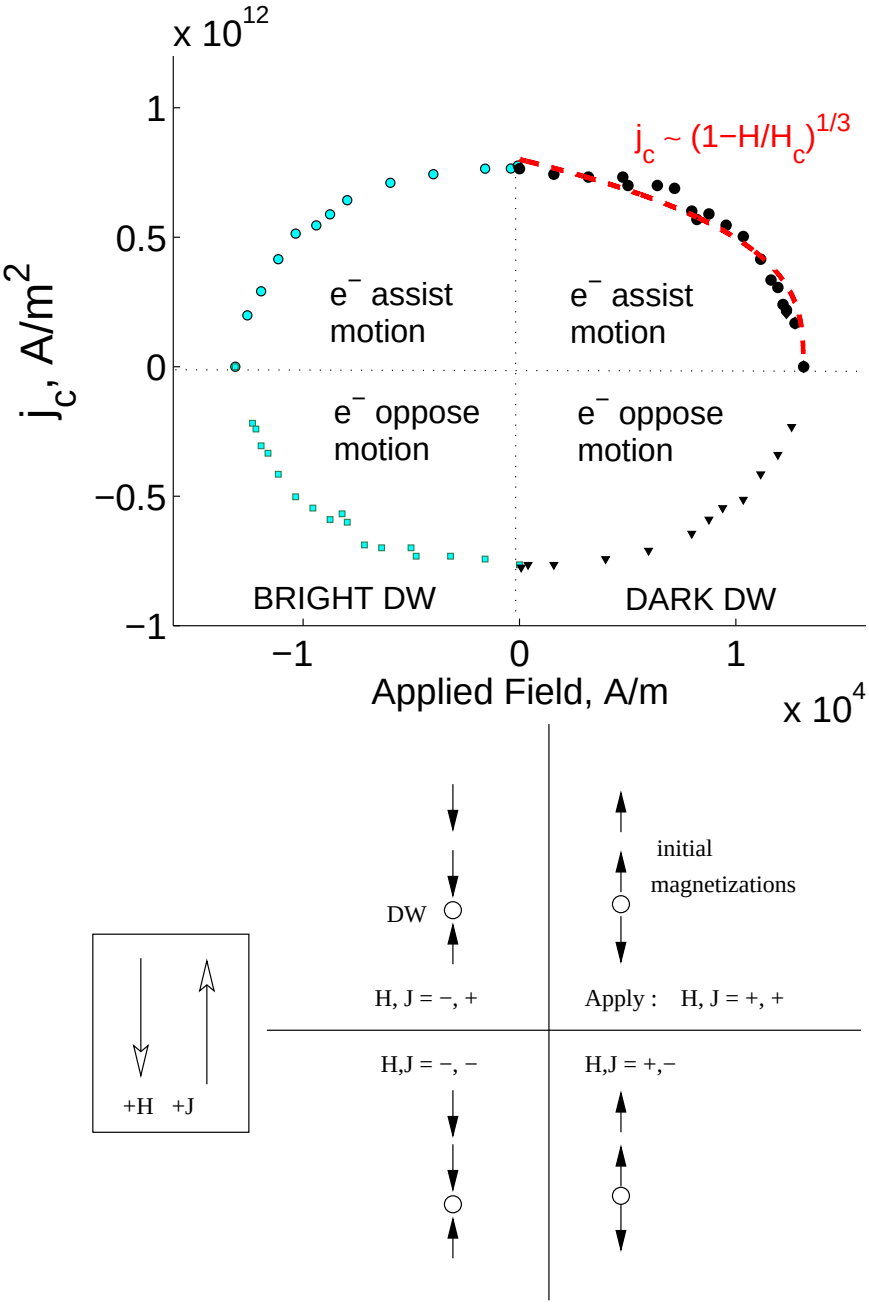

Figure 6.19: (Top) Critical current densities vs. magnitude applied magnetic field along the wire easy axis, (bottom) initial magnetization and direction of applied field and current for data taken in each cuadrant.

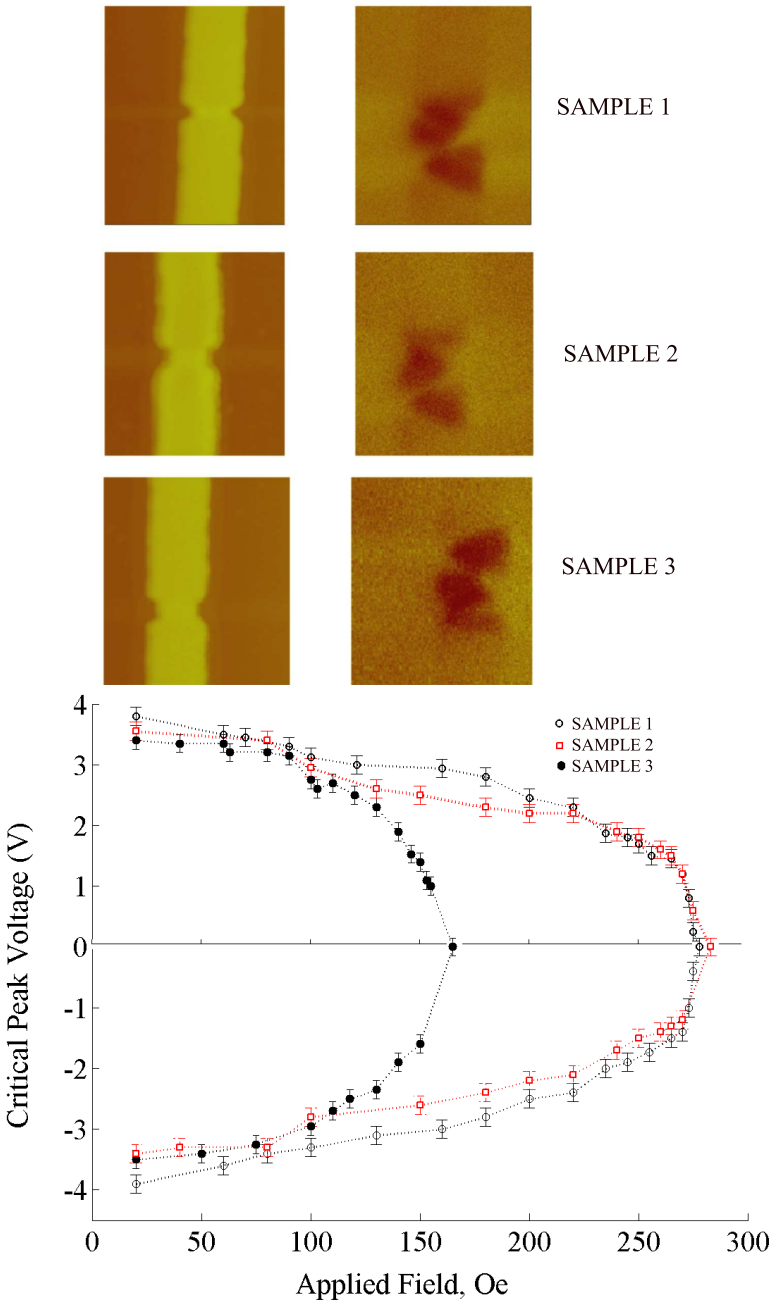

Figure 6.20: (Top) AFM/MFM images of trapped domain walls corresponding to the critical boundaries shown in the bottom part. The data shows how critical current densities depend more on wall type than on details of the constriction geometry.

magnitude of this current depends on pulse duration. For all measured samples however, critical currents for the DC case increase much faster with reducing field than those measured for the fast rising pulse case. In fact, for fields below ~ 200 Oe it was not possible to depin and displace the DW with DC current (required currents were high enough to burn the sample). More interestingly, within experimental accuracy, the data for the fast rising pulse case is nearly symmetric about horizontal axis. This is surprising, especially at high fields/low currents where joule heating is low, since one would expect that the opposing direction of the pulsed current should hinder the DWM. This suggests that the depinning mechanisms, independent of current direction, mentioned before are dominant. The DC data by contrast, shows a much stronger anti-symmetric behavior with respect to current direction at this high field range below H_p. That is, the slope of the j_c vs H_{app} line is much steeper in the lower quadrant, suggesting that the electron pressure either assists or impedes the action of the H_{app} in reversing the central domain. Thus, it appears that the DWM triggering mechanisms dominating with these two types of current dynamics are inherently different. By additionally plotting the absolute values of the critical currents for the data corresponding to electron motion opposing the direction of DWM, the asymmetry in the DC case is clearly revealed.

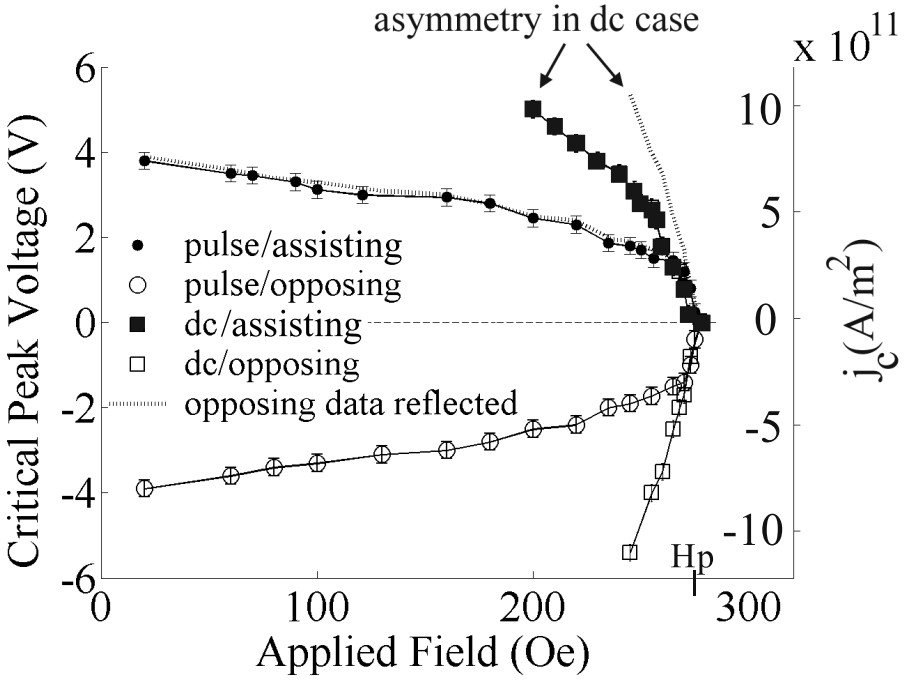

Figure 6.21: Critical current densities vs magnitude of easy axis applied magnetic field for the cases of pulsed and DC current. By reflecting the negative current data, with respect to the $j = 0$ axis, the asymmetry obtained in the DC case is clearly observed.

6.3 Theoretical Description

6.3.1 Phenomenological Description of Current Induced Domain Wall Motion

The simplest phenomenological description of this force was given by Berger [132–134]. It is based on the steady state motion of domain walls under a magnetic field for which a viscous damping force F_d balances the force from the applied field.

$$0 = F_H + F_d = 2M_s H - 2M_s \frac{v_w}{\mu} \tag{6.2}$$

In this case, μ is the intrinsic domain wall mobility. The origin of this damping force is the friction between the moving domain wall and the electron gas at rest. If however, a current j is present, the electron gas is moving with an average drift velocity of $v_e = -j/ne = jR_o$, where R_o is the ordinary Hall coefficient. If the interaction depends only on the relative motion, v_e will generate a drive source F_e of the same form as the damping force given by $F_e = 2\beta M_s \frac{v_e}{\mu}$ where β is an experimental correction factor introduced by Berger. Additionally, lattice defects apply a pinning force F_p on the wall of the general form $F_p = 2M_s H_p$ and at the critical current density for motion j_c, $F_e + F_p = 0$ and one finds $j_c = \frac{\mu H_p}{\beta |R_o|}$. If a field is applied such that it generates a force parallel to the exchange force then the critical field/current boundary H_c, j_c between static and moving walls will be determined by

$$H_c = \pm H_p - \frac{\beta}{ne\mu} j_c \tag{6.3}$$

This equation assumes the the pinning field H_p is independent of the current magnitude. In reality, we expect the current to reduce the pinning force and to obey $H_p(j) = H_p(-j)$. The most likely explanation, in Berger's own words is

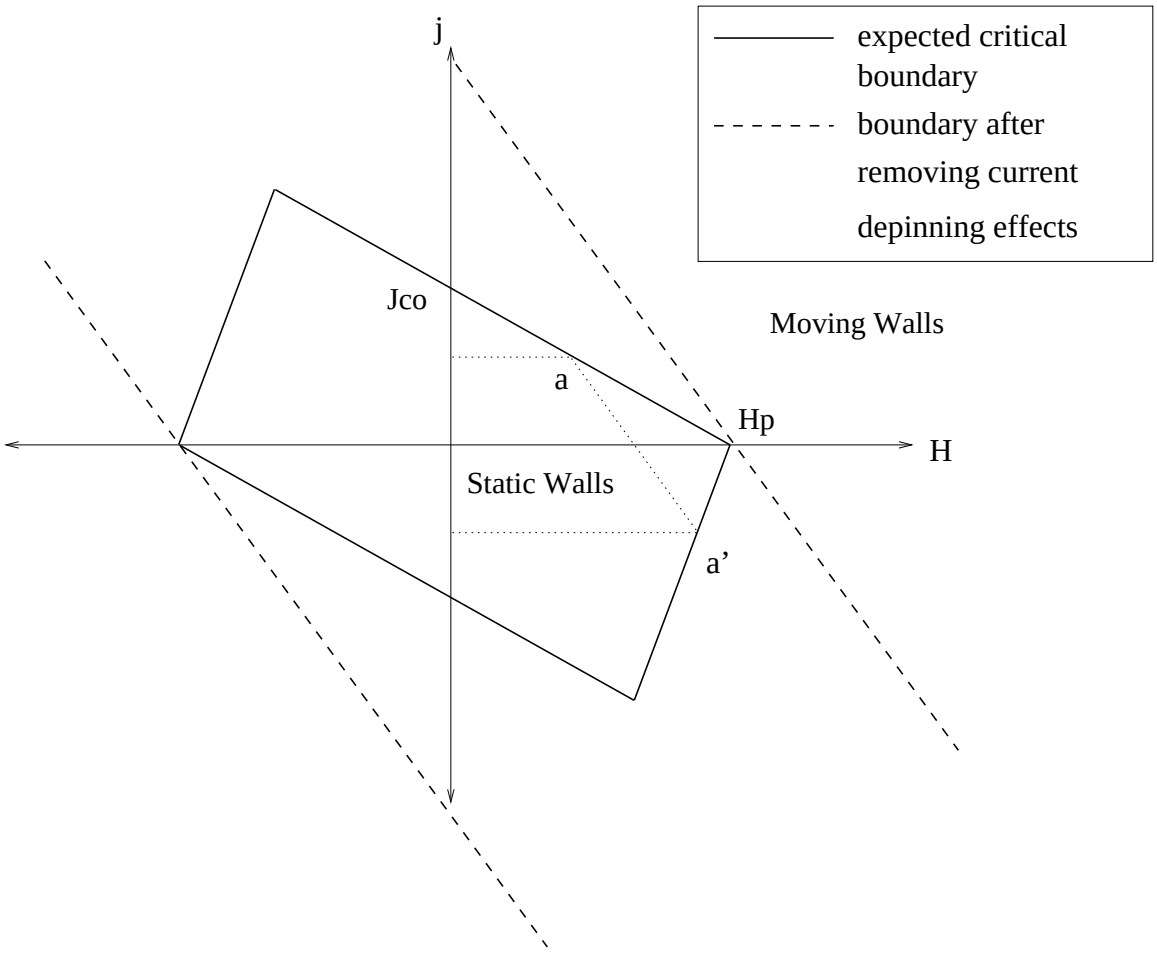

Figure 6.22: Phenomenlogical prediction for critical boundary for domain wall motion.

that the current "shakes" the wall thereby exciting modes of wall oscillation and reducing the local pinning forces. Therefore, the boundary is expected to be as shown in figure 6.21 (continuous line), with a sharp bend at H_p. The boundary (dashed line) without including the "depinning" effects from the current can be recovered from the measured boundary (continuous line) using a simple geometric construction. We simply choose two current of same magnitude but opposite polarity and find their intersections with the measured boundary at a and a'.

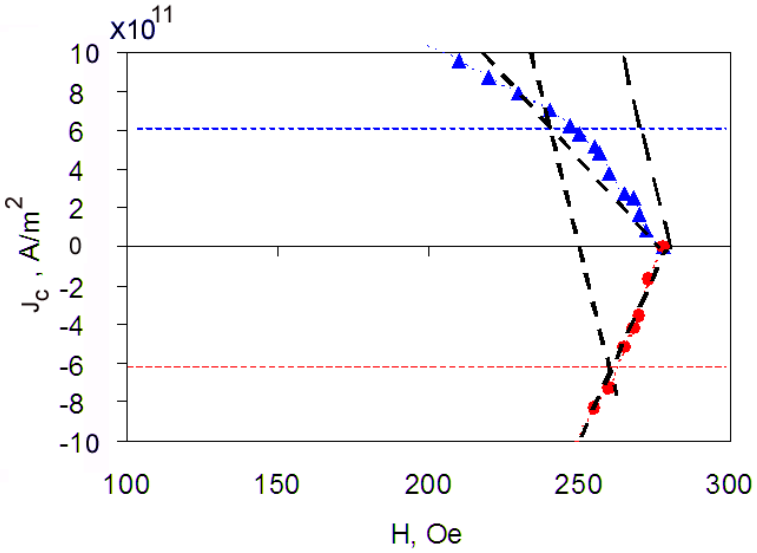

Figure 6.23: Geometrical construction for extracting domain wall mobility from the measured boundary (DC current).

The boundary without depinning effects will be parallel to a line passing through a and a' but displaced so that it pass through H_p.

With our asymmetric data obtained using DC, we perform linear fits and carry out this simple geometrical construction as shown in figure 6.22. From the slope of the curve and by using $R_o = -1.36 \times 10^{-10} m^3/C$ and $\beta = 2$, appropriate values for permalloy [110] we obtain a rough estimation of the domain wall mobility of 0.21 m^2/C for our wires, or equivalently $\sim$16 $m\ s^{-1}\ Oe^{-1}$

Figure 6.23 was originally provided by Berger, [110] and consists of a collection of almost all experimental data available for mobility of DW's as a function of the ration t/w. Note on the left upper side the mobilities measured for films, on the order of 1 m^2/C. Our measurement is marked with a large black dot. It agrees with other data obtained for nanowires, showing the expected reduction in the DW mobility for this geometry. The continuous line, represents a theoretical

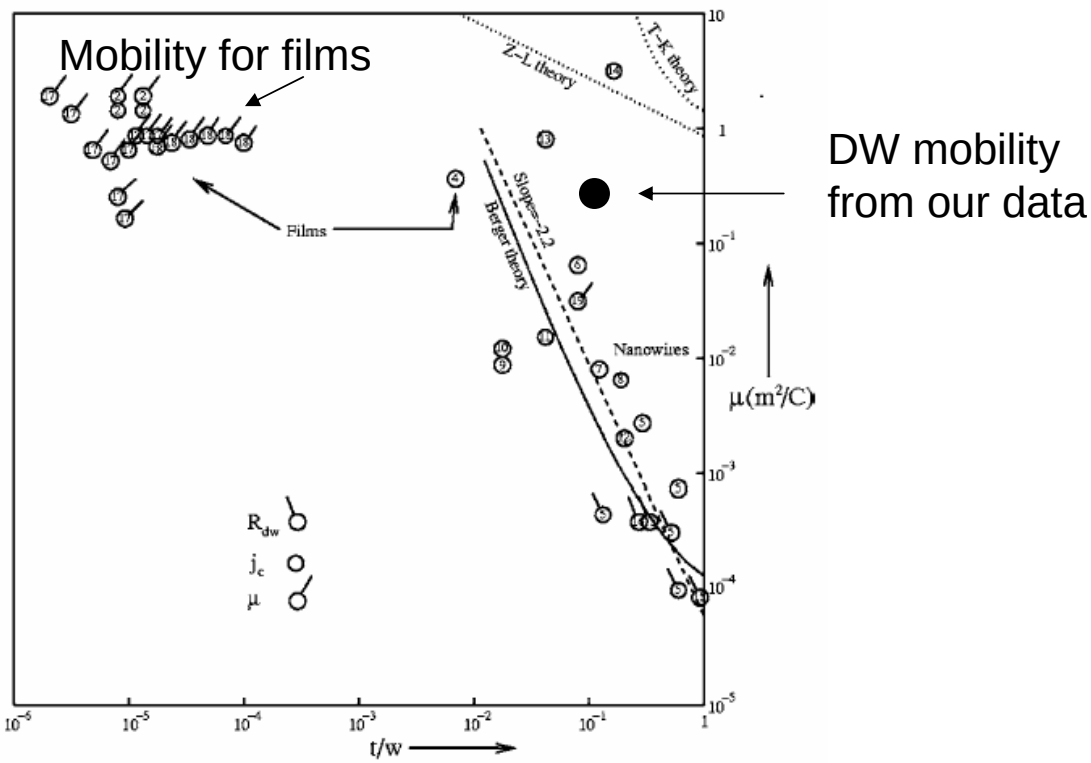

Figure 6.24: Collection of experimental data for domain wall mobility as a function of the ratio t/w, presented by Berger in [110].

formulation of this mobility for nanowires provided by Berger [110]. Although we do not explain this theory here, we note order of magnitude agreement with our data.

6.3.2 Exchange Interaction Between Domain Walls and Electric Current in thin films

In the case of a 180° degree Bloch wall, Berger estimated the strength of the potential barrier seen by the incident electron. The s-d exchange coupling occurring between the spin s of the 4s conduction electron and the more localized 3d

magnetic spin $S(x)$ of a domain wall and can be expressed as:

$$V = g\mu_B(\mathbf{s} \bullet \mathbf{H}_{sd}(x) + H_{sd/2}) \tag{6.4a}$$

$$\mathbf{H}_{sd}(x) = -2J_{sd}\langle \mathbf{S}(x)\rangle / g\mu_B \tag{6.4b}$$

Here $\mathbf{H}_{sd}$ is the interatomic exchange field, and J_{sd} the exchange integral. The value of the exchange integral is somewhat uncertain but in the range $0.05-1.5eV$ [1]. The force exerted on the magnetic moment of the conduction electron while inside the wall, can be calculated from the gradient of the exchange field

$$F_x = -g\mu_B \mathbf{s} \bullet (d\mathbf{H}_{sd}/dx) \tag{6.5}$$

We consider local y and z axes parallel to the plane of the wall and a z-axis parallel to the exchange field, making an angle $\theta(x)$ with the $\mathbf{H}_{sd}(+\infty)$. This is depicted in figure 5.5.

$$F_x = -g\mu_B H_{sd} s_y d\theta/dx \tag{6.6}$$

and the precession of $\mathbf{s}$ around $\mathbf{H}_{sd}(x)$ is given by

$$\hbar d\mathbf{s}/dt = -g\mu_B \mathbf{s} \times \mathbf{H}_{sd} \tag{6.7}$$

The adiabatic approximation, which implies $(-\mathbf{s}, \mathbf{H}_{sd}) << \theta(x)$ and therefore $\frac{dS_y}{dt} \simeq S_z \frac{d\theta}{dt}$ allowing us to write

$$s_y \cong \frac{1/2\hbar^2}{(g\mu_B H_{sd})^2}[(d^2\theta/dx^2)v_x^2 + (d\theta/dx)dv_x/dt] \tag{6.8}$$

For sufficiently thick walls, the second term is negligible and by combining these equations we can write

$$F_x = -\frac{1/2\hbar^2 v_x^2}{2g\mu_B H_{sd}} \frac{d}{dx}(\frac{d\theta}{dx})^2 \tag{6.9a}$$

$$V = \frac{1/2\hbar^2}{2g\mu_B H_{sd}}(\frac{d\theta}{dx})^2 v_x^2 \cong 10^{-3} - 10^{-2} eV \tag{6.9b}$$

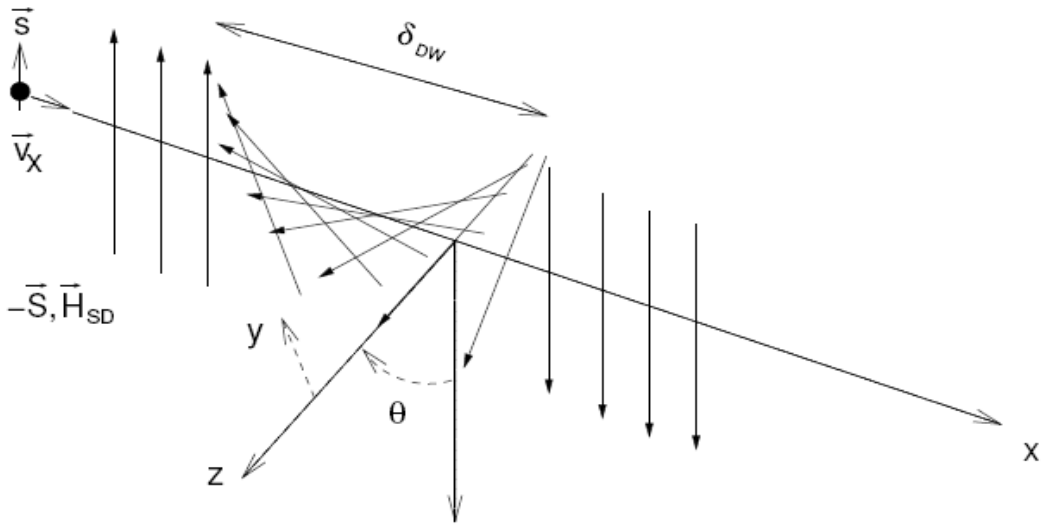

Figure 6.25: Definition of variables for estimation of potential seen by a conduction electron when crossing the localized 3d spin distribution inside a domain wall.

From this model we point out that the angular variation of the force is an odd function with respect to the center of the wall (x=0), so that $d(d\theta/dx)^2/dx$ has opposite sign on each side of the wall. Thus integration of the total force on the wall vanishes when the electron density is assumed constant or in the case of zero current flow. However, when a current flows, the densities of conduction states between the sides of the wall are not the same since there is a potential drop across the wall. Hence, a non-zero force exists on the wall in the direction of electron flow. The salient conclusion from this analysis is that a force perpendicular to the wall exists when a polarized current transverses a domain wall. The force is directed opposite to the direction of current flow.

In [129], Berger uses this value for the domain wall interaction potential in order to estimate the intrinsic mobility μ. The calculation is based on classical transport equations, which are justified for wall thickness well above the electron wavelength. The result is

$$\mu = \frac{16\pi^2\hbar^3 M_s}{m^{*2}(\overline{\Delta V})^2}\frac{\delta}{\Lambda} \tag{6.10}$$

A fairly rough estimation can be made by considering $M_s \sim 1T$, $\overline{\Delta V} \sim 2 \times 10^{-2}eV$, $\delta \cong 40nm$ and an interband mean free path $\Lambda \sim 40$ nm. This potential is averaged over the wall thickness. The effective mass on the other hand is assumed to be three times the free electron mass, because of s-d electron-magnon admixtures. The final result gives $\mu \cong 2m^2/C$, agreeing with experimental values that have found $\mu \cong 1m^2/C$ (or $\sim 80\ m\ s^{-1}\ Oe^{-1}$) [144] in thick permalloy.

6.3.3 Review of Field Driven Domain Wall Motion

Micromagnetic modeling of the motion of a domain wall in a uniform DC magnetic field is a complex problem. During the 1970's however, N. L. Schryer and

L. R. Walker presented an analytical solution for this problem in the case of the 180° degree Bloch wall forming in uniaxial materials, when a uniform magnetic field applied along the symmetry axis. In this case, the problem is greatly simplified since there are only two independent variables, namely time and the coordinate normal to the wall. Their analysis originates from the phenomenological equation of motion used to describe the damped gyromagnetic precession of a magnetization vector. The equation was originally proposed by Landau and Lifshitz in 1935 and later modified by Gilbert in order to correct the behavior in the limit high damping. For this reason it is commonly known referred to as the Landau-Lifshitz-Gilbert (LLG) equation.

$$\frac{\partial \mathbf{M}}{\partial t} = -\gamma \mathbf{M} \times \mathbf{H}_{eff} + \frac{\alpha}{M_s} \mathbf{M} \times \frac{\partial \mathbf{M}}{\partial t} \tag{6.11}$$

where α is the damping term (Gilbert loss parameter) and γ the gyromagnetic ratio. The first term describes the Larmor precession of the magnetic moment around the local magnetic field and the second, the damping of this precession that allows relaxation to equilibrium. Some of the processes which contribute to the damping in a magnetic film are magnon-magnon and magnon-phonon interactions and interactions between localized and itinerant electrons and eddy currents.

These equations can also be expressed in terms of the free energy density by noting that the torque acting on the magnetization is related to the free energy E by the equations $\mathbf{F} = -\nabla E$, and $\mathbf{T} = \mathbf{r} \times \mathbf{F} = -\mathbf{r} \times \nabla E$, where F is the generalized force and r is a radius vector in the direction of M.

$$M = \hat{\mathbf{r}} M_s \tag{6.12a}$$

$$\mathbf{T} = \hat{\phi} \frac{\partial E}{\partial \theta} - \hat{\theta} \frac{1}{sin\theta} \frac{\partial E}{\partial \phi} \tag{6.12b}$$

The one dimensional LLG equation expressed in terms of the polar and azimuthal angles θ and ϕ becomes

$$\frac{M}{\gamma}(\alpha\dot{\theta} - \dot{\phi}sin\theta) = \frac{\delta\varepsilon}{\delta\theta} \tag{6.13a}$$

$$\frac{M}{\gamma}(\dot{\theta} + \alpha\dot{\phi}sin(\theta)) = (\frac{1}{sin(\theta)})\frac{\delta\varepsilon}{\delta\phi} \tag{6.13b}$$

where $\varepsilon(M)$ is the local energy density.

Schryer and Walker considered an infinite medium whose magnetization is only a function of x and also conserves its magnitude $|M| = M_s$. For this system, the energy consists of Zeeman, magnetostatic, anisotropic and exchange .

$$\varepsilon = -H_o M_z + 2\pi M_x^2 - K\frac{M_z^2}{M_s^2} + \frac{A}{M_s^2}|\frac{\partial \mathbf{M}}{\partial x}|^2 \tag{6.14}$$

By substituting this energy density we obtain the following equations of motion for this problem

$$\dot{\theta} - \alpha\dot{\phi}sin\theta = 4\pi\gamma M_o sin\theta sin\varphi cos\varphi + \frac{2\gamma A}{M_o}\frac{1}{sin\theta}\frac{\partial}{\partial x}(sin^2\theta\frac{\partial\varphi}{\partial x}) \tag{6.15}$$

$$\begin{aligned}\alpha\dot{\theta} + \dot{\phi}sin\theta = 4\pi\gamma M_o sin\theta cos\theta cos^2\varphi + \frac{2k\gamma}{M_o}sin\theta cos\theta + \gamma H_o sin\theta + \\ \frac{2\gamma A}{M_o}sin\theta cos\theta(\frac{\partial\varphi}{\partial x})^2 - \frac{2\gamma A}{M_o}\frac{\partial^2\theta}{\partial x^2}\end{aligned} \tag{6.16}$$

These equations of motion are difficult to solve, however they proposed a simple trial solution that proved to be an adequate solution for applied fields lower than a given critical field $H_c = 2\pi\alpha M_s$. In their solution, the domain wall moves at constant velocity without changing its shape. During the motion, the angle φ is assumed to be independent of position and the instantaneous width of the domain wall, determined by $c(t)^{-1}$, is the only variable parameter during the

motion. These characteristics can be expressed as

$$\varphi = \varphi(t) \tag{6.17a}$$

$$\ln[\tan(\theta/2)] = c(t)[x - d(t)] \tag{6.17b}$$

With these trial functions it is possible to calculate the domain wall width and velocity as a function of time for any applied field $H_o(t)$.

$$v(t) = \frac{\alpha\gamma H_o + 4\pi\gamma M_o sin\varphi(t) cos\varphi(t)}{(1+\alpha^2(t))c(t)} \tag{6.18a}$$

$$c(t)^2 = 1 + (2\pi M_o^2/k) cos^2\phi(t) \tag{6.18b}$$

6.3.4 Domain Wall Dynamics Driven by Adiabatic Spin-Transfer

One approach to understanding domain wall dynamics under spin-transfer torque is to incorporate a spin-torque term into the Landau-Liftshitz equation. This problem was considered by Li and Zhang [157] who reported the most complete and detailed calculation of the spin-torque term [145, 145].

The basis for this model is, once again, the s-d Hamiltonian:

$$H_{sd} = -J_{sd}\mathbf{s}\cdot\mathbf{S} = \frac{SJ_{sd}}{M_s}\mathbf{s}\cdot\mathbf{M}(r,t) \tag{6.19}$$

where $\mathbf{S}$ has been replaced by the classical magnetization $\mathbf{S}/S = -\mathbf{M}(\mathbf{r},t)/M_s$ and $\mathbf{s}, \mathbf{S}$ are the spins of the itinerant and localized electrons. The calculation involves deriving the linear response function for the conduction electron spin in a time and spatially varying local moment.

It is assumed that the non-equilibrium electrons are generated by a DC electric field or a time-dependent magnetic field. While the first directly generates the

charge and spin currents, the second drives the magnetization changes that induce non-equilibrium spin density (through the s-d interaction). The spin operator however, must satisfy the continuity equation

$$\frac{\partial \mathbf{s}}{\partial t} + \nabla \cdot J = \frac{1}{i\hbar}[\mathbf{s}, H_{sd}] - \Gamma(\mathbf{s}) \tag{6.20}$$

where J is the spin current and $\Gamma(\mathbf{s})$ the spin relaxation time due to scattering with impurities, electrons etc. By averaging over all occupied electronic states one obtains the semiclassical Bloch equation for the conduction electron spin density $\mathbf{m}$.

$$\frac{\partial \mathbf{m}}{\partial t} + \nabla \cdot J_{av} = -\frac{1}{\tau_{ex} M_s} m \times \mathbf{M}(\mathbf{r}, t) - \Gamma_{av}(\mathbf{s}) \tag{6.21}$$

with $\mathbf{m}(\mathbf{r}, t) =< \mathbf{s} >$, $J_{av} =< J >$, $\Gamma_{av}(\mathbf{s}) =< \Gamma(\mathbf{s}) >$ and $\tau_{ex} = \hbar / S J_{sd}$.

The induced spin density $\mathbf{m}$ is separated into two terms. The first represents the adiabatic spin density when the conduction electron spin relaxes to the equilibrium value at a time t. Since the dynamics of the magnetization is slow compared to that of the conduction electrons, it is reasonable to assume that the spin of the conduction electrons follows the direction of the local moment. The second term contains all non-adiabatic contributions.

$$\mathbf{m}(\mathbf{r}, t) = \mathbf{m}(\mathbf{ro}, t) + \delta\mathbf{m}(\mathbf{r}, t) = n_0 \frac{\mathbf{M}(\mathbf{r}, t)}{M_s} + \delta\mathbf{m}(\mathbf{r}, t) \tag{6.22}$$

where n_0 represents the equilibrium local spin density (parallel to the local magnetization). Similarly, the spin current is written as

$$J_{av}(\mathbf{r}, t) = J_{av}(\mathbf{r}, t) + \delta J_{av}(\mathbf{r}, t) = -(\mu_B P / e)\mathbf{j}_e \otimes \frac{\mathbf{M}(\mathbf{r}, t)}{M_s} + \delta J_{av}(\mathbf{r}, t) \tag{6.23}$$

where j_e is the current density and P the spin polarization of the ferromagnet. The first term in this equation is the spin current component with spin polarization parallel to the local magnetization (note that it is a tensor composed of the charge current and the spin polarization of the current).

Next, Zhang and Li introduce several simplifications that allow them to obtain a closed solution for the non-equilibrium spin density. First, the relaxation term is modeled in terms of a spin-flip relaxation time τ_{sf} as $\Gamma_{av} = \delta\mathbf{m}(\mathbf{r}, t)/\tau_{sf}$ Second, only a linear response of $\delta\mathbf{m}$ to the electric current is considered. Within semiclassical transport, the non-adiabatic current density and the nonequilibrium spin density are related through the spin diffusion constant D_0 by $\delta J = -D_0\nabla\delta\mathbf{m}$

By inserting equations 5.25 and 5.26 into the continuity equation one obtains

$$D_0\nabla^2\delta\mathbf{m} - \frac{1}{\tau_{ex}M_s}\delta\mathbf{m}\times\mathbf{M} - \frac{\delta\mathbf{m}}{\tau_{sf}} = \frac{n_0}{M_s}\frac{\partial\mathbf{M}}{\partial t} - \frac{\mu_B P}{eM_s}(\mathbf{j}_e\cdot\nabla)\mathbf{M} \tag{6.24}$$

And from this equation one can identify that the non-equilibrium spin density is created by two terms: one is time varying and the other spatial variation of the magnetization. By neglecting the second order spatial derivative $D_0\nabla^2\delta\mathbf{m}$ since we assume magnetization varies slowly in space, the equation becomes a simple algebraic equation and through basic vector manipulations one can obtain

$$\delta\mathbf{m} = \frac{\tau_{ex}}{1+\xi\xi^2}\left[-\frac{\xi n_0}{M_s}\frac{\partial\mathbf{M}}{\partial t} - \frac{n_0}{M_s^2}\mathbf{M}\times\frac{\partial\mathbf{M}}{\partial t} + \frac{\mu_B P\xi}{eM_s}(\mathbf{j}_e\cdot\nabla)\mathbf{M} + \frac{\mu_B P\xi}{eM_s^2}\mathbf{M}\times(\mathbf{j}_e\cdot\nabla)\mathbf{M}\right] \tag{6.25}$$

where $\xi = \tau_{ex}/\tau_{sf}$.

The above spin density is responsible for exerting a spin-torque on the magnetization. This torque is given by $\mathbf{T} = -(SJ_{sd}/\hbar M_s)\mathbf{M}\times\mathbf{m} = -(1/\tau_{ex}M_s)\mathbf{M}\times\delta\mathbf{m}$ and by inserting the non-equilibrium spin density we obtain:

$$T = \frac{1}{1+\xi^2}[-\frac{n_0}{M_s}\frac{\partial\mathbf{M}}{\partial t} + \frac{\xi n_0}{M_s^2}\mathbf{M}\times\frac{\partial\ \mathbf{M}}{\partial t} - \frac{\mu_B P}{eM_s^3}\mathbf{M}\times[\mathbf{M}\times(\mathbf{j}_e\cdot\nabla)\mathbf{M}] - \frac{\mu_B P\xi}{eM_s^2}\mathbf{M}\times(\mathbf{j}_e\cdot\nabla)\mathbf{M}] \tag{6.26}$$

Here we identify four terms: the first two (independent of current) arise from magnetization variation in time and the second two from variations in space. The latter are the current driven torque components.

By adding these terms to the LLG equation we obtain the full equation for magnetization dynamics in terms of spin currents.

$$\frac{\partial \mathbf{M}}{\partial t} = -\gamma \mathbf{M} \times \mathbf{H}_{eff} + \frac{\alpha}{M_s} \mathbf{M} \times \frac{\partial \mathbf{M}}{\partial t} + \mathbf{T} \tag{6.27}$$

By inspecting 5.29, we find that the first term is of the form of the first term while the second is of the form of the damping term. These two terms can be introduced into the original LLG equation by renormalizing the constants α and γ

$$\gamma' = \gamma(1+\eta)^{-1} \tag{6.28a}$$

$$\gamma'\alpha' = \gamma(\alpha + \xi\eta) \tag{6.28b}$$

with $\eta = (n_0/M_s)/(1+\xi^2)$. For a typical ferromagnet with $J_{sd} \sim 1eV$, S=2, $\tau_{sf} \sim 10^{-23}s$, $n_0/M_s \sim 10^{-2}$ and $\xi \sim 10^{-2}$, $\xi\eta \sim 10^{-4}$ and therefore negligible in comparison to other damping mechanisms.

After absorbing the temporal spin-torques into the original terms in the LLG equation, Zhang and Li, write the final equation as

$$\frac{\partial \mathbf{M}}{\partial t} = -\gamma \mathbf{M} \times \mathbf{H}_{eff} + \frac{\alpha}{M_s} \mathbf{M} \times \frac{\partial \mathbf{M}}{\partial t} - \frac{b_j}{M_s^2} \mathbf{M} \times \left(\mathbf{M} \times \frac{\partial \mathbf{M}}{\partial x} \right) - \frac{c_j}{M_s} \mathbf{M} \times \frac{\partial \mathbf{M}}{\partial x} \tag{6.29}$$

where it is assumed that the current is in the x direction, $b_j = Pj_e\mu_B/eM_s(1+\xi^2)$ and $c_j = Pj_{e\mu_B\xi/eM_s}(1+\xi^2)$ both constants with units of velocity. We point out that the term accompanied by the constant b_j (describing the adiabatic spin-torque) has been derived by Bazaily [146] et al. and Tatara and Kohno [147] . The c_j term on the other hand, has only been found through this calculation. Although it is much smaller than the b_j term, since $c_j/b_j \sim 10^{-2}$, it is important in determining the domain wall dynamics. In fact, Zhang shows that the terminal velocity of the domain wall is independent of b_j and controlled by the c_j term. Therefore experimental analysis must include this term.

Following Walkers trial solution approach, the initial and terminal velocity of the domain wall can be estimated. To do so we consider a Neél wall in a nanowire whose magnetization only depends on the position along the wire, i.e. $\mathbf{M}(x,t)$. The effective field due to anisotropy, exchange and demagnetization is given by

$$H_{eff} = \frac{H_k M_x}{M_s}\mathbf{e}_x + \frac{2A}{M_s^2}\nabla^2\mathbf{M} - 4\pi M_z \mathbf{e}_z + H_{ext}\mathbf{e}_x \tag{6.30}$$

by inserting equation 5.33 into the complete LLG equation and assuming the same trial solution used by Walker and Schryer with the magnetization given by $M(\theta,\varphi)$, where $M_x = M_s cos\theta$,$M_y = M_s sin\theta cos\varphi$,$M_z = M_s sin\theta sin\varphi$ and the angles determined by

$$\varphi = \varphi(t) \tag{6.31a}$$

$$\ln\tan\frac{\theta}{2} = W^{-1}(t)(x - \int_0^t v(\tau)d\tau) \tag{6.31b}$$

one finds two coupled differential equations for the parameters φ and $W(t)$. The solution yields expressions for the initial and terminal velocities of the wall as

$$v(0) = -\frac{1}{1+\alpha^2}[\alpha\gamma H_{ext}W(0) + b_j + \alpha c_j] \tag{6.32a}$$

$$v_{\infty)} = \frac{1}{\alpha}[\gamma H_{ext}W(\infty) + c_j] \tag{6.32b}$$

where W is a parameter related to the width of the wall.

In [148], the LLG equation including the adiabatic and non-adiabatic spin-torques are solved for the case a head-to head Neél wall formining in a submicron Py wire, under the effect of a pinning field. The result is included in figure 6.22. In addition to predicting the expected magnitude for the critical current density, the result shows that the linearity or nonlinearity of the critical boundary depends on the relative weight of the adiabatic and non-adiabatic torque terms determined by ξ.

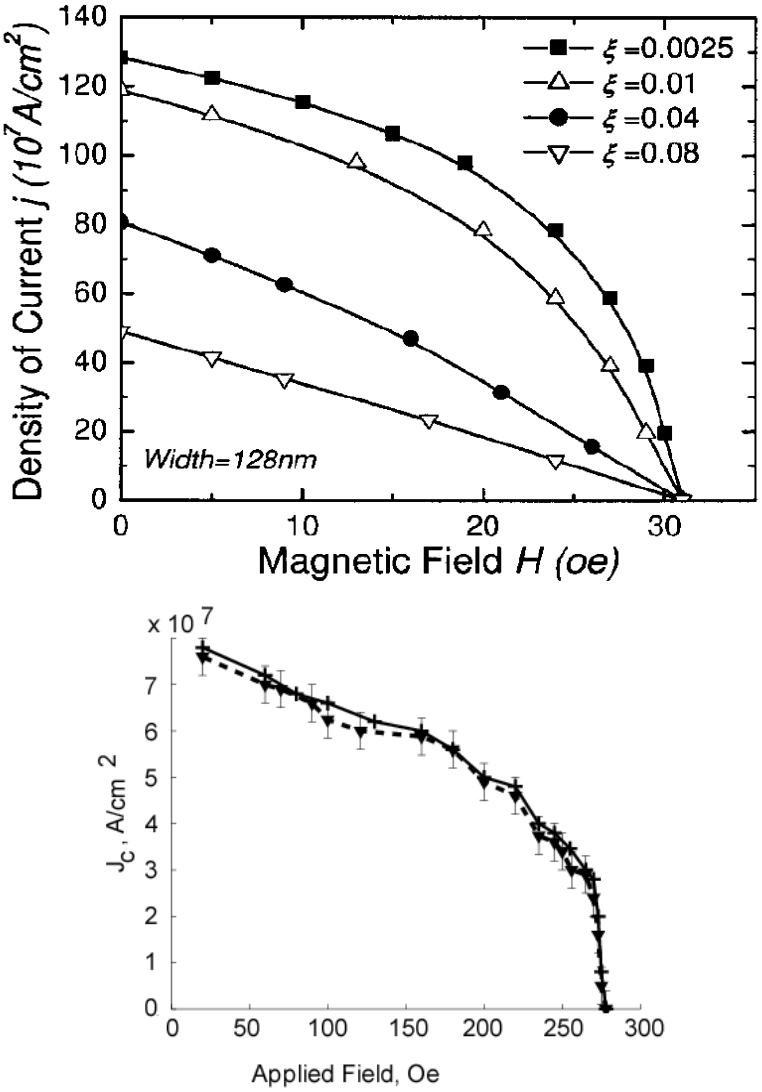

Figure 6.26: (Top) Critical boundary for domain wall motion for different ratios of ξ from simulation carried presented by He et al. Reprinted with permission from J. Appl. Phys. 98, 016108 (2005), Copyright 2005, American Institute of Physics. (Bottom) our experimental data for this boundary for permalloy with $\xi \sim 10^{-2}$.

For materials used in our experiments we have $\xi = \tau_{ex}/\tau_{sf} \sim 10^{-2}$. By comparing this result with our data we observe that although there is a clear similarity in the shape of the curves, our experimental data is about an order of magnitude lower than the values obtained in the simulation. The difference in order of magnitude is probably due the heating effects not considered in the simulation. These effect will assist the switching process. The qualitative behavior of the experimental data does however suggest the dominance of the adiabatic term in our experiments.

6.4 Summary of Results

- We observed current induced domain wall transformations (between different domain wall types) when applying current pulses near $5 \times 10^{11} A/m^2$ through the wires.

- We demonstrated the effect of current induced domain wall motion in nanoscale patterned permalloy wires with current densities on the order of $7 \times 10^{11} A/m^2$. The direction of electron motion coincides with the direction of electron flow.

- By including two constrictions along the wire we observed *reversible* current-induced magnetization reversal, of the section of the wire between the constrictions.

- We measured the critical phase space boundary (H_c, j_c) between static and moving walls, for the cases of DC and fast rising pulses.

- For experiments carried out in the presence of external fields, we confirmed that the current assists in the depinning of the domain wall *regardless* of its *polarity* and the motion is always in the direction of the applied field.

- Only in the case of DC current were we able to detect the asymmetry induced by the current direction.

- From the DC data we extract and estimation of the domain wall mobility of $\sim 0.2\ m^2/C$in our patterned wires.

Chapter 7

Current Induced Switching in a Nanoscale Spin-Valve Device

7.1 Introduction

In the previous section we demonstrated the possibility of switching the magnetization of a section of a nanowire by using only current. This system constitutes a current-controlled bi-stable device and is very attractive for applications such as MRAM. However, in order to obtain a useful device, readout of the magnetic state must be attainable through an efficient process. Until now, we have determined the magnetic state through magnetic imaging, a process clearly not viable for device applications.

In an early attempt to electrically determine the magnetic state of our devices, we performed magnetoresistance measurements on our Py nanowires containing two constrictions. The presence of the domain wall in the wire results in a tiny dip in the curve due to AMR from the DW. This effect was only detectable through AC four-wire resistance measurements and an example of this measurement together with an SEM micrograph of the four-contact set-up are shown in figure

6.1. These measurements are taken with the magnetic field applied parallel to the wire and the magnitude of the effect is below 0.02%.

In order to amplify the magnetoresistive response, one possibility is to take advantage of the spin-valve effect. The idea of current induced switching in a spin-valve devices, is not new and has been widely studied. However, most studies carried out to date consider the current perpendicular to plane (CPP) configuration previously described. In this case the current is injected perpendicular to the free layer through a point contact. The spin-torque, depending on the current direction, can have a substantial component that either opposes or enhances the magnetic damping. This leads to a state of persistent magnetization precession driven by the DC current. Excitation and full magnetization reversal have been predicted and observed in numerous theories and experiments [190–195]. In this work, we consider the current parallel to plane configuration (CIP), for which the effects of current induced magnetization reversal are largely unexplored. In fact, to our knowledge, the only work of this type was carried out by Grollier et al. [171]. In their initial work, current induced depinning of a domain wall in this device was shown however, a consistent correlation between electron direction and domain wall motion direction is not observed. In an additional subsequent report [172], the authors observe the effects, on the MR, of displacing a domain wall between two naturally occurring defects. In this experiment we provide, for the first time demonstration of full magnetization reversal between two artificially produced domain wall traps. For this purpose we fabricated spin-valves in the same pattern studied in chapter 6, i.e., nanowires containing two constrictions and a nucleation pad at one extreme. This structure allowed us to observe the current induced switching effect through reproducible and consistent events.

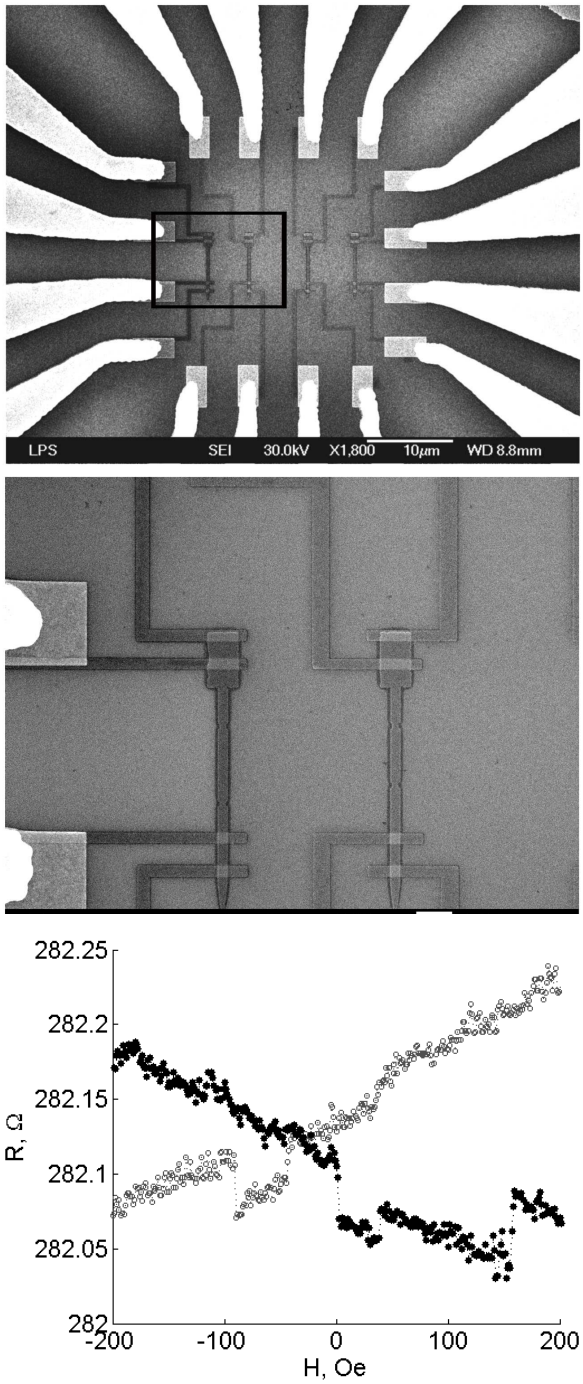

Figure 7.1: (Top) Permalloy pattern with electrical contacts for four-wire resistance measurements. (Bottom) Four-wire longitudinal magnetoresistance measurement for the sample above, showing a tiny dip from the AMR of a trapped domain wall.

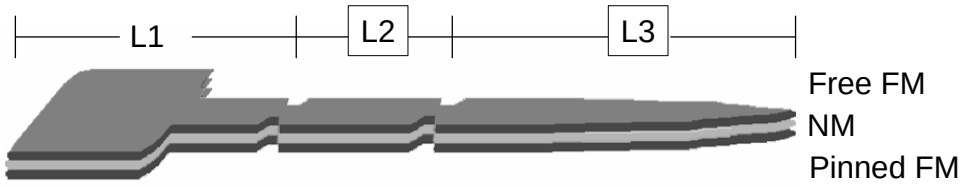

Figure 7.2: Schematic of the sample geometry for the nanoscale exchange-biased spin-valves.

7.2 Experiment

The sample stack is typically formed by IrMn(10 nm)/FM(10 nm)/Cu (3 nm)/ FM (20 nm) where FM is either Py or Co. The fabrication process is once again the simple lift-off process described in the appendix and all materials were deposited in a thermal evaporator at pressures near 1×10^{-6} torr. Figure 6.2 shows a schematic of the sample geometry.

Two sets of wires different lengths were fabricated. The first set was 20 μm long with distances between the constrictions of 4.2, 6, 6.6 or 8 μm. The second set was 10 μm long and with distances of 1.7, 2.2 and 3.2 μm. Figure 6.3 includes AFM/MFM images of the first set of Py based spin-valves. The MFM images are taken at remanence after saturation, revealing bright/dark contrast at the constrictions.

7.2.1 Magnetoresistance Measurements

Typical magnetoresistance curves obtained for this type of sample when sweeping the field longitudinally from negative to positive values are shown in figure 7.4. The step-like behavior appears due to the fact that sections of the free layer of the pattern switch independently as depicted in the inset arrows next to each resistance level. For example, in the top curve, the measurement begins at -150 Oe with all layers magnetization's in the direction of the applied field (left). This configuration persists up to zero applied field due to the presence of the exchange-biasing field. The coupling between the layers maintains this configuration. At a low positive field, however, a section of the free layer switches leading to a significant increase in resistance due to the spin-valve effect. At this field, we expect a domain wall to be trapped in the leftmost constriction. At a somewhat higher field, the domain wall moves to the constriction to the right leading once again to a jump in the resistance. At +50 Oe, there is another jump and the free layer is completely antiparallel to the pinned layer. For a higher field above 100 Oe, the pinned layer also reverses its direction, thereby inducing a drop in the resistance(both layers are parallel once again). For the curve presented, the magnitude of the effect is near 0.6%. From all samples measured, responses up

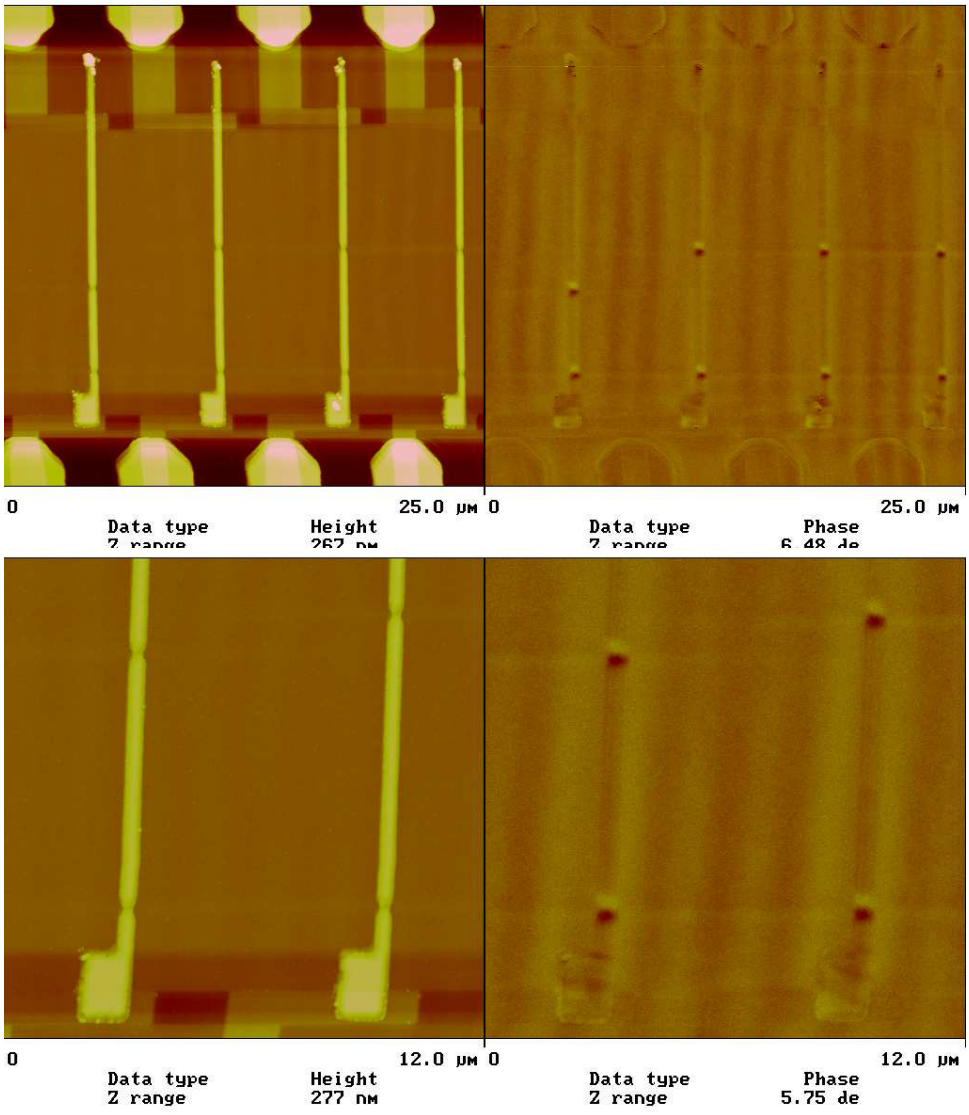

Figure 7.3: AFM/MFM images of IrMn/Py/Cu/Py spin-valve structures.

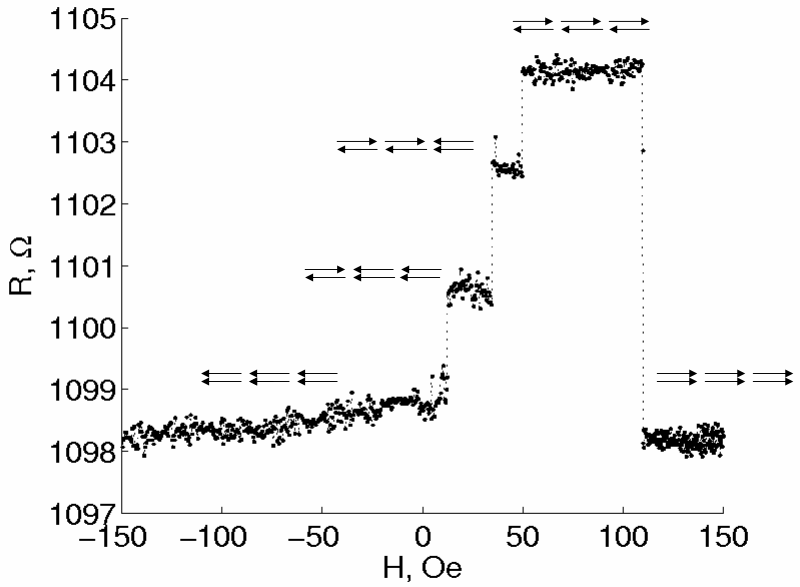

Figure 7.4: Step-like magnetoresistance (with field swept from negative to positive values) revealing domain wall trapping in the free layer.

to 1.5% were observed. In this case, the sample was 10 μm with L1=2.5 μm, L2= 3.2 μm, L3=4.3 μm, the width of the wire near 0.4μm while the width of the nucleation pad 1.5μm. The resulting areas of the three sections separated by the constrictions area roughly one third each, corresponding to the distribution of levels in the MR. In figure 7.5, we observe that domain wall trapping may also occur in the pinned layer as described by the arrows near the curve. The occurrence of this effect essentially depends on the width of the constriction. The relative magnitude of the exchange-biasing switching field and the pinning field of the constrictions determines whether the event is observed or not for a given sample. This is more likely for narrower constrictions with stronger trapping potential/higher pinning fields. For samples with strong exchange biasing, the

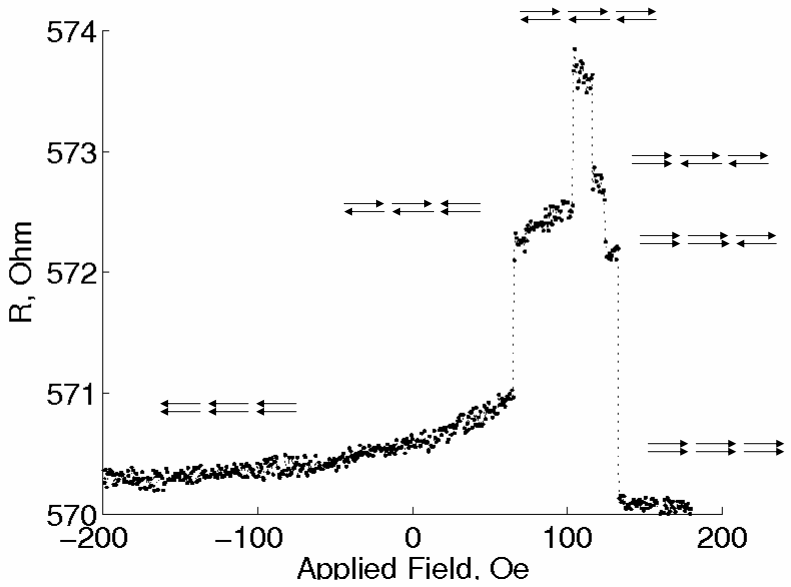

Figure 7.5: Step-like magnetoresistance (with field swept from negative to positive values) revealing domain wall trapping in the pinned layer.

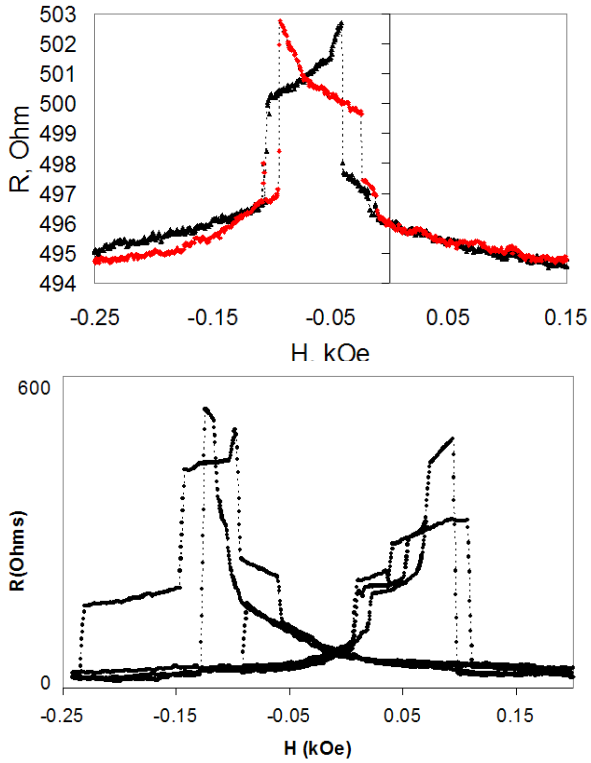

Figure 7.6: Complete MR cycle showing effect of (top) strong and weak (bottom) exchange biasing. The latter, behaving more like a *pseudo* spin-valve, exhibits strong hysteresis.

complete MR loop is overlapping as shown in figure 7.6 (top). This is not always the case and some samples exhibit strong hysteresis as shown in the bottom part of the same figure. In the latter case, the behavior seems more like that of a *pseudo* spin-valve, that is, two layer of different coercivities. The presence of the AF underlayer and the difference in thickness (between the two FM layers) is responsible for these differences in coercivitiy.

Although domain wall injection and domain wall propagation are known to be stochastic processes, we can distinguish the observed resistance levels with some repeatability. An overlap of several MR cycles (starting at low fields below

saturation), is shown in figure 7.7 (top). The data demonstrates that while slight differences in resistance levels, due to AMR at the nucleation pad, appear, the locations of domain walls trapping along wire are somewhat repeatable. This is especially true if the sample is not saturated and only minor loops are taken (maintaining the applied field near the free-layer switching fields) as shown in the figure 7.7 (bottom). This data confirms that the domain wall tends to stop in identical locations along the wire. Ultimately this type of repeatability in a given sample depends on how well the constrictions are lithographically defined. In other words, how the constriction trapping potential compares to inherent pinning defects in the material.

7.2.2 Experiments using DC current

Experiments were performed by passing a DC current through device. Before injecting current, the sample was initialized with a magnetic field by setting it in a remanent state with a domain wall trapped in one of the constrictions. Figure 7.7 shows for a given sample, a complete sweep (left) and the initialization sweep (right). Note that in the MR curve, there is one level less than in the previous case as the domain appears to only have been trapped in one of the two constrictions (at this field sweeping rate). In the initialization curve, the field is reduced after reaching the first resistance jump. The remanent resistance is near 552 ohms.

At this point, DC current is injected through the sample with no external field applied. Figure 7.8 shows the effect of the current on the sample resistance while the schematic below depict our interpretation of the origin of this behavior. The first trace (blue), marked with '1', is fixed roughly at 552 Ohms with negative currents increasing in magnitude up to -200 μA. Subsequently the magnitude of

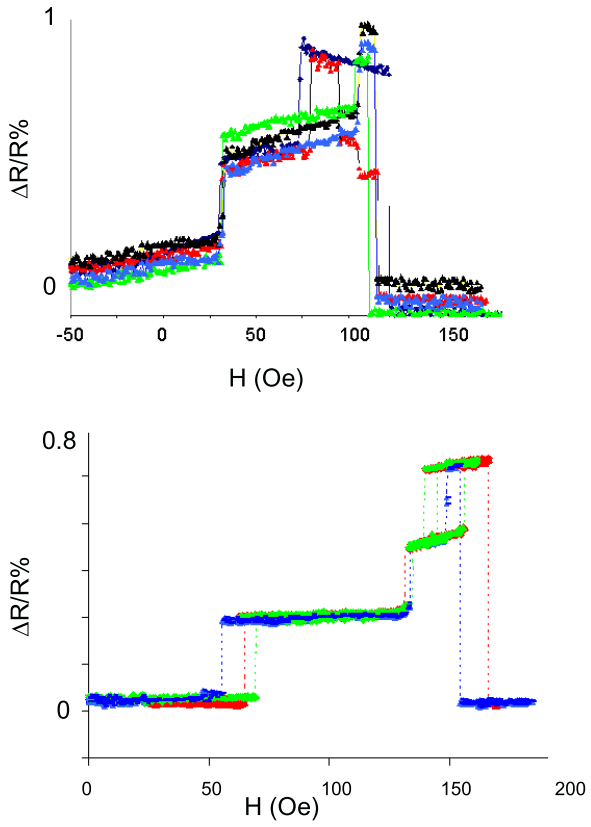

Figure 7.7: (Top) Successive MR cycles after saturating the sample between measurements. (Bottom) Successive minor loops showning repeatability in domain wall trapping positions.

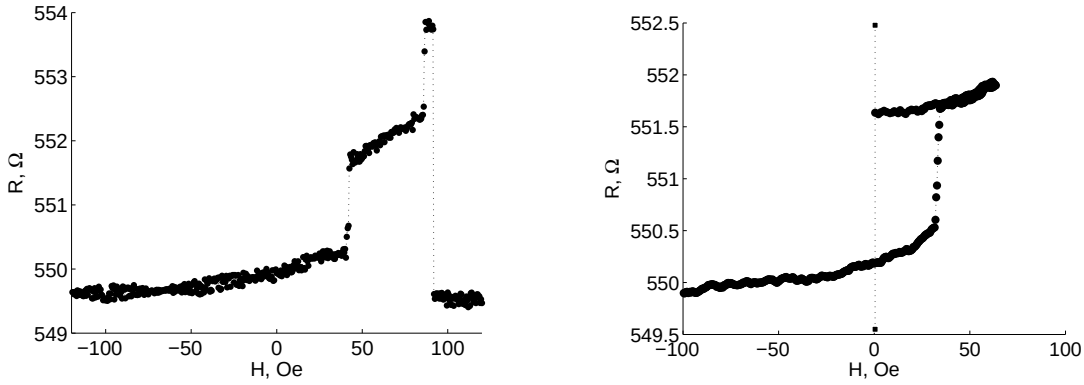

Figure 7.8: (Left) MR sweep and (right) resistance during field initialization process. This initialization process results in a trapped domain wall trapped at a constriction at zero field.

the current was reduced until zero and then increased with positive values along (black) trace '3'. At $\sim 180\mu A$, however, we observed a clear drop in resistance to a level near 550 Ohms. After increasing the current to 200 μA, we reduce it while on trace '4'(blue). For a relative high current (trace '5') near -190 μA we measure another jump in resistance up to 553 Ohms. After this event, no further jumps or drops in resistance were observed when sweeping the current in the range [-250,250] μA. We believe that in the final jump, the domain wall was completely swept out of the sample and this is why no further current induced changes were observed. Note how the resistance level observed when sweeping current coincide with the levels obtained when sweeping the field as in figure 7.8.

If we estimate the critical current density through the device (supposing current is uniform), we obtain a values below $3 \times 10^{10}\ A/m^2$. On average, for this kind of sample, these events were observed at current densities varying from $3 - 7 \times 10^{10}\ A/m^2$. These values are an order of magnitude *lower* than that obtained for the single layer permalloy samples. In fact, the current distribu-

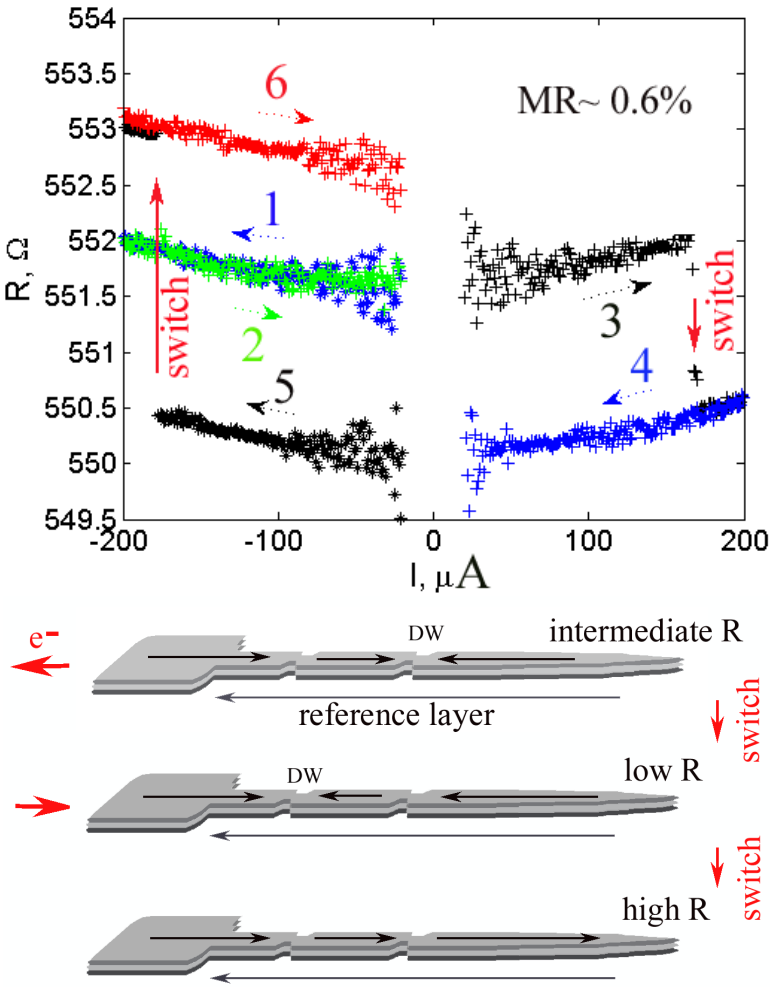

Figure 7.9: (Top) DC current induced magnetization switching, (bottom) presumed magnetization configurations at each level.

tion through the device is clearly not uniform, and a more precise estimation of the current through the free layer (taking into account layer thickness and the resistivities of the materials) leads to a critical current of less than half this value. This is an unexpectedly low value. We believe that the Oersted field from the adjacent highly conductive copper layer may be playing a significant role by assisting the motion of the DW.

7.2.3 Experiments using Fast Rising Pulses

Another set of experiments were performed by passing pulsed current through this type of device. A simple circuit was designed in order to be able to measure AC resistance while injecting fast rising current pulses through the device without perturbing the measurement. This main components of this circuit are shown in figure 7.10. On the left of the sample we describe the basic elements of the pulse generator while on the right of the sample, the basic elements required for measurement. The basic idea is to set the lock-in measurement frequency relatively low so the high frequencies in the pulse are not picked-up. With this set-up we can still detect the step-like (although the transitions appear somewhat smeared out) behavior in the magnetoresistance. An example of an AC resistance MR minor loops taken with this set-up is shown in figure 7.11. The numbered arrows show the direction of the field during measurement The data from several minor cycles shows some repeatability of the switching fields and resistance levels. An example of a MR half-cycle curve, obtained with this set-up is shown in figure 7.12. Note that in all curves (e.g. 7.11 and 7.12) obtained with this set-up, there are multiple data points between two distinct resistance levels. These points are a measurement artifact appearing as a consequence of the slow time-response of the

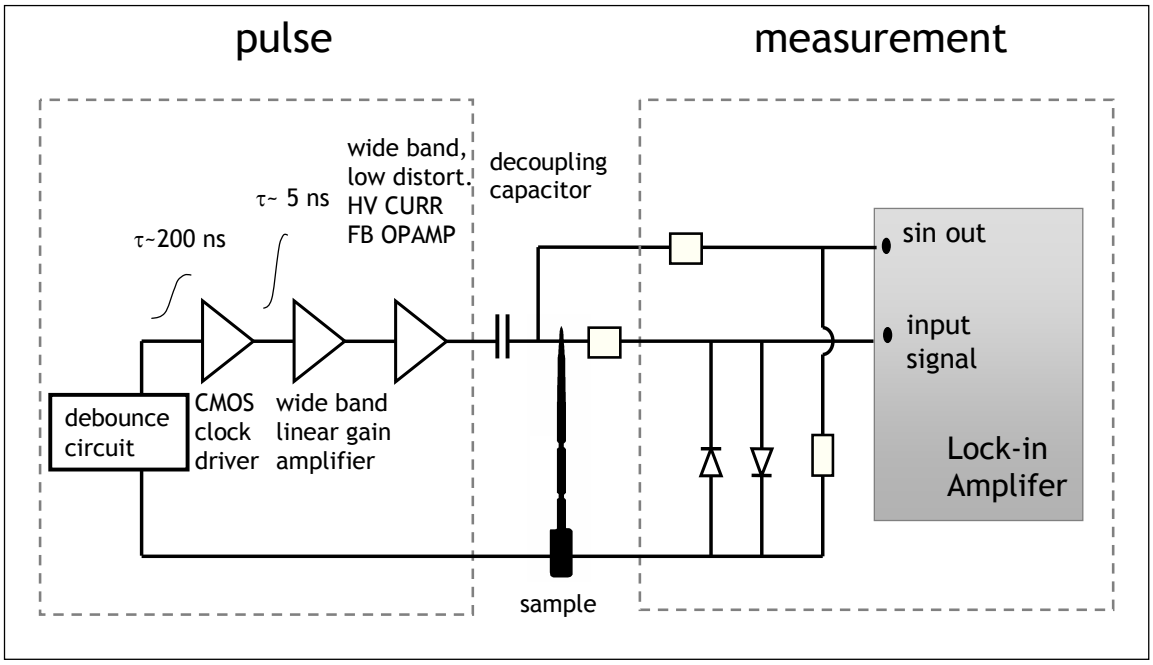

Figure 7.10: Set-up used for taking AC magnetoresistance measurements while simultaneously applying fast rising current pulses through the device without perturbing the measurement.

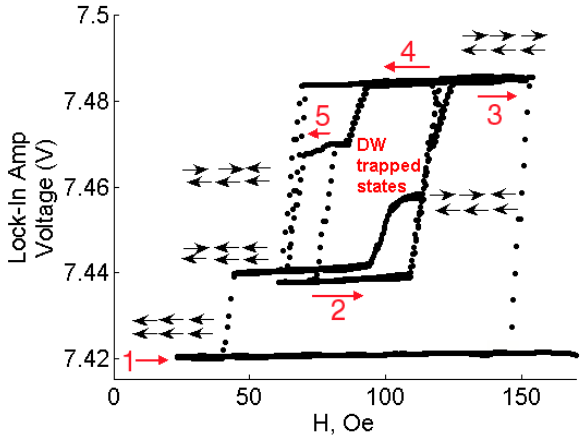

Figure 7.11: AC Magnetoresistance measurements of spin-valve device, taken in the set-up shown in figure 7.10.

system due to its low pass characteristic. Domain wall velocities are expected to be on the order of several hundred m/s, therefore the observed events are expected to occur in a nanosecond time scale.

Initial experiments were performed in the presence of low external fields and figure 7.12 shows an example of such a measurement. Figure 7.12 (top) shows a half cycle MR of this sample while in figure 7.12 (bottom) the field is held constant at values indicated on the figure. For this data, the sample was initialized in a remanent state with a domain wall trapped in one constriction. Subsequently at a given instant marked 'H' a low field near -20 Oe was applied. The small drop in resistance is a consequence from changes in the magnetization (and AMR) in the nucleation pad. Sometime after, a pulse with peak current density near $1\times10^{11} J/m^2$ was applied through the sample. At this time, marked, -P, there is a sharp drop in resistance from L2 to L1. Sometime after the field is reduced to zero and a positive field applied. These two events are marked on the figure and small changes in the resistance reveal the instants when changes in applied field occurred. Next, another pulse of same polarity is applied at the time marked -P. This time however the pulse triggers a jump in resistance. This type of experiment confirms that at the given field level, the direction of the field dictates the direction of motion. The final set of experiments were performed in absence of applied external magnetic field. In this case a succession of positive and negative pulses with magnitude above $5\times10^{10} J/m^2$ were applied. Figure 7.13 (right) shows the result of this pulse train on the sample resistance. Clearly, the pulses effectively induce switching by displacing a domain wall between trapping sites along the wire. By comparing the resulting resistance levels with those obtained in the MR measurement on the left, we find a strong correspondence. We

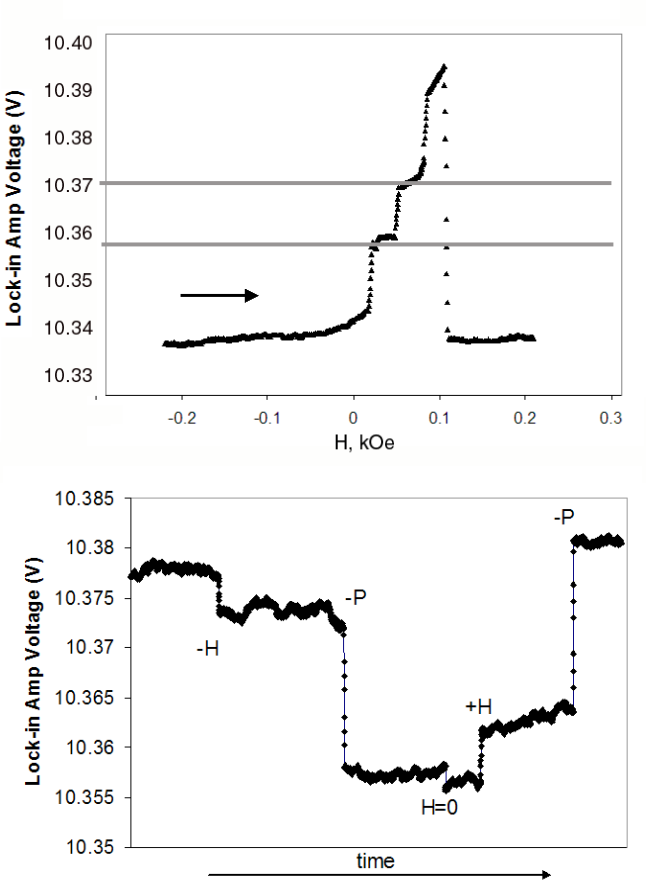

Figure 7.12: (Top) AC magnetoresistance curve, (bottom) effect of applying current pulses of same polarity in the presence of fields of opposing directions. The data confirms that motion is always in the direction of the field. Note $\pm H$ specifies moment at which field of given polarity was applied, $-P$ indicates instant at which pulse was applied through the device.

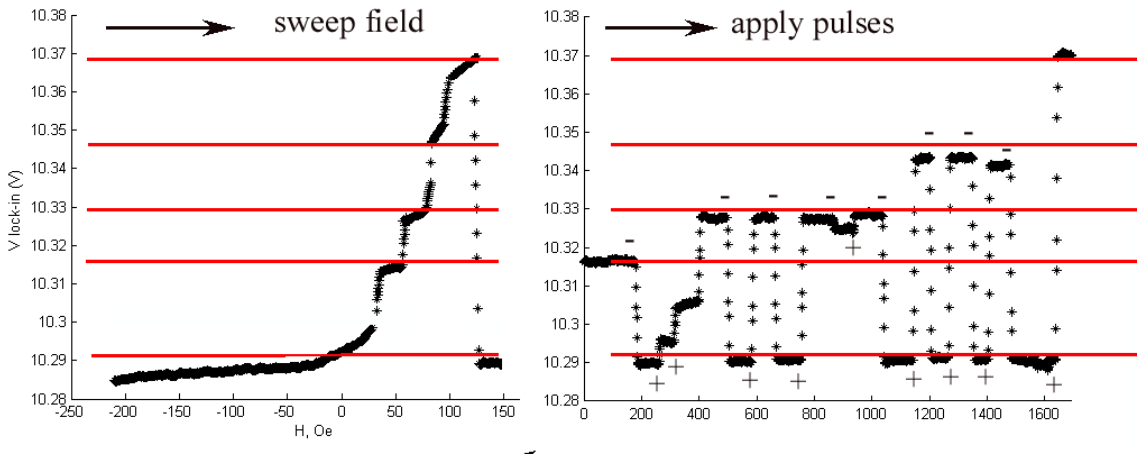

Figure 7.13: (Left) AC MR measurement for reference. (Right) Effect of applying successive positive and negative pulses to the sample in absence of applied external field. Note the correspondence between domain wall pinning sites for both curves.

thereby demonstrate the possibility of a nanoscale current controlled bi-stable device operating current densities in the mid $10^{10} A/m^2$ range.

Clearly the most important objective in this area is to determine the structure and configuration that allows current induced magnetization reversal using the lowest possible current density. The table below shows some recent advances in reducing J_c.

While it is not clear why there is a drop of almost an order or magnitude for the critical current densities measured in the spin- valve (in comparison to those measured for the permalloy sample), it is clear that the Oersted field from the neighboring highly conducting copper layer may play an important role. Other important differences are the thickness of the layers and difference in morphology of the layer beneath the permalloy (in one case SiO_2, in the other copper).

CPP J_c (A/m^2)	CIP J_c (A/m^2)
mid 10^{11} range, Hayakawaa et al.	mid 10^{11} range, Tsai et al.
mid 10^{10} range Nguyen et al.	mid 10^{11} range, Yamaguchi et al.
$low10^{10}$ range Jiang et al.	mid $10^{11}$for Py sample (this work)
	mid 10^{10} for spin-valves(this work)

Table 7.1: Recent advances in reduction of critical current densities for switching in the current perpendicular to plane (CPP) and current in plane (CIP) configurations.

Chapter 8

Strain Induced Resistance Changes in AF Coupled CoFe/Cu GMR Multilayers

8.1 Introduction

The basic mechanism in the giant magnetoresistive (GMR) effect occurring in antiferromagnetically (AF) coupled magnetic multilayers resides in the fact that the resistivity of the material depends on the magnetization configuration set up in the magnetic layers of the film. Normally, changes in resistivity are controlled through an external magnetic field. These changes however, may also be induced to some degree byimposed external stress. This is possible since magnetization is susceptible to stress through the inverse magnetostrictive effect. This type of effects has previously been studied for magnetic tunneling junctions (MTJ) and GMR spin-valve structures [184, 185]. In this study, we focus on AF coupled GMR films that contain highly magnetostrictive material and evaluate the films stress sensitivity using resistivity as a sensing parameter. In general, this is done for processes in which stress is applied under the influence of constant external fields, namely $H\sigma$ processes. In particular, we measure these effects for weakly

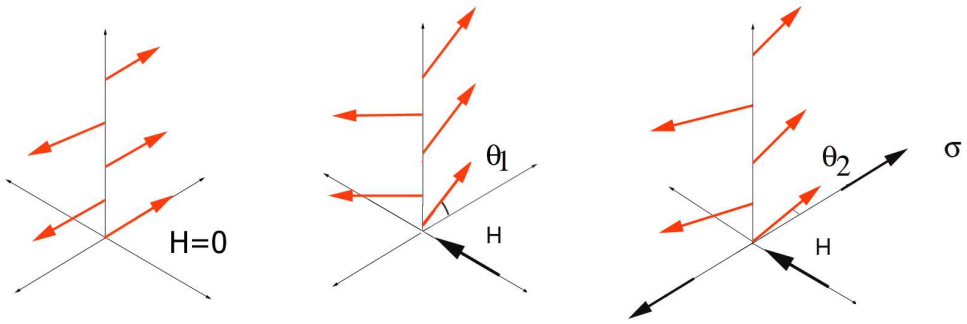

Figure 8.1: Schematic describing effects of stress on the anisotropy of the magnetic layers in an antiferromagnetically coupled multilayer.

coupled $Co_{50}Fe_{50}/Cu$ AF GMR. The strain sensitivity should be maximized for weakly coupled ML as it is related to the ratio of magnetoelastic energy and exchange energy

$$\gamma = |\frac{magnetoelastic}{exchange}| \sim \frac{3/2\lambda_s\sigma}{J_{AF}} \sim \frac{\sigma}{H_{sat}} \tag{8.1}$$

We also correlate this response with the GMR curve and explore the viability of using this effect in the development of strain sensors. Given that all layers are stressed simultaneously and that the resistivity depends strongly on these weakly coupled magnetizations, we anticipate high strain sensitivity. Figure 8.1 includes a descriptive diagram of the effect. On the left, the AF coupled layers in absence of field. In the center, a field is applied and the magnetizations now make an angle θ with the easy axis. If tensile (compressive) strain is applied, the easy axis anisotropy is increased (diminished) and the angle θ changes. We wish to determine $d\rho/d\sigma(H)$.

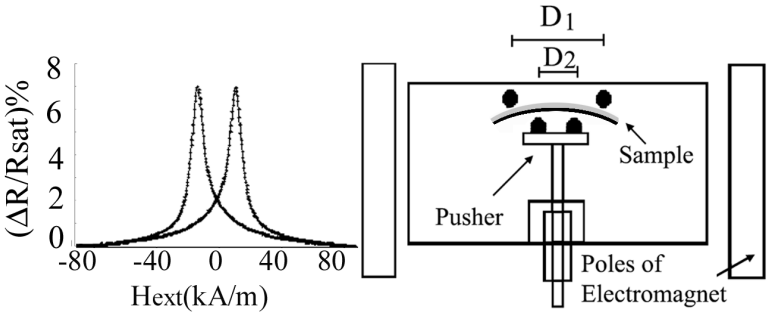

Figure 8.2: (Left) Typical GMR response of a weakly coupled multilayer and (right) measurement set-up consisting of a four-point bending device placed directly between the poles of an electromagnet.

8.2 Experimental Set-up

All samples were fabricated in a custom-built multi-target DC magnetron sputtering system with base pressure in the mid 10^{-7} torr range. These were sputtered at 3mtorr argon pressure onto 450m thick SiO_2 substrates. The structure consists of a buffer layer of 3 nm of Ta followed by $[CoFe/Cu] \times 25$ multilayer. The thickness of both the Cu layers were varied between 20-30$\mathring{A}$ while the CoFe layers are roughly near 25$\mathring{A}$, resulting in multilayers with responses up varying from $4-8\%$. A typical GMR curve is shown in figure 8.2 (left), revealing strong hysteresis and considerable ferromagnetic coupling (preventing the curve to peak at H_{ext}=0). Coercive fields (H_C) typically vary between 5-11 kA/m. These characteristics are determined by factors, such as the intrinsic coercivity of the thick CoFe layers, the weak nature of the AF coupling and the existence of rough surfaces and defects. These are especially significant since samples are unpatterned. Strain-induced four-point resistance measurements at various external fields H_{ext} were made on GMR samples cut into rectangular strips of $\sim$ 3mm$\times$15 mm. These strips were subject to external fields and strain in a four-point bending apparatus placed

between the poles of an electromagnet as shown in figure 8.2 (right). Applied strain is either tensile ε_T or compressive ε_T (ε represents magnitude) depending on whether the film is on the inner (ε_C) or outer side (ε_T) of the arc formed by the strained sample. Additionally, since the magnet can be rotated, data can be taken with strain parallel ($\varepsilon^{\parallel}$) or perpendicular ($\varepsilon^{\perp}$) to the H_{ext}. Partial differential equation plus boundary conditions, set by the system geometry, were solved through finite element modeling. The main results of this simulation, shown in figure 8.3 is the strain (ignoring magnetostrictive strain) at each point along the sample for a given pusher displacement.

8.3 Strain Measurements

A typical resistance versus strain curve, for compression applied perpendicular to $H_{ext} < H_c$, ($\varepsilon_C^{\perp}$) and for a sample with $\sim 8\%$ GMR amplitude is shown in figure 8.4. Three consecutive strain cycles up to $\varepsilon_{max} \sim 1 \times 10^{-3}$ were applied and the response was highly linear and reversible. In general, high reversibility was observed for all measurements at low field values and this may stem from the fact that the AF coupling acts as a restoring force that opposes the effects of strain in this configuration. The maximum response for this sample was $\triangle R_{\varepsilon}/R_{min}\% \sim 0.8\%$, where $\triangle R_{\varepsilon} = R(\varepsilon_C^{\perp} = \varepsilon_{max}) - R(\varepsilon_C^{\perp} = 0)$. Since effects are linear, gauge factors (GF), given by $GF = \triangle R_{\varepsilon}/R/\Delta\varepsilon$ can be obtained directly from the slope of the curve in figure 8.4. The decrease in resistance arises from two different sources, geometrical (Poisson) and magnetic. The first is completely independent of H_{ext} and causes a decrease in resistance during compression and increase in resistance during tension. The magnetic effect, results mainly from strain-induced changes in anisotropy and coercivity.

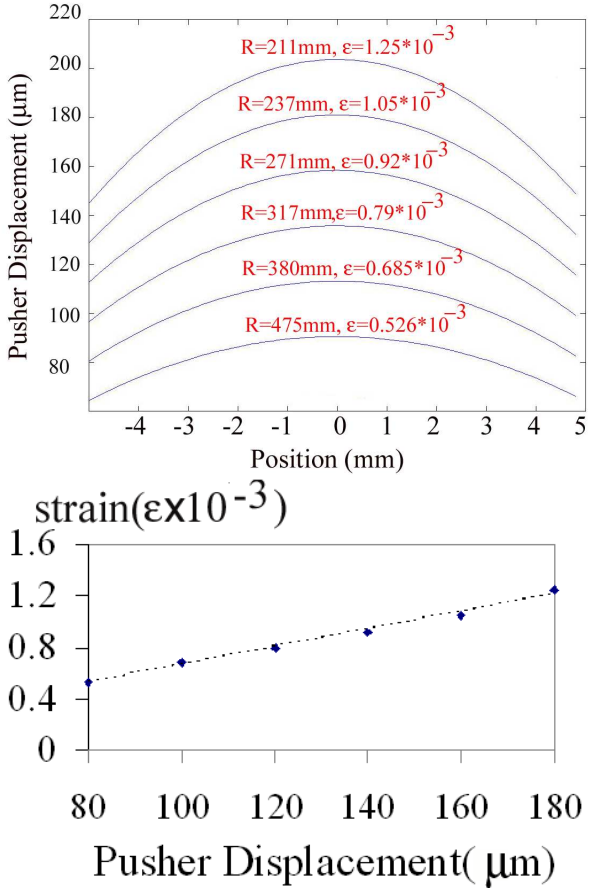

Figure 8.3: (Top) Curvature obtained (through numerical calculation) for different pusher displacements, (bottom) strain vs. pusher displacement.

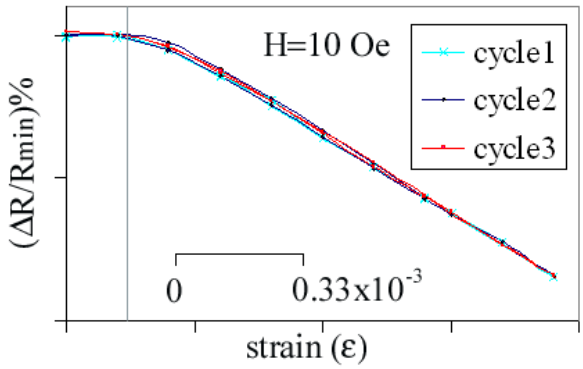

Figure 8.4: Resistance vs strain ($\varepsilon_C^{\perp}$) for applied fields below H_c.

Data from numerous measurements of this type (at different applied fields) were combined to observe the field dependence of gauge factors for this sample. Figure 8.5 contains examples of these measurements at different fields for the cases of $\varepsilon_C^{\perp}$. The blue points plotted in the bottom part of figure 8.5 specify the fields at which each of the curves in the top region, was taken. The resulting field dependence of gauge factors for this sample, for the cases of $\varepsilon_C^{\perp}$ and $\varepsilon_T^{\perp}$ is shown in figure 8.6. The solid and dashed lines correspond to the results for first and second strain cycles, respectively. Before the applying first strain cycle (not the second), the sample was magnetically initialized, by applying a negative saturation field. The field was subsequently increased to the specific field value in the data. For the second cycle the effect is greatly reduced in certain field regions. Evidently, for these fields, the strain effects are irreversible.

For all samples measured with $\varepsilon_C^{\perp}$ or $\varepsilon_T^{\parallel}$, the same general characteristics as observed in figure 8.6 (a) were obtained. These are, two dips of unequal magnitude appearing below and above H_C. This is not surprising since these configurations have equivalent effective stress fields [186]. Similarly, for $\varepsilon_T^{\perp}$ or $\varepsilon_C^{\parallel}$, two peaks above and below H_C , as shown in figure 8.6 (b). were observed. These curves allow identification of optimum field biasing condition under which response is maximum, linear and reversible. Figure 8.7, compares the strain response, in the $\varepsilon_C^{\perp}$ configuration for three GMR films. These are Co/Cu with 8% GMR and CoFe/Cu with amplitudes of 4% and 8%. It is evident that effects are notably enhanced for the samples containing CoFe and that strain effects appear to be proportional to the GMR amplitude. For the Co/Cu case, GF's remain below 2, which is typical value for regular metallic strain gauges (such as copper).

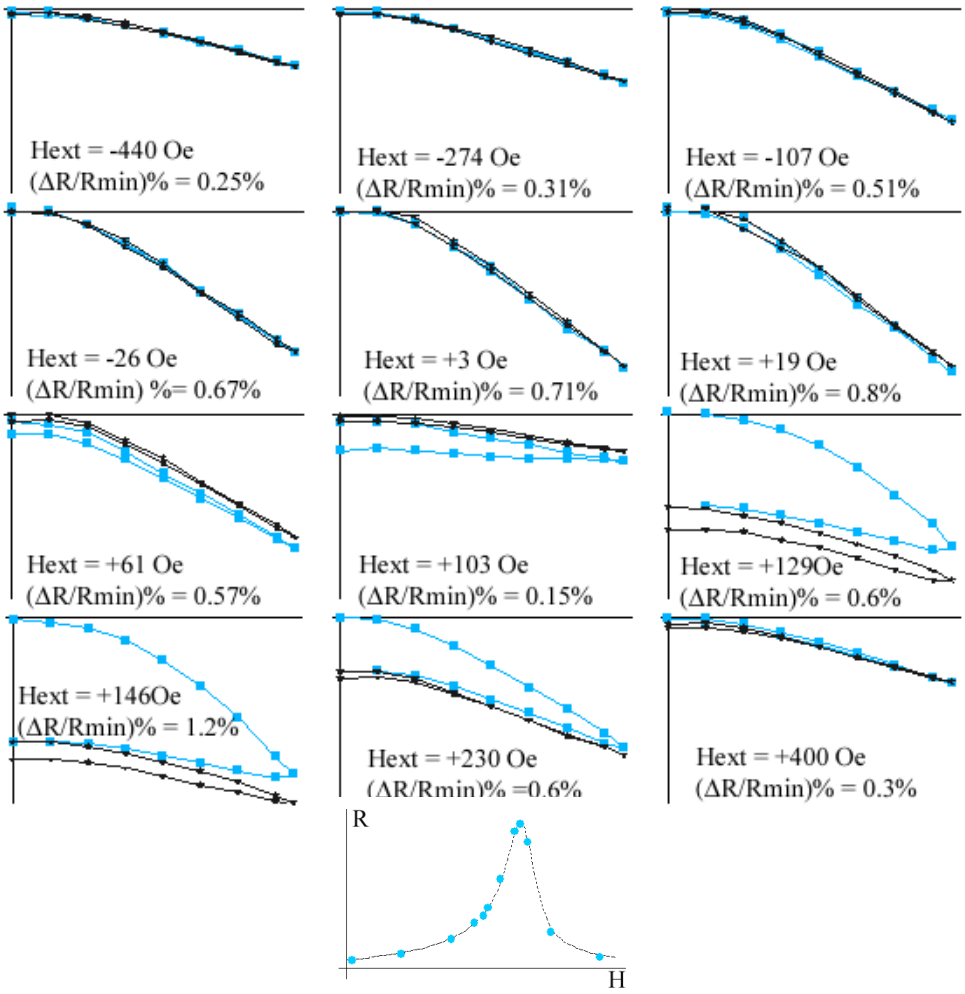

Figure 8.5: (Top) Resistance vs strain ($(\varepsilon_C^{\perp})$) for 12 different applied field values, (bottom) fields at which data was taken.

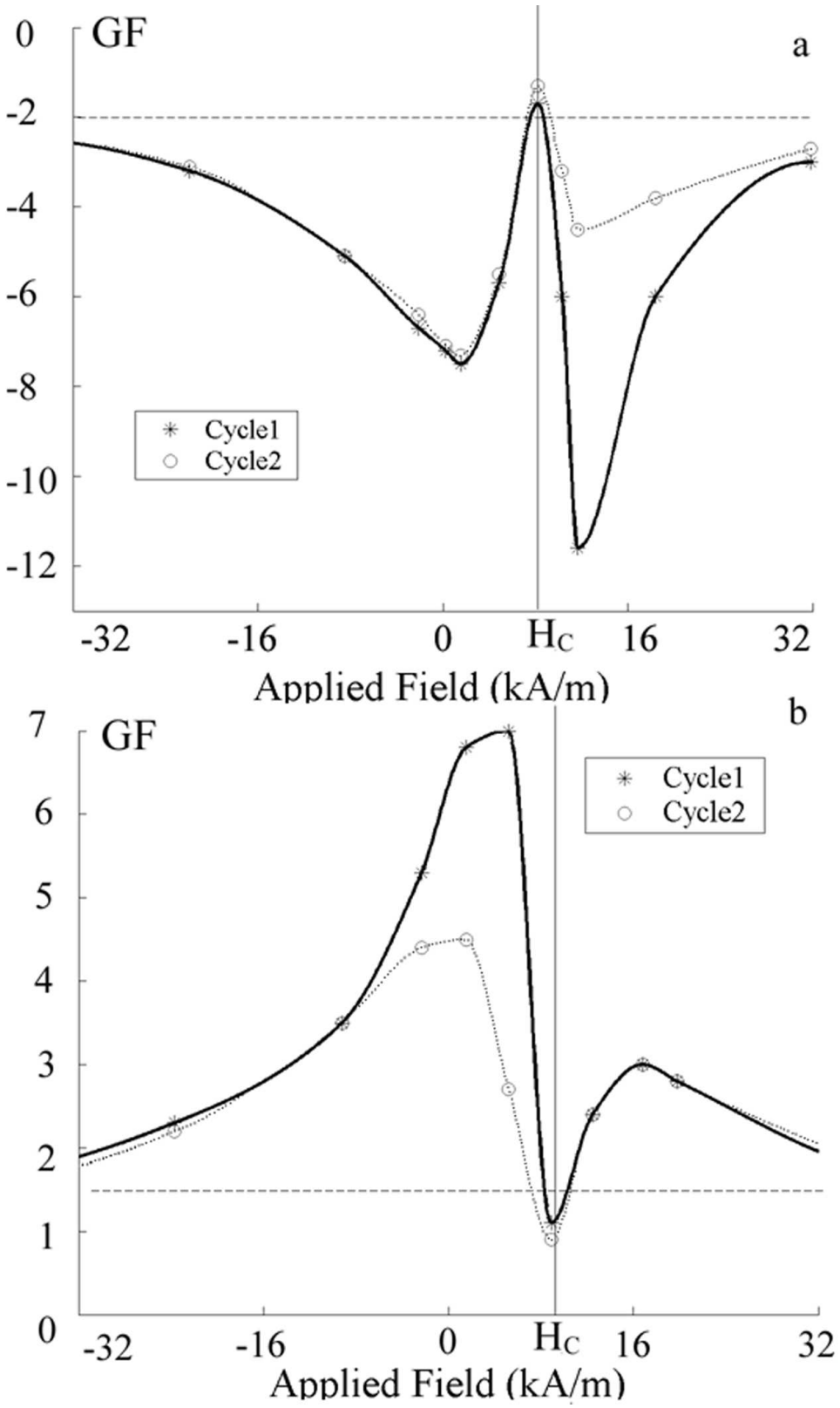

Figure 8.6: Field dependence of $\Delta R/R\%$ for (a) $\varepsilon_C^{\perp}$ or (b) $\varepsilon_T^{\perp}$.

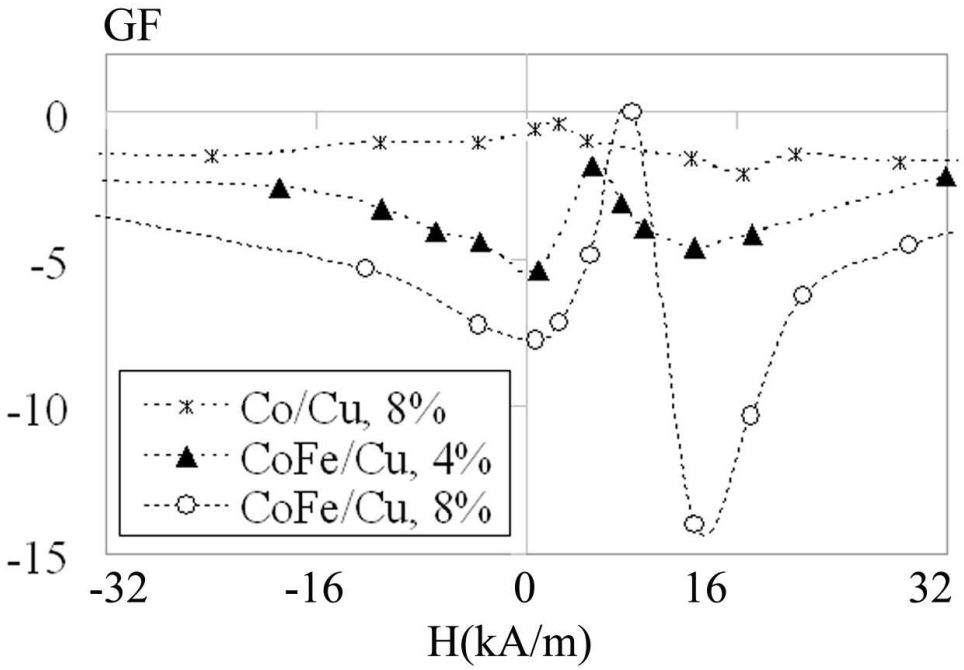

Figure 8.7: Gauge Factor vs. H_{ext} for Co/Cu (low magnetostriction) and CoFe/Cu (high magnetostriction) multilayers.

8.4 Origin of Strain-Induced Effects

One approach to understanding the magnetic effects of strain on GMR can be conceived from minimizing the total system energy [187]. Consider the simple case of two positively magnetostrictive ($\lambda_s > 0$), single domain magnetic layers of thickness t, separated by a nonmagnetic spacer. The structure is subject to an applied strain and magnetic field in the configuration. Assuming that a uniaxial in-plane anisotropy characterized by the constant k_u exists in each magnetic layer, the energy per unit area is given by:

$$E = -M_s H_{ext}(cos\alpha + cos\beta)t + 2J_{AF}cos(\alpha - \beta)t + (k_u - \frac{3}{2}\lambda_s\sigma)(cos^2\alpha + cos^2\beta)t \tag{8.2}$$

These terms represent Zeeman, interlayer exchange coupling, anisotropy and magnetoelastic coupling energies. In this case, $\varepsilon_C^{\perp}$ is applied along the easy axis (EA), thereby decreasing the effective anisotropy in this direction. Here, M_s is the saturation magnetization, J_{AF} the AF coupling parameter, and σ the applied stress. By minimizing the energy with respect to the angles α and β, it is possible to find their values for given applied stress and field. In doing this we use bulk $Co_{50}Fe_{50}$ values such as $M_s \sim 1.9 \times 10^6 A/m$ and $\lambda_s \sim 60 \times 10^{-6}$, and estimate J_{AF} from typical saturation field values for our films. Inserting the angles obtained when considering low stress values ($\sigma \sim 0.1GPa$) into the phenomenological GMR equation, we obtain the strained and unstrained GMR curves shown in figure 8.8 b. In reality however, effects are not as strong as those obtained through this calculation since magnetoelastic properties strongly depend on film thickness. For the case of $Co_{50}Fe_{50}$, it has been shown [188] that surface effects lead to a negative contribution to the magnetostriction This toy model illustrates however, the general trend of these effects. As shown in figure 8.8, $\varepsilon_C^{\perp}$ ($\varepsilon_T^{\parallel}$) increases the

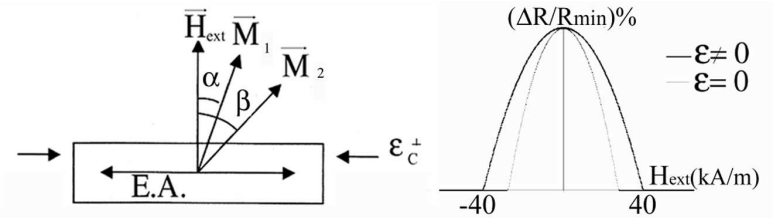

Figure 8.8: (Left) Definition of angles α and β (b) GMR for $\varepsilon_C^{\perp} \neq 0$ and $\varepsilon_C^{\perp=0}$.

anisotropy in the H_{ext} direction leading to a narrower curve under stress. Thus, we expect the resistance to decrease with applied stress in these configurations and the inverse to occur for $\varepsilon_C^{\parallel}$ ($\varepsilon_T^{\perp}$). All effects predicted by this model are reversible since it assumes changes in magnetization are purely rotational. In real samples however, there are defects, domain walls as well as surface roughness. These features lead to domain wall pinning and ferromagnetic coupling through pinholes or magnetostatic "Neél type coupling". As a result, field and stress induced hysteretic effects appear. These effects have been modeled [189], and an important conclusion of these studies is that stress also affects domain walls, by causing some of them to break away from their pinning sites. This ultimately, causes hysteretic magnetic states to always tend to anhysteretic states. Translating this to the GMR curve, implies a shift of the curve to lower field values. In other words, final magnetic states after applying stress will lie closer to the anhysteretic GMR curve. Consequently, the sign of the change in the resistance induced through this mechanism will depend on the initial conditions as depicted in Figure 8.9 (left). These effects are irreversible. It is interesting to note that these contributions to changes in resistance only oppose those of the AF coupling, at high fields above H_C. This is may explain the high reversibility observed in the low field region. Combining these contributions, we expect for $\varepsilon_C^{\perp}$ or $\varepsilon_T^{\parallel}$, that the stressed curve would be both narrower and shifted to lower

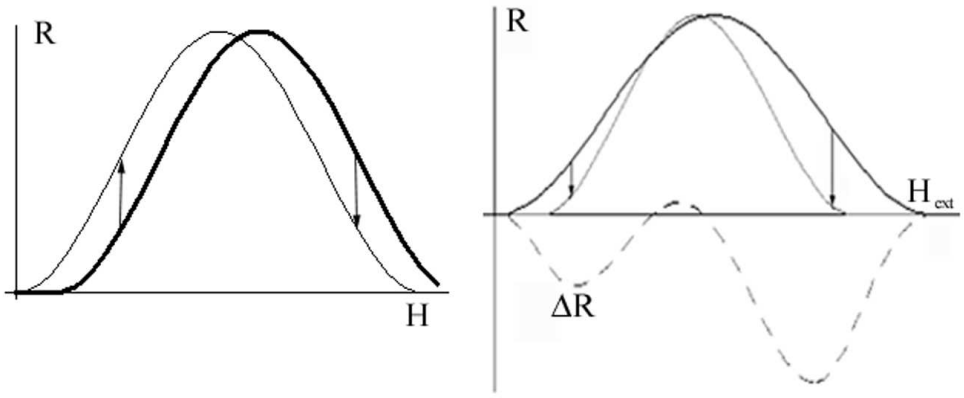

Figure 8.9: (a) Effects of $\varepsilon_C^{\perp}$ stress GMR due to domain wall effects(irreversible effects). (b) Strained and unstrained R vs. H curves and their difference (considering both reversible and irreversible effects).

fields. Figure 8.9 (right) shows these curves as well as their difference (dashed curve in Fig. 8.9(right)). The general form of the difference (dashed) curve and the experimental result for strain-field sensitivity in figure 8.6(a) are strikingly similar. The difference in the offset between figure 8.9 (right) and 8.6(a) arises due to the geometric effect on the resistance. Similar analysis on the tensile case generates the positive peaks shown in figure 8.6(b) suggesting that the observed universal behavior originates from these two well-known phenomenological effects. Thus, under appropriate field biasing conditions AF GMR coupling enhances strain sensitivity and response exhibits the desirable characteristics of linearity and reversibility (even for hysteretic samples). There is also ample room for optimization, since effects depend strongly on multilayer characteristics such as, thickness of the magnetic layer and GMR amplitude. Further optimization can be achieved by tailoring anisotropies through patterning and annealing.

APPENDIX: Sample Fabrication Process Large Au contact

Photolithography Process:

1. Spin on NRZ-1500 Py photoresist at 4000 rpm
2. Bake 120°C for 1 min.
3. Expose (contact aligner) for 12 sec at 12 mW/cm^2
4. Bake at 120°C for 1 min.
5. Develop using RD-6 for 12 sec.
6. Rinse DI.
7. Blow dry N_2.
8. Oxygen plasma etch at 100W for ∼15 sec.
9. Evaporate metal.
10. Lift-off in RR2 at 90°C.

E-beam lithography Process:

1. Spin-on MMAEL-II/EL THINNER (MMA 8.5 EL) at 3000 rpm for 1 min.
2. Bake at 180°C 5 min.
3. Spin-on 950 PMMA A4 (anisol) at 5000 rpm for 1 min.
4. Bake at 180°C 5 min.
5. Expose using e-beam.
6. Develop by dipping in MIBK/IPA (1:3) for 1 min
7. Rinse in IPA 30 sec.
8. Blow dry N_2.
9. Oxygen plasma etch at 100W for ∼15 sec.
10. Evaporate film.
11. Lift-off in acetone.

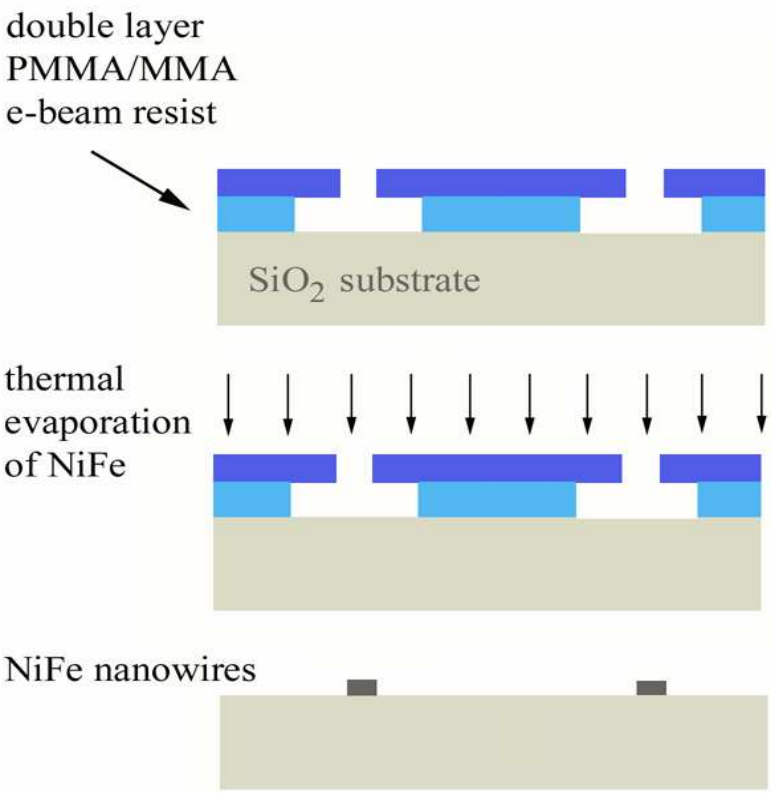

Figure 8.10: Schematic of fabrication process showing undercut profile obtained using double layer MMA/PMMA. This appears due to the higher sensitivity of MMA to e-beam exposure and ultimately facilitates lift-off.

APPENDIX:OOMMF Micromagnetic Simulator Overview

The first step in using OOMMF is to define the specific problem. This includes defining the material characteristics, geometry of the sample, initial magnetic state and the magnetic fields to be applied in the given experiment. Simulation parameters such as the characteristics of the finite element mesh and the criteria for convergence are other important input parameters.

The solution 'solves' the problem by integrating the Landau-Liftshitz-Gilbert [118, 120] equation

$$\frac{d\mathbf{M}}{dt} = -|\gamma|\mathbf{M} \times \mathbf{H}_{eff} - \frac{|\gamma|\alpha}{M_s}\mathbf{M} \times (\mathbf{M} \times \mathbf{H}_{eff}) \tag{8.3}$$

Where M is the magnetization (A/m), γ the gyromagnetic ratio (m/(A.s)), α the dimensionless damping coefficient and H_{eff} the effective field (A/m). Further details concerning the conceptual origin and significance of this equation can be found in section **.

The effective field is calculated from (in SI)

$$\mathbf{H}_{eff} = -\mu_0^{-1}\frac{\partial E}{\partial \mathbf{M}} \tag{8.4}$$

While the average density $E(\mathbf{M})$ is obtained using Brown's equation [111]. This includes anisotropy, exchange, self-magnetostatic and Zeeman terms.

For the calculation, the micromagnetic problem is impressed on regular 2D mesh of squares, with 3D magnetization spins positioned at the center of the square. For each cell, assuming constant magnetization within, the anisotropy and applied field energy terms are calculated. The exchange energy is calculated using the eight-neighbor bilinear interpolation described in [116, 117], with Neumann boundary conditions.

The magnetostatic field is far the most consuming in terms of computer time. In OOMMF it is calculated as the convolution of the magnetization for a given *kernel*, that represents different interpretations of the discrete magnetization and the cell to cell magnetostatic interaction. Several kernel are supported within the software, but we used the simplest one for which the the magnetization is constant in each cell, and computes the average demagnetization field through the cell by using the formula described in [123]. Although we will not going into details concerning details of calculation we mention that this convolution is evaluated using fast Fourier transform (FFT) techniques. The Landau-Lifshitz ODE, on the other hand is integrated using a second order predictor-corrector technique of the Adams type. Further details concerning this process can be found at [113].

BIBLIOGRAPHY

[1] P. Weiss, *J. Phys.* (Paris) **6**, 661 (1907).

[2] W. Heisenberg, *Z. Phys.* **38**, 411 (1926).

[3] W. Heisenberg, *Z.Phys.* **49**, 619 (1928).

[4] P. A. M. Dirac, *Proc. Soc. London, Ser. A* **112**, 661 (1926).

[5] P. A. M. Dirac, *Proc. Soc. London, Ser. A* **123**, 714 (1929)

[6] F. Bloch, *Zeit. Phys.* **61** (1930) 206.

[7] F. Bloch, *Z. Phys.* **74**, 295 (1932).

[8] L. D. Landau and E. Liftshitz, *Phys.Z.Soweit* **8**, 153 (1935).

[9] L. Neél, *C. R. Acad. Sci.* **241**, 533 (1955).

[10] H. D. Dietze and H. Thomas, *Z. Physik* 523 **163**,(1961).

[11] H. Reidel and A. Seeger,*Phys.Stat. Sol.(b)* **46**, 377 (1971).

[12] D. V. Berkov, K. Ramstock and A. Hubert, *Phys.Status. Solidi A* **137**, 207 (1993).

[13] R. Kishner, W. Doring, *J.Appl. Phys.***39**, 855 (1968).

[14] W. F. Brown and A. E. Labonte, *J.Appl.Phys.* **36**, 1380 (1965).

[15] A. E. Labonte, *J. Appl. Phys.* **40**, 2450 (1970).

[16] A. E. Labonte, PhD Thesis, University of Minnesota (1966).

[17] A. Aharoni, *J. Appl. Phys.* **38**,3196 (1967).

[18] A. Aharoni,*Introduction to the Theory of Ferromagnetism*, Second edition. Oxford Press (2000).

[19] A. Hubert, *Phys. Status Solidi*, **32**, 519 (1969).

[20] A. Hubert, *Phys. Status Solidi*, **38**, 699 (1970).

[21] P. Bruno, *Phys. Rev. Lett.* **83**, 12. 2425 (1999).

[22] R. D. McMichael and M. J. Donahue, *IEEE Trans. Mag.* **33**, 4167 (1997).

[23] Y. Martin, H. Wickramasinghe, *Appl. Phys. Lett.* **50**, 1455 (1987).

[24] Y. Martin, D. Rugar and H.K. Wickramasinghe, *Appl. Phys. Lett.*, **52** , 244 (1988).

[25] G. Binnig, H. Rohrer, Ch. Gerber and E. Wiebel, *Phys. Rev. Lett.* **50**, 120 (1982).

[26] G. Binnig US Pat. RE 33 387 (1985).

[27] G. Binnig, H Rohrer, C.F. Quate, Ch. Gerber, *Phys. Rev. Lett.* **56**, 930 (1986).

[28] U. Drig, J.K. Gimzewski, D.W. Pohl, and R. Schlitter, *IBM Res. Rep.* **RZ1513** (1986).

[29] T. R. Albrech, P. Grtter, D. Horne , and D. Rugar, *IBM Res. Rep.* **RJ7681** (1990).

[30] A. W. Adamson, A. P. Gast. *Physical Chemistry of Surfaces*, 6th Edition (1997).

[31] H. J. Hug, A. Moser, Th. Jung, O. Fritz, A. Wadas, I. Parashikov and H. J. Guntherodt, *Rev. Sci. Instrum.* **64**, 2820 (1993).

[32] S.H. Chung, S. R. Shinde, S.B. Ogale, T. Venkatesan, *J. Appl. Phys.* **89**, 6784 (2001).

[33] S. H. Chung, S. R. Shinde, S. B. Ogale, A. Biswas, *IEEE Trans. Magn.* **38**, 2886 (2002).

[34] M. Dreyer, M. Kleiber, R.Wiesendanger, *Appl. Phys. A* **69**, 359 (1999).

[35] M. Dreyer, C. Krafft, R.D. Gomez, *IEEE Trans. Magn,* **38**, 2538 (2002).

[36] J. Losch, U. Memmert, U. Hartmann, *J. Magn. Magn. Mat.* **226**, 1597 (2001).

[37] M. Dreyer, R.D. Gomez, I. D. Mayergoyz, *IEEE Trans. Magn.* **36**, 2975 (2000).

[38] M. Ruhrig, S. Porthun, J.C. Lodder, S. McVitie, *J. Appl. Phys*, **79**, 2913 (1996).

[39] G. N. Phillips, M. Siekman, L. Abelmann, and J. C. Lodder, *Appl. Phys. Lett.* **81**, 866 (2002).

[40] A. R. Champagne, A. J. Couture, F. Kuemmeth, and D. C. Ralph, *Appl. Phys Lett.* **82**, 1111 (2003).

[41] Z. Deng, E. Yenilmez, J. Leu, J. E. Hoffman and Eric W. J. Straver, H. Dai, K. A. Moler, *Appl. Phys. Lett.* **85**, 6263 (2004).

[42] U. Hartmann *Phys. Lett. A* **137**, 475 (1989).

[43] A. Wadas, P. Gmetter, and H. Guntherodt, *J. Vac. Sci. Tech. A.* **8**, 416419 (1990).

[44] A Wadas and P. Gruetter, *Phys. Rev. B* **39**,(1989).

[45] U. Hartman, *J. Vac. Sci. Tech. A* **88**, 411 (1990).

[46] C. Schoenenberger and S. Alvarado, *Z. Phys. B* **80**, 373,(1990).

[47] P. J. A. van Schendel, H. J. Hug, B. Stiefel, S. Martin, and H.-J. Guntherodt, *J. Appl. Phys.* **88**, 435 (2000).

[48] F. Liu, S. Li, Y. Liu, G. Gray, and A. Schultz. *J. Appl. Phys.***91**, 6842 (2002).

[49] E.T. Yen, T. Thomson,J.-P. Chen, H.J. Richter, *IEEE Trans. Magn.* **36**, 2330 (2000).

[50] R. B. Proksch, S. Foss, E. D. Dahlberg, *IEEE Trans. Magn.* **30** 4467 (1994).

[51] K. Babcock, V. Elings, M. Dugas, S. Loper, *IEEE Trans. Magn.* **30**, 4503 (1994).

[52] L. Kong and S. Y. Chou, *J. Appl. Phys.* **81**, 5026 (1997).

[53] L. Kong L and S. Y. Chou, *Appl. Phys. Lett.* **70** 2043 (1997).

[54] J. Lohau, S. Kirsch ,A. Carl, G. Dumpich and E.F. Wassermann *J. Appl. Phys.* **86**, 3410 (1999).

[55] J. Lohau, S. Kirsch, A Carl, E.F. Wassermann, *Appl. Phys. Lett.* **76**, 3094 (2000).

[56] E. F. Wassermann, C. Burgel, A. Carl, J. Lohau, *Magn. Magn. Mat.* **239**, 220 (2002).

[57] J. Lohau, A. Carl, S. Kirsch, E.F. Wassermann, *Appl. Phys. Lett.* **78**, 2020 (2001).

[58] M. V. Rastei, R. Meckenstock, and J. P. Bucher, *Appl. Phys. Lett.* **87**, 222505 (2005).

[59] J. Vergara, P. Eames, C. Merton, V. Madurga, *Appl. Phys. Lett.* **84**, 1156 (2004).

[60] T. Goddenhenrich, H. Lemke, M. Muck, U. Hartmann, and C. Heiden. *Appl. Phys. Lett.* **57**, 2612 (1990).

[61] K. L. Babcock, V. B. Elings, J. Shi, D. D. Awschalom, and M. Dugas, *Appl. Phys. Lett.* **69**, 705 (1996).

[62] A. Thiaville, L. Belliard, D. Majer, E. Zeldov, and J. Miltat, *J. Appl. Phys.* **82**, 3182 (1997).

[63] P. J. A. van Schendel, H. J. Hug, B. Stiefel, S. Martin, and H.J. Güntherodt, *J. Appl. Phys.* **88**, 435 (2000).

[64] S. McVitie, R. P. Ferrier, J. Scott, G. S. White, and A. Gallagher.*J. Appl. Phys.* **89**, 3656 (2001).

[65] D. G. Streblechenko, M. R. Sheinfein, M. Mankos, and K. Babcock, *IEEE Trans. Magn.* **32**, 4124 (1996).

[66] R. P. Ferrier, S. McVitie, A. Gallagher, and W. A. P. Nicholson, *IEEE Trans. Magn.* **33**, 4062 (1997).

[67] J. Scott, S. McVitie, R. P. Ferrier, G. P. Heydon, W. M. Rainforth, M. R.J. Gibbs, J. W. Tucker, H. A. Davies, and J. E. L. Bishop, *IEEE Trans.Magn.* **35**, 3986 (1999).

[68] X. Zhu, P. Grtter, Y. Hao, F. J. Castano, S. Haratani, C. A. Ross, H. I. Smith, B. Vogeli, and H. I. Smith, *J. Appl. Phys.* **93**1132 (2003).

[69] T. Chang, M. Lagerquist, J. Zhu, J. H. Judy, P. B. Fischer and S. Y. Chou. *IEEE Trans. Magn.* **28**, 3138 (1992).

[70] N. Mott *Proc. Phys. Soc.* **47** 571(1935).

[71] N.Mott, *Proc. Roy. Soc.* A **153**, 699 (1936).

[72] M .N. Baibich, J.M. Broto, A. Fert, F. Nguyen Van Dau, F. Petroff, P. Eitenne, G. Creuzet, A. Friederich, and J. Chazelas, *Phys. Rev. Lett.* **61**, 2472 (1988).

[73] P. Grnberg, R. Schreiber, Y. Pang, M. B. Brodsky and H. Sowers, *Phys. Rev. Lett.* **57**, 2442 (1986).

[74] M.A. Ruderman and C. Kittel. *Phys. Rev.*, **96**,99, (1954).

[75] G. G. Cabrera and L. M. Falicov, *Phys.Status Solidi B* **61**, 539 (1974)

[76] G. G. Cabrera and L. M. Falicov, *Phys. Status Solidi B*, **62**, 217 (1974).

[77] L. Berger, *J. App. Phys.* **49**, 2156 (1978).

[78] J.F. Gregg, W. Allen, K. Oundjaela, M. Viret, M. Hehn, S.M. Thompson, and J.M. D. Coey, *Phys. Rev. Lett.* **77**, 1580 (1996).

[79] Rudiger, J. Yu, A. D.Kent and S. S. P. Parkin, *Appl. Phys. Lett.* **73**, 9,1298 (1998).

[80] A. D. Kent et al., *IEEE Trans. Magn.* **34**, 900 (1998).

[81] K. Hong and N. Giordano, *J. Phys. Cond. Matter.* **10**, L401 (1998).

[82] N. Garcia, M. Munoz, and Y.W. Zhao, *Phys. Rev. Lett.* **82**, 2923 (1999).

[83] G. Tatara, Y.W. Zhao, M. Munoz, and N. Garcia, *Phys. Rev Lett.* **83**, 2030 (1999).

[84] S. H. Chung, M. Muoz, N. Garca, W. F. Egelhoff, and R. D. Gomez, *J. Appl. Phys.* **93**, 10, 7939 (2003).

[85] Y. Otani, S. G. Kim, and K. Fukamichi, *IEEE Trans. Magn.* **34,** 1096 (1998).

[86] T. Taniyama, I. Nakatani, H. Yanagihara and E. Kita, *J. Magn. Magn. Mat.* **196**, 77 (1999).

[87] S. J. C. H. Theeuwen J. Caro, K. I. Schreurs, R. P. van Gorkom, K. P. Wellock, R. M. Jungblut, W. Oepts, R. Coehoorn and V. I. Kozub *J. Appl. Phys.* **89**, 4442 (2000).

[88] U. Ebels A. Radulescu, Y. Henry, L. Piraux and K. Ounadjela, *Phys. Rev. Lett.* **84**, 983 (2000).

[89] Y. B. Xu, C. A. F. Vaz, A. Hirohata, H. T. Leung, C. C. Yao, and J. A. C. Bland,E. Cambril, F. Rousseaux, and H. Launois, *Phys. Rev. B* **61,** R14901 (2000).

[90] C. Yu, S.F. Lee, J. L. Tsai, E.W. Huang, T. Y. Chen, Y.D. Yao, Y. Liou and C. R. Chang, *J. Appl. Phys.* **93**, 8761 (2003).

[91] D. Buntinx, S. Brems, A. Volodin, K. Temst, C. Van Haesendonck, *Phys. Rev. Lett.* 017204,(2005).

[92] A. O. Adeyeye, R. P. Cowburn, M. E.Welland, *J. Appl. Phys.* **87**, 299 (2000).

[93] A. O. Adeyeye and M. E. Welland, *J. Appl. Phys.* **92**, 3896 (2002).

[94] M. Klaui, C. A. F. Vaz, J. A. C. Bland, *J. Appl. Phys.* **93**, 7885 (2003).

[95] D. Lacour, J.A. Katin, L. Folks, T. Block, J.R. Childress, M. J. Carey and B. A. Gurney, *Appl. Phys. Lett.* **84**, 1910 (2004).

[96] A. D. Kent, J. Yu, U. Rudiger and S. S. P. Parkin, *J. Phys.:Condens. Matter* **13**, R461 (2001)

[97] M. Viret, D. Vignoles, D. Cole, and J. M. D. Coey, W. Allen, D. S. Daniel,

and J. F. Gregg, *Phys. Rev. B* **53**, 8464 (1996).

[98] P. M. Levy and S. Zhang, *Phys. Rev. Lett.* **79**, 5110 (1997).

[99] R. P. van Gorkom, A. Brataas, and G. E. W. Bauer, *Phys. Rev. Lett.* **83**, 4401 (1999).

[100] A. Brataas, G. Tatara and G. E. Bauer, *Phys. Rev. B.* **60**, 3406 (1999).

[101] G. Tatara and H. Fukuyama, *Phys. Rev. Lett.* **78**, 3773 (1997).

[102] G. Tatara and H. Fukuyama, *J. Magn. Magn. Mater.* **177**, 193 (1998).

[103] G. Tatara and N. Garcia, *IEEE Trans.Magn.* **36**, 2839 (2000).

[104] G. Tatara, *J. Phys. Soc. Jap.* **69**, 2969 (2000).

[105] G. Tatara,Y. Tokura, *Solid State Communications*, **116**, 533 (2000).

[106] Tatara, G.; Zhao, Y.-W.; Munoz, M.; Garcia, N., *Phys. Rev. Lett.* **83**, 2030 (1999).

[107] G. Tatara, *Int. J. of Mod. Phys. B.* **15**, 321 (2001).

[108] G. Tatara, N. Vernier, J. Ferre, *Appl. Phys. Lett.* **86**, 252509 (2005).

[109] V. K. Dugaev, J. Berajdar and J. Barnas, *Phys. Rev. B.* **68**, 104434 (2003).

[110] L. Berger, *Phys. Rev. B.* **73**, 014407 (2006).

[111] W. F. Brown, Jr., Micromagnetics (Krieger, New York, 1978).

[112] A. Aharoni, Introduction to the Theory of Ferromagnetism (Oxford, New York, 1996).

[113] http://math.nist.gov/oommf/

[114] A. Aharoni, *J. App. Phys.* **83**, 3432 (1999).

[115] D. V. Berkov, K. Ramstock, and A. Hubert, *Phys. Stat. Sol. (a)* **137**, 207 (1993).

[116] M.J. Donahue and R. D. McMichael, *Physica B* **233**, 278 (1997).

[117] M. J. Donahue and D. G. Porter, OOMMF User's Guide, Version 1.0," Technical Report No. NISTIR 6376, National Institute of Standards and Technology, Gaithersburg, MD (1999).

[118] T. L. Gilbert, *Phys. Rev.* **100**, 1243 (1955).

[119] P. R.Gillette and K. Oshima, *J. Appl. Phys.* **29**, 529 (1958).

[120] L. Landau and E. Lifshitz, *Physik. Z.* **8**, 153 (1935).

[121] R. D. McMichael and M. J. Donahue, *IEEE Trans. Mag.* **33**, 4167,(1997).

[122] L. Néel, *Adv. Phys.* **4**, 191 (1955).

[123] A. J. Newell, W. Williams, and D. J. Dunlop, *J. Geophysical Research* **98**, 9551(1993).

[124] D. G. Porter and M. J. Donahue, *J. Appl. Phys.* **89**, 7257 (2001).

[125] M. R. Scheinfein, J. Unguris, J. L. Blue, K. J. Coakley, D. T. Pierce, and R. J. Celotta, *Phys. Rev. B* **43**, 3395 (1991).

[126] J. D. Burton, A. Kashyap, M. Ye. Zhuravlev, R. Skomski, E. Y. Tsymbal, and S. S. Jaswal, O. N. Mryasov and R. W. Chantrell, *App. Phys. Lett.* **85**, 251 (2004).

[127] L. Berger, *J. App. Phys.* **50**, 2137 (1979).

[128] Y. Hsu and L. Berger, *J. App. Phys.* **53**, 7873 (1982).

[129] L. Berger, *J. App. Phys.* **55**, 1954 (1984).

[130] P. P. Freitas and L. Berger, *J. App. Phys.* **57**, 1266 (1985).

[131] L. Berger, *Phys. Rev. B* **33**, 1572 (1986).

[132] L. Berger, *J. App. Phys.* **63**, 1266 (1988).

[133] L. Berger, *J. App. Phys.* **63**, 1663 (1988).

[134] C.-Y. Hung and L. Berger, *J. App. Phys.* **63**, 4276 (1988).

[135] C.-Y. Hung, L. Berger and C. Y. Shih, *J. App. Phys.* **67**, 5941 (1990).

[136] L. Berger,*J. App. Phys.* **69**, 4683 (1991).

[137] L. Berger, *J. App. Phys.* **71**, 2721 (1992).

[138] E. Salhi and L.Berger, *J. App. Phys.* **73**, 6405 (1993).

[139] E. Salhi and L.Berger, *J. App. Phys.* **76**, 4787 (1994).

[140] L. Berger, *Phys. Rev. B* **54**, 9353 (1996).

[141] W. Sholz, H. Forester, D. Suess, T. Schrefl and J Fidler, *Comp. Mat. Science* **25**, 540 (2002).

[142] S. Jen and L. Berger, *J. Appl. Phys.* **53**, 2298 (1982).

[143] R. J. Weiss and A. S. Marota, *J. Phys. Chem. Solids* **9**, 302 (1959).

[144] S. Middelhoek. *IBM J. Res. Develop.* **10**, 351 (1966).

[145] S. Zhang and Z. Li, *Phys. Rev. Lett.* **93**, 127204 (2004).

[146] Ya. B. Bazaliy, B. A. Jones, and S. C. Zhang, *Phys. Rev. B* **57**, R3213 (1998).

[147] G. Tatara and H. Fukuyama, *Phys. Rev. Lett.* **78**, 3773 (1997).

[148] J. He, Z. Li, and S. Zhang *J. Appl. Phys.* **98**, 016108 (2005)

[149] L. Gan, S.H. Chung, K.H. Aschenbach, M. Dreyer and R. D. Gomez, *IEEE Tran. Magn.* **36**, 3047 (2000).

[150] M. Tsoi, R. E. Fontana, and S. S. P. Parkin, *App. Phys. Lett.* **83**, 2617 (2003).

[151] T. Kimura and Y. Otani, *J. Appl. Phys.* **94**, 7266 (2003).

[152] A. Yamaguchi, T. Ono, S. Nasu, K. Miyake, K. Mibu, T. Shinjo, *Phys. Rev. Lett.* **92**, 077205 (2004).

[153] C. K. Lim, T. Devolder, C. Chappert, J. Grollier, V. Cros, A. Vaures, A. Fert, G. Faini, *Appl. Phys. Lett.* **84**, 2820 (2004).

[154] N. Vernier, D. A. Allwood, D. Atkinson, M. D. Cooke and R. P. Cowburn, *Europhys. Lett.* **65**, 526 (2004).

[155] A. Thiaville, Y. Nakatani, J. Miltat, and N. Vernier, *J. Appl. Phys.* **95**, 7049 (2004).

[156] G. Tatara, H. Kohno, *Phys. Rev. Lett.* **92**, 086601 (2004).

[157] 10 Z. Li and S. Zhang, *Phys. Rev. Lett.* **92**, 207203 (2004).

[158] X. Waintal and M. Viret, *Europhys. Lett.* **65**, 427 (2004).

[159] N. Vernier, D. A. Allwood, D. Atkinson, M. D. Cooke, and R. P. Cowburn, *Europhys. Lett.* **65**, 526 (2004).

[160] S. H. Florez, M. Dreyer, K. Schwab, C. Sanchez, and R. D. Gomez *J. Appl. Phys.* **95**, 6720 (2004).

[161] S. H. Florez, C. Krafft, R. D. Gomez, *J. Appl. Phys.* **97**, 10C705 (2005).

[162] R. O'Handley, "Modern Magnetic Materials: Principles and Applications", Wiley and Sons, New York (2001).

[163] R. D. McMichael and M. J. Donahue, *IEEE Trans. Magn.* **33**, 4167 (1997).

[164] R. P. van Gorkom, A. Brataas, and G. E. W. Bauer, *Phys. Rev. Lett.*, **83**, 4401 (1999).

[165] G. Tatara and H. Fukuyama,*J. Magn. Magn Mater.* **177**, 193(1998).

[166] A. D. Kent, U. Ruediger, J. Yu, S. Zhang, P. M. Levy, Y. Zhong, S. S. P. Parkin, *IEEE Trans. Magn.* **34**, 900 (1998).

[167] P.P. Freitas and L. Berger, *J. Appl. Phys.* **57**, 1266 (1985).

[168] H. Koo, C. Krafft, and R. D. Gomez, *Appl. Phys. Lett.* **81**, 862(2002).

[169] M. Tsoi, A.G.M. Jansen, J. Bass, W.C. Chiang, M. Seck, V. Soi, and P. Wyder, *Phys. Rev. Lett.* **80,** 4281 (1998).

[170] E. B. Myers, D.C. Ralph, J.A. Katine, R.N. Louie, R.A. Buhrman, *Science* **285**, 867 (1999).

[171] J. Grollier, D. Lacour, V. Cros, A. Hamzic, A. Vaurs, A. Fert, D.Adam, G. Faini, *J. Appl. Phys.* **92**, 4825 (2002).

[172] J. Grollier, P. Boulenc, V. Cros, A. Hamzic, A. Vaurs, A. Fert, and G. Faini, *J. Appl. Phys.* **95**, 6777 (2004).

[173] L. Lopez-Diaz, M. Klui, J. Rothman, J.A.C. Bland, *J. Magn. Magn. Mat.* **242**, 553 (2002).

[174] M. Klui, C. A. F. Vaz, J. A. C. Bland, W. Wensdorfer, G. Faini, and E. Cambril, *J. Appl. Phys.* **93**, 10, 7885 (2003).

[175] F.J. CastaNo, C.A. Ross, C. Frandsen, A. Eilez, D. Gil, H.I. Smith, M. Redjdal, and F. B. Humphrey, *Phys. Rev. B* **67**, 184425 (2003).

[176] E. C. Stoner and E. P. Wolfarth, *Philos. Trans R. Soc. London, Ser.* **A 240**, 599(1948).

[177] D. C. Jiles and D. L. Atherton, *J. Magn. Magn. Mat.* **61**, 48(1986).

[178] Y. B. Xu, et al., *Phys. Rev. B* **46**, R14 901, (2000).

[179] C. Yu., et al., *J. App. Phys.* **93**, 8761 (2003).

[180] S. J. C. H. Theeuwen, et al., *J. Appl. Phys.* **89**, 4442 (2000).

[181] Y. Otani et al., *IEEE Trans. Magn.* **34** 1096 (1998).

[182] U. Ebels, et al., *Phys. Rev. Lett.* **84**, 983 (2000).

[183] P. Grünberg ,R. Schreiber,Y. Pang, M. B. Brodsky and H. Sowers, *Phys. Rev. Lett.* **57** 2442 (1986).

[184] M. Lhndorf, T. Duenas, M. Tewes, E. Quandt, M. Rhrig and J. Wecker. *Appl. Phys. Lett.* **81** 313(2002).

[185] L. Baril, B. Gurney, D. Wilhoit, and V. Speriosu, *J. Appl. Phys.* **85**,5139(1995).

[186] C. S. Schneider, P. Y. Canell, and K. T. Watts, *IEEE Trans.Magn.* **28**,2626(1992).

[187] E. C. Stoner and E. P. Wolfarth, *Philos. Trans R. Soc. London, Ser.* **A240**, 599 (1948).

[188] R. Matheis, J. Langer, S. Senz, H. A. M. Vn den Berg, *Symposium Materials Research Society Symposium Proceedings*, **562**,15 (1999).

[189] D. C. Jiles and D. L. Atherton, *J. Magn. Magn. Mat.*, **61**, 48(1986).

[190] J. C. Slonczewski, *J. Magn. Magn. Mater.* **159**, L1(1996).

[191] E.B. Myers, D.C. Ralph, J.A. Katine et al., *Science* **285**, 867 (1999)

[192] J. A. Katine, F. J. Albert, R. A. Burhman et al., *Phys. Rev. Lett.* **84**, 3149 (2000).

[193] L.Berger, *Phys. Rev. B* **54**, 9353 (1996)

[194] Ya. B. Bazaliy, B. A. Jones, and S.-C. Zhang, Phys. Rev. B **57**, R3213 1998!.

[195] Z. Li and S. Zhang, *Phys. Rev. B* **68**, 024404 (2003).